FIBER-OPTIC SENSORS BASED ON FIBER BRAGG GRATINGS FOR DYNAMIC STRAIN MEASUREMENT

By

Yupeng Zhu

A DISSERTATION

Submitted to
Michigan State University
in partial fulfillment of the requirements
for the degree of

Electrical Engineering – Doctor of Philosophy

2020

ABSTRACT

FIBER-OPTIC SENSORS BASED ON FIBER BRAGG GRATINGS FOR DYNAMIC STRAIN MEASUREMENT

By

Yupeng Zhu

This dissertation investigates how to measure dynamic strain including quasi-static strain, vibration, acoustic emission, and ultrasonic waves with fiber Bragg grating based optical fiber sensors. Fiber optic sensors are inherently immune to electromagnetic interference, light weight, small size, corrosion resistance, and capable of multiplexing. With narrow linewidth tunable lasers, the strain induced spectral shift of the Bragg wavelength of the sensor can be demodulated. However, the spectrum of the uniform fiber Bragg grating can not satisfy the sensitivity, resolution, and dynamic range requirements. To address these challenges, we propose and demonstrate a sensor structure based on chirped fiber Bragg gratings combined with Fabry-Perot cavity. Taking advantage of large bandwidth provided by the chirped fiber Bragg grating and the narrow resonance peaks formed by the Fabry-Perot cavity, it can simultaneously achieve high resolution, high sensitivity, and large dynamic range measurement.

The second chapter provides the theoretical analysis and numerical simulation on the spectra of chirped fiber Bragg gratings and Fabry-Perot cavities. Based on such context, we are motivated to propose a dynamic strain measurement scenario which take advantage of both high resolution and large dynamic range of the sensor. Due to the different and unique spectral intervals of the notches in the wavelength bandwidth used for measurement, the spectral notches can be unambiguously recognized in each spectral frame without the need for fringe counting. Using this principle, we demonstrated high-resolution and absolute static and dynamic strain measurement. In chapter three, we study the acoustic emission detection with the proposed sensor based on high finesse short cavity structure and explore the potential of using the narrow resonance peak as the laser locking source to reduce the laser noise while functions as ultrasound sensor. Additionally, since the Bragg wavelength is highly related to the polarization, birefringence causes polarization dependent

center-wavelength shift. We propose a 90-degree rotation method for grating fabrication in the UV laser beam side exposure technique to reduce the birefringence. Therefore the sensor is insensitive to the polarization state of the laser, the ultrasound detection system can be simplified by omitting the polarization controller. Chapter four expands our work on ultrasonic sensor by using coiled fiber with low-finesse Fabry-Perot interferometer formed by two chirped fiber Bragg gratings. Our work has successfully demonstrated a strain and temperature insensitive fiber-optic ultrasonic detection by combining the coil structure, wide spectral range, and quadrature demodulation. The ultrasonic sensing scheme is immune to the laser wavelength drift, therefore no wavelength locking mechanism is needed. Future work will continue on exploring new design of the sensor structure and optimizing the measurement system to further improve the feasibility while reduce the overall cost.

To my family and friends, who always support and trust me.

TABLE OF CONTENTS

LIST OF TABLES

LIST OF FIGURES

CHAPTER 1

INTRODUCTION

1.1 Motivation of the Work

For the past few decades, fiber optic sensors [1] are widely researched and utilized in sensing of temperature [2], strain [3], pressure [4], magnetic field [5], and ultrasonic waves [6]. Especially in the area of non-destructive evaluation (NDE) and structural health monitoring (SHM), fiber optic sensors provide numerous advantages compare to their electronic counterparts [7, 8]. As of the glass material, they are inherently immune to electromagnetic interference (EMI) and corrosion resistance. Also, fiber optic sensors are light weight and small size, make them easily embedded into the structure of measurand. Furthermore, fiber Bragg grating (FBG) based fiber-optic sensors offer extraordinary multiplexing capabilities, making them ideal for applications requiring minimal cables with multiple sensing locations.

An FBG is a periodic refractive index modification (grating) structure at the core of an optical fiber. The optical fiber can be either single-mode fiber or multi-mode fiber. The typical diameter of coating, cladding, and core of the single-mode fiber are about 250, 125, and 8 μm. The mode-field diameter is about 10 μm at 1550 nm. Figure 1.1a shows the grating structure on a single-mode fiber. Due to the periodic structure, FBG reflects a specific part of the input broadband light and allows other light to transmit. The reflected light has a central wavelength called the "Bragg wavelength," which is expressed as [9]

$$\lambda_B = 2n_{eff}\Lambda_0 \tag{1.1}$$

where n_{eff} denotes the effective refractive index of the modes propagating in the fiber, and Λ_0 is the period of the grating. Any external parameters that can change either n_{eff} or Λ_0 can introduce a shift in the Bragg wavelength. Therefore, the value of external parameter can be derived by demodulating the Bragg wavelength of the FBG. As a strain sensor, the grating period as well as the effective refractive index are changed directly by the strain through the elasto-optic effect. With

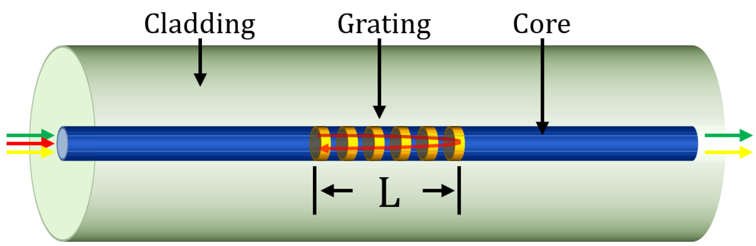

(a) The grating structure in an optical fiber.

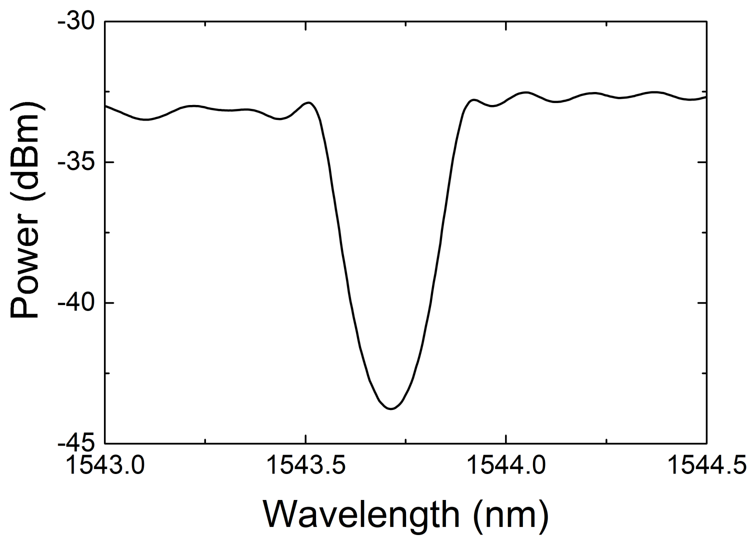

(b) The transmission spectrum of the FBG.

Figure 1.1: FBG structure and spectrum.

applied axial strain, the Bragg wavelength variation sensitivity can be written as [9, 10]

$$\Delta\lambda_B = (1 - \rho_\varepsilon)\lambda_B \varepsilon \tag{1.2}$$

where ρ_ε is the elasto-optic coefficient, which is give by

$$\rho_\varepsilon = \frac{n_{eff}^2}{2}[p_{12} - \nu(p_{11} + p_{12})] \tag{1.3}$$

where p_{11} and p_{12} are the strain—optic coefficients of fused silica material of the fiber, and ν is Poisson's ratio. The typical measured sensitivity of Bragg wavelength shifts on single-mode fiber SMF-28 is about 1.2 $pm/\mu\varepsilon$ in the 1550 nm wavelength region [11].

As the FBG only functions as sensor in the system, either the broadband light source or the probe laser is used to interrogate the sensor and the demodulation system detects the reflection or transmission light [3]. The resolution of the system is typically limited by the linewidth of the

FBG sensor and the noise of the light source, including intensity noise, and thermodynamic phase noise. The linewidth of a uniform regular FBG sensor with a typical length of 10 mm at Bragg wavelength of 1550 nm has a reflection linewidth on the order of 200 pm. Because the interested external parameter is derived from the Bragg wavelength of the sensor, the spectral linewidth of the FBG determines the sensor resolution. The measurement resolution, which is defined as the minimum change of the external parameter of interest that can be resoled by the sensor, is limited. In our work, FBG-based resonators are investigated with sub 10 pm linewidth which significantly increase the measurement resolution of the sensing system compared to the regular FBGs.

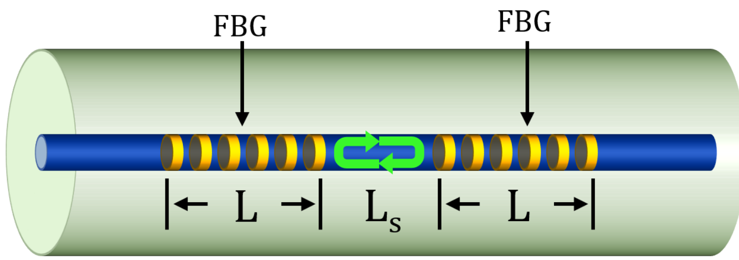

(a) The Fabry-Perot interferometer formed by a couple of FBGs.

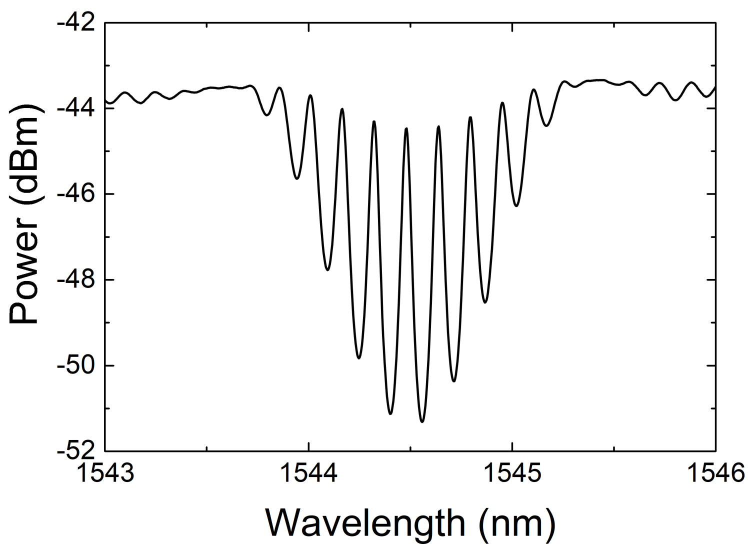

(b) The transmission spectrum of the FBG-FP sensor.

Figure 1.2: FBG-FP structure and spectrum.

In most FBG sensors, the general principle of operation is based on the Bragg wavelength shift caused by a measurand such as strain, temperature, pressure, et al. Therefore, the measurement resolution of a FBG sensor is determined by the linewidth and the slope of the reflection spectrum. In order to realize narrower linewidth or a sharper slope of the spectrum, a Fabry-Perot interferometer with a pair of FBGs (FBG-FP) [12] is introduced as shown in Fig. 1.2a. With high refractive index modification and proper distance between the FBGs, high finesse cavity features extremely narrow transmission peaks within the reflection spectrum of the sensor as shown in Fig. 1.2b. These transmission peaks shift linearly together with the Bragg wavelength when strain or temperature changes. As a result, the FBG-FP sensors provide better sensing resolution. However, the dynamic range still limited within the spectrum of the FBG on the order of 200 pm. Also the periodic nature of the fringes are not easy to distinguish in terms of equal free spectral range and fringes counter is required to measure the spectral shift correctly [13].

Additionally, laser frequency noise can not be ignored when the sharp slope of the narrow fringes is used since the laser frequency noise is converted to laser intensity variation with a large factor of the slope [14, 15]. Low frequency noise, narrow linewidth high performance laser source is perfect but the bulky size and high cost are not suitable in practical applications. High speed electronic feedback control method such as Pound-Drever-Hall technique [16] can also be used to suppress the laser frequency noise. However, the wavelength tuning capability is limited and increase the complexity. Low-cost laser source with minimal laser frequency noise is critical in dynamic strain measurement applications.

A narrow fringe is also sensitive to the polarization of the laser because of the birefringence introduced by the FBG resulting different Bragg wavelengths for the principal axes of the sensor. The Bragg wavelength differences can be on the order of pm which is close to the linewidth of the fringe. Either a polarization controller after the laser to align the laser polarization to the sensor [17] or polarization-maintaining fiber for the sensor [11] is required to ensure the best performance. The misalignment of the polarization between the laser wavelength and the principal axes of the sensor can reduce the sensing signal significantly.

As the grating structure is a cylindrical structure along the fiber core, the sensor exhibits a unique response the the dynamic strain signal. Its sensitivity to the strain signal is directive. More specificity, the sensor is more sensitive to the dynamic strain signal that propagate along the fiber direction, but not to those that propagate in its transverse direction [6]. In order to realize omni-directional sensitivity, a metal ring structure was integrated with the FBG sensor to change its properties to the dynamic strain signals [18], the sensor becomes a resonant sensor and sensitive to the out-of-plane strain. Subsequently, the whole sensor structure is inevitably bulkier and the signal is more complicated.

This dissertation consists of a series of studies that allow for the development of fiber Bragg grating structures, demodulation algorithms, laser noise reduction, polarization dependency, and ways to simplify the control system. By applying the new fiber-optic sensor structure onto various dynamic strain applications, we intend to propose novel fiber Bragg grating designs and innovative fabrication process to significantly enhance the dynamic range, resolution, signal-to-noise ratio, laser performance, and the whole system cost.

1.2 Dissertation Outline

The remainder of this dissertation is organized as follows; In **Chapter 2**, based on the coupled mode theory, the theoretical analysis and numerical simulations conducted on the spectra of CFBG and CFBG-FP is provided. To improve the reliability, realize the absolute measurement, and overcome the drawbacks of the FBG-FP sensors, we propose to use CFBG-FP sensors with opposite chirp direction which possess both high sensitivity and high dynamic range for dynamic strain measurement. CFBG-FP sensors are promising candidate for dynamic strain measurement for low-cost, multiplexing scenario.

Chapter 3 presents the ultrasonic wave detection with both the π-phase-shifted FBG (πFBG) and the CFBG-FP sensors. To minimize the electronic feedback system and the laser noise, self-injection locking distributed feedback (DFB) laser with a πFBG are combined for high signal-to-noise ratio (SNR) ultrasonic wave detection; Acoustic emissions (AE) are generated and captured on the fraction of a aluminum board with CFBG-FP sensor by edge filter detection method.

Chapter 4 covers a low-finesse CFBG-FP sensor which realizes quadrature demodulation makes it respond to ultrasonic signal all the time regardless the background environmental variations. The experimental results showed that the sensor is capable of detecting ultrasonic signal when the sensor spectra experience environmental drifts using a laser at fixed wavelength.

Chapter 5 draws the conclusions, and summarizes the contributions in this dissertation and suggests future research directions.

CHAPTER 2

FABRY-PEROT INTERFEROMETER FORMED WITH CHIRPED FIBER BRAGG GRATINGS

Part of the material in this chapter has been published in "Fabry–Perot sensor using cascaded chirped fiber Bragg gratings with opposite chirp directions," IEEE Photonics Technology Letters, vol. 30, no. 16, pp. 1431, 2018.

In this chapter, we conduct analytical and numerical simulations on the spectra of chirped fiber Bragg gratings (CFBGs) and CFBG-FP sensors. The configuration of chirp direction and the effects to the spectra will be explained in details. The grating spectrum is described based on the coupled mode equations. The transform matrix method is applied to solve these equations to generate the optical spectrum of grating with chirped structures. Furthermore, the free spectral range (FSR) and the effective length of the Fabry-Perot cavity formed by CFBGs are provided. The analysis can be used to optimize the grating structures for sensing applications and to predict the characteristics of grating structures under different writing conditions. Therefore, the theoretical study in this chapter can provide a guidance for the sensor fabrication and understanding the grating-based sensing behavior. Then we demonstrate the dynamic strain measurement with cascaded CFBG with opposite chirp directions that can simultaneously achieve high resolution and large dynamic range.

2.1 Coupled Mode Theory and Transfer Matrix Method for Chirped Fiber Bragg Grating

As discussed in Chapter 1, our work is mainly focused on the use of CFBGs in single-mode optical fiber to overcome the drawbacks of regular uniform FBGs including low resolution and small effective bandwidth. An analytical solution does not exist for most nonuniform grating structures. In this section, the transfer matrix method, which is applicable to arbitrary grating structures, is used to numerically solve the coupled mode equations [19, 20, 21]. For a CFBG with linear periodic modulation of its effective refractive index along the fiber axis z [22]:

$$n_{eff}(z) = n_{eff} + \Delta n_{eff}[1 + \nu\cos(\frac{2\pi}{\Lambda(z)}z)] \tag{2.1}$$

where n_{eff} is the effective refractive index of the guided mode in the unperturbed single-mode fiber, Δn_{eff} is the modulation depth, ν is the fringe visibility, $\Lambda(z) = \Lambda_0 + Cz$ is the chirped gating period with nominal grating period Λ_0 and C is the chirp ratio of the grating.

For CFBG in a single-mode fiber, the mode coupling happens predominantly between the forward propagating mode and the identical counter-propagating mode. However, the coupling coefficients are not constant in chirped grating structure. Therefore, an analytical solution could not be derived from the first-order ordinary differential coupled-mode equations. The transfer matrix method, which is applicable to arbitrary grating structures, is used to numerically solve the coupled-mode equations for grating analysis.

The idea of the transfer method is to divide the complicated grating structure into N uniform sections. Each section is treated as a uniform FBG, and the overall spectrum of the CFBG can be calculated by multiplexing the matrix describing each uniform section for which an analytical solution exists.

Assuming each sub-grating is a four port system with a grating featured as a transfer matrix T_k, defining A_n, B_n to be the field amplitudes along the $+z$ direction and $-z$ direction respectively, then the total structure can be derived by multiplying each transfer matrix together, which is given by [21]

$$\begin{bmatrix} A_0 \\ B_0 \end{bmatrix} = T_M T_{M-1} \cdots T_k \cdots T_1 \begin{bmatrix} A_M \\ B_M \end{bmatrix} = \begin{bmatrix} T_{11} & T_{12} \\ T_{21} & T_{22} \end{bmatrix} \begin{bmatrix} A_M \\ B_M \end{bmatrix} \tag{2.2}$$

Here, A_0, B_0, A_M, and B_M are the field amplitudes at $z = 0$ and $z = M$ respectively, and the matrix for each uniform section T_k is given by [21]

$$T_k = \begin{bmatrix} \cosh(\Omega\Delta z) - j\frac{\sigma}{\Omega}\sinh(\Omega\Delta z) & -j\frac{\kappa}{\Omega}\sinh(\Omega\Delta z) \\ j\frac{\kappa}{\Omega}\sinh(\Omega\Delta z) & \cosh(\Omega\Delta z) + j\frac{\sigma}{\Omega}\sinh(\Omega\Delta z) \end{bmatrix} \tag{2.3}$$

where $\sigma = 2\pi n_{eff}(\frac{1}{\lambda} - \frac{1}{\lambda_B})$ is a DC coupling coefficient and $\kappa = \frac{\pi}{\lambda}\Delta n_{eff}$ is an AC coupling coefficient of the k^{th} section, $\Omega = \sqrt{\kappa^2 - \sigma^2}$. With the boundary condition that the light is injected from $-\infty$ and the grating starts at $z = \frac{L}{2}$, we have $A_0(-L/2) = 0$, $B_0(L/2) = 0$, the matrix specifies each section that can be obtained.

The reflectivity of the whole grating structure can be expressed as

$$R = \left|\frac{T_{21}}{T_{11}}\right|^2 \tag{2.4}$$

If the loss is negligible, as a consequence of conservation of energy, one can find the transmitted power simply as $T = 1 - R$. In the following numerical simulations, only the transmission characteristics are considered. It is worth noting that the number of sections for the transfer matrix method should be carefully chosen. Usually the number of total pieces should satisfy [23]

$$M << \frac{2n_{eff}L}{\lambda_B} \tag{2.5}$$

2.2 Simulation

The structure of a Chirped FBG (CFBG) is shown in Fig. 2.1. Unlike the unchirped FBG, the refractive index modulation has a linear period variation with a chirp rate ($\Delta\Lambda$) instead of a constant period (Λ). Compare to the regular FBG, the grating period of the CFBG increases or decreases along the fiber axis, resulting a wider bandwidth of the reflection spectrum than a regular FBG. The bandwidth of the CFBG is proportional to the chirp rate with a center wavelength at the Bragg wavelength. For a single CFBG, the parameters used for the numerical simulations are listed in Table 2.1:

Table 2.1: Parameters of the CFBG used in the simulation.

Symbol	**Physical Quantity**	**Value**	**Unit**
L	Grating length	5	mm
ΔL	Edge-to-edge distance between gratings	0	mm
Λ_0	Phase mask pitch period	1067.7	nm
C	Phase mask chirp ratio	4	nm/cm
n_{eff}	Effective refractive index	1.448	-
Δn_{eff}	Refractive index modulation depth	5×10^{-4}	-
M	Total section number	200	-
v	Fringe visibility of index change	1	-

Figures 2.1 shows the structure of a single CFBG and the simulated transmission spectrum of the CFBG. Similar to the uniform FBG, the reflectivity of the CFBG can be enhanced by either the increasing the grating length or increasing refractive index modulation depth through more exposure to the UV laser. The center wavelength will shifts toward a longer wavelength with the increased UV exposure and independent of the grating length. The bandwidth of the CFBG is proportional to the chirp rate and grating length, while the uniformity of the reflection band is inversely proportional to the chirp rate. Therefore, depends on the applications, chirp rate and grating length should be carefully designed for optimal performance of the CFBG.

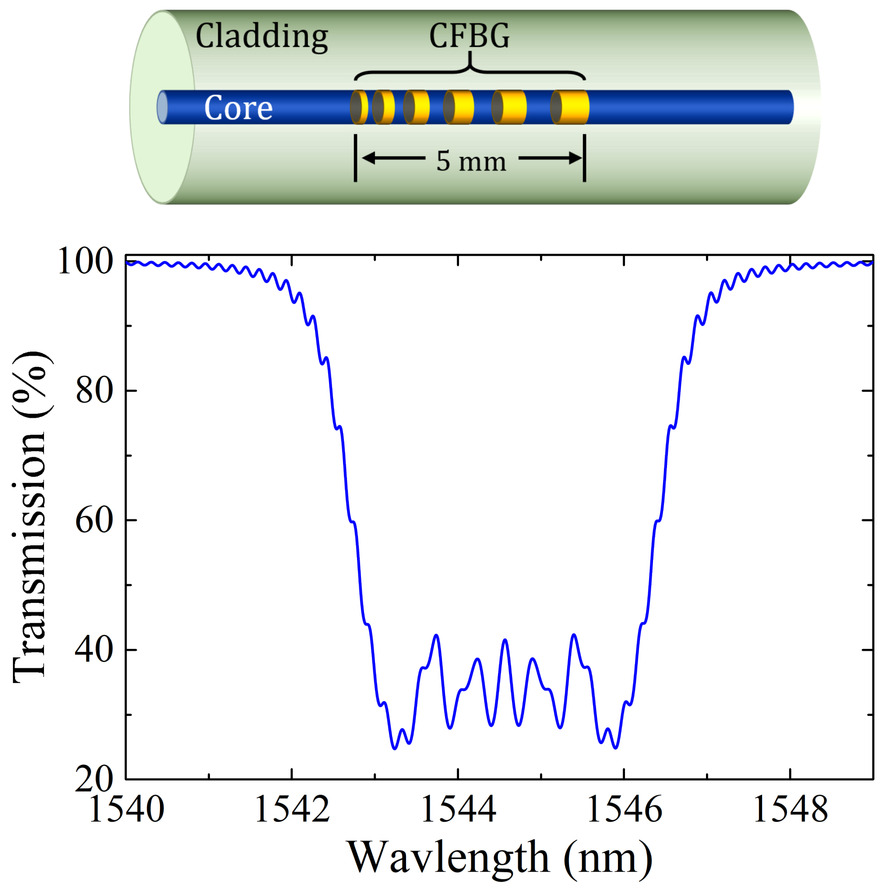

Figure 2.1: Structure of a single CFBG (top) and the simulated transmission spectrum (bottom).

2.2.1 CFBG-FP with same chirp direction

Similar to FBG-FP sensors, if two identical CFBGs are inscribed with some space apart in an optical fiber, they also form a Fabry-Perot interferometer with CFBG reflectors (CFBG-FP), the transmission characteristics of the CFBG-FP cavity is an ideal lossless cavity constructed by two CFBGs with the same chirp direction and also the same other parameters as shown in the Table 2.1. The edge-to-edge distance between the CFBGs is set to 0.

The transmission spectrum of the CFBG-FP sensor features a number of narrow peaks that are approximately equal-spaced within the broad transmission bandwidth [24]. The spectral distance between adjacent peaks is called free spectral range (FSR). It is decided by the relative position between two CFBGs, and the chirp direction. The FSR is inversely proportional to the geometrical distance between the CFBGs.

To ensure at least one interference peak locates within the CFBG spectrum, the FSR should be smaller than half of the full width half maximum (FWHM) of the bandwidth of the CFBG. The FSR $\Delta\lambda$ is given by:

$$\Delta\lambda = \frac{\lambda^2}{2n_g L_c}, \tag{2.6}$$

where λ is the Bragg wavelength of the CFBG, n_g is the group refractive index of the LP_{01} mode of the fiber. For conventional single mode optical fiber, group refractive index $n_g \approx n_{eff}$, where n_{eff} is the effective refractive index. The n_{eff} for our fiber is about 1.448. L_c is the effective length, which is a sum of the effective lengths of both the CFBGs forming the cavity and the edge-to-edge distance between between the two FBGs: $L_c = L_s + L_{eff1} + L_{eff2}$. The grating effective length L_{eff} at the Bragg wavelength is given by [12]:

$$L_{eff} = L\frac{\sqrt{R}}{2\,\mathrm{arctanh}(\sqrt{R})}, \tag{2.7}$$

where R is the grating peak reflectivity. As shown in Fig. 2.2, with a low reflectivity value, the effective length of the grating L_{eff} is around half of the grating physical length L; while at high reflectivity value the effective length is close to zero. It can be physically comprehended by the fact that for a weak FBG, the reflected light along the grating is homogeneously distributed, while a high reflective FBG reflects most of the light from its initial part.

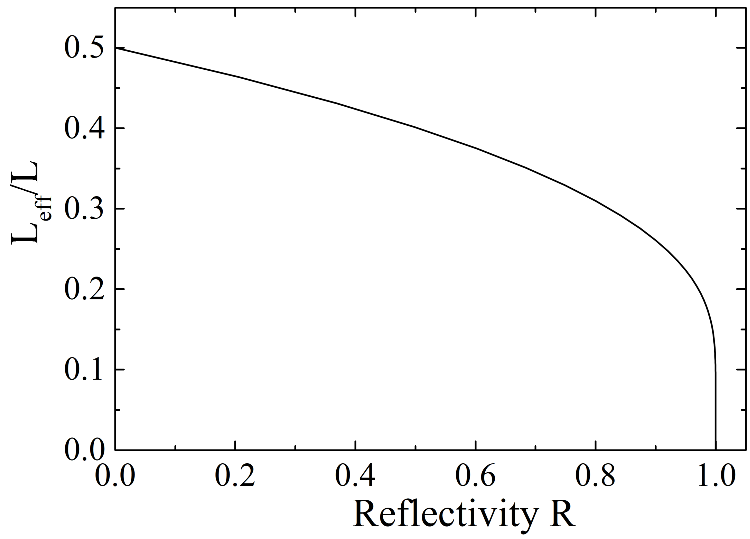

Figure 2.2: Relative effective length of a FBG versus its reflectivity R.

In our numerical simulations, the refractive index modulation depth is about 5×10^{-4} which resulting a total reflectivity of 60% at the Bragg wavelength. Then the relative effective length L_{eff}/L is about 0.4 for a single 5-mm CFBG with 60% reflectivity. For a pair of CFBGs with the same 60% reflectivity, $L_{eff1} = L_{eff2} = 2$ mm. The edge-to-edge distance L_s is set to be 0. Therefore, the effective length L_c is 4 mm. The FSR is expected to be around 206 pm.

The top of Fig. 2.3 shows the structure of the CFBG-FP sensor with the same chirp direction and the bottom shows the corresponding transmission spectrum and the FSR of the selected resonance peaks. A couple of CFBGs cascaded in the same chirp direction provides comb-like FSR. The intervals between peaks are uniform but not exactly the same. This scheme can work as a wide-band filter for communication systems. These peaks can also be used for relative measurement by counting the wavelength peaks number. However, lost of previous counting information could lead to enormous error. There are 16 resonance peaks in the 3 dB transmission bandwidth and the neighboring resonance peaks intervals are approximately uniform, as can seen from the markers from Fig. 2.3.

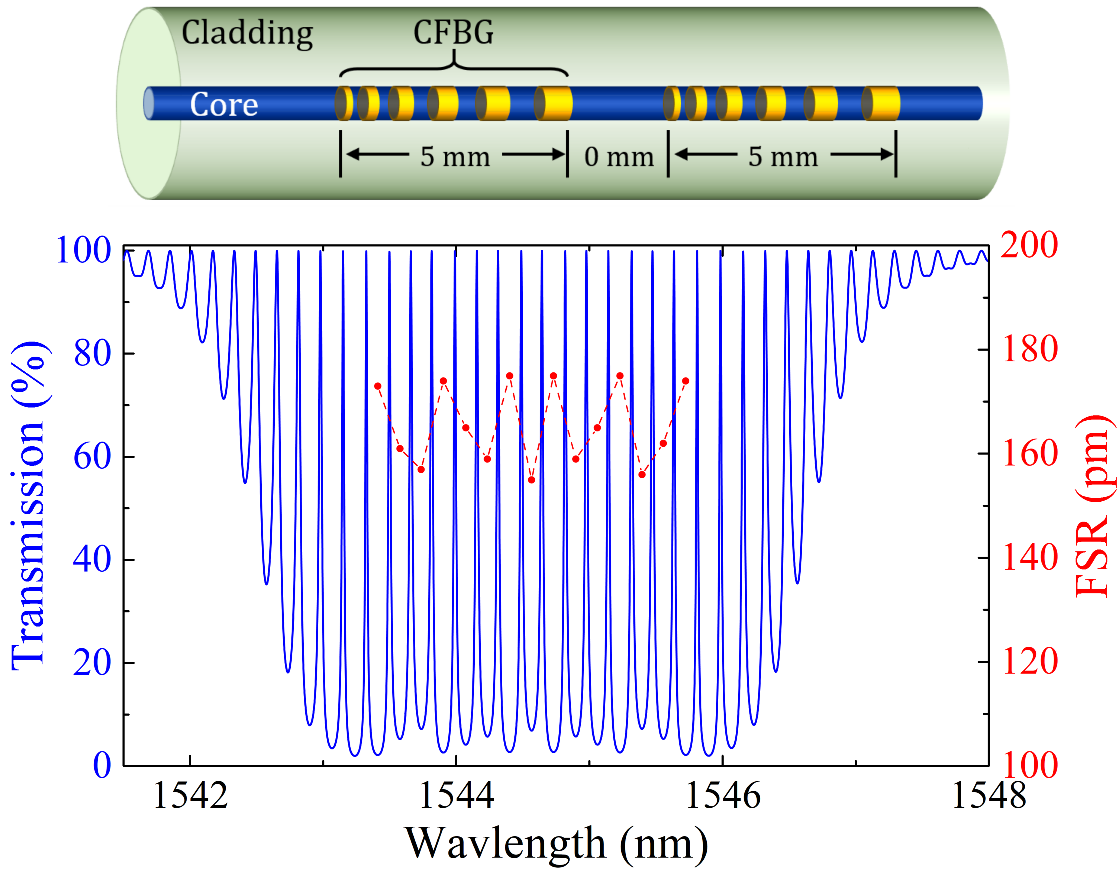

Figure 2.3: Structure of the CFBG-FP with the same chirp direction (top) and the simulated transmission spectrum (bottom).

2.2.2 CFBG-FP with different chirp directions

For the CFBG-FP sensor constructed by two CFBGs with opposite chirp directions, as shown at the top of Fig. 2.4 and Fig. 2.5, the transmission spectra and the FSR feature are depicted at the bottom of Fig. 2.4 and Fig. 2.5, respectively. Obviously, the FSR is also related to the chirp direction. If the CFBGs have the same chirp direction, the FSR is equally spaced in the transmission band of the CFBG-FP sensor; If the shorter-period sides of the CFBGs are face to each other, the FSR at shorter wavelengths is larger than the longer wavelengths, and vice versa.

It is obvious the intervals of neighboring resonance peaks show non-uniformity feature. According to the different chirp directions, the peak intervals are increased or decreased with respect to the wavelengths. That features are because the signals with different wavelengths are reflected at different positions along the linearly chirped gratings, which result in the different effective cavity

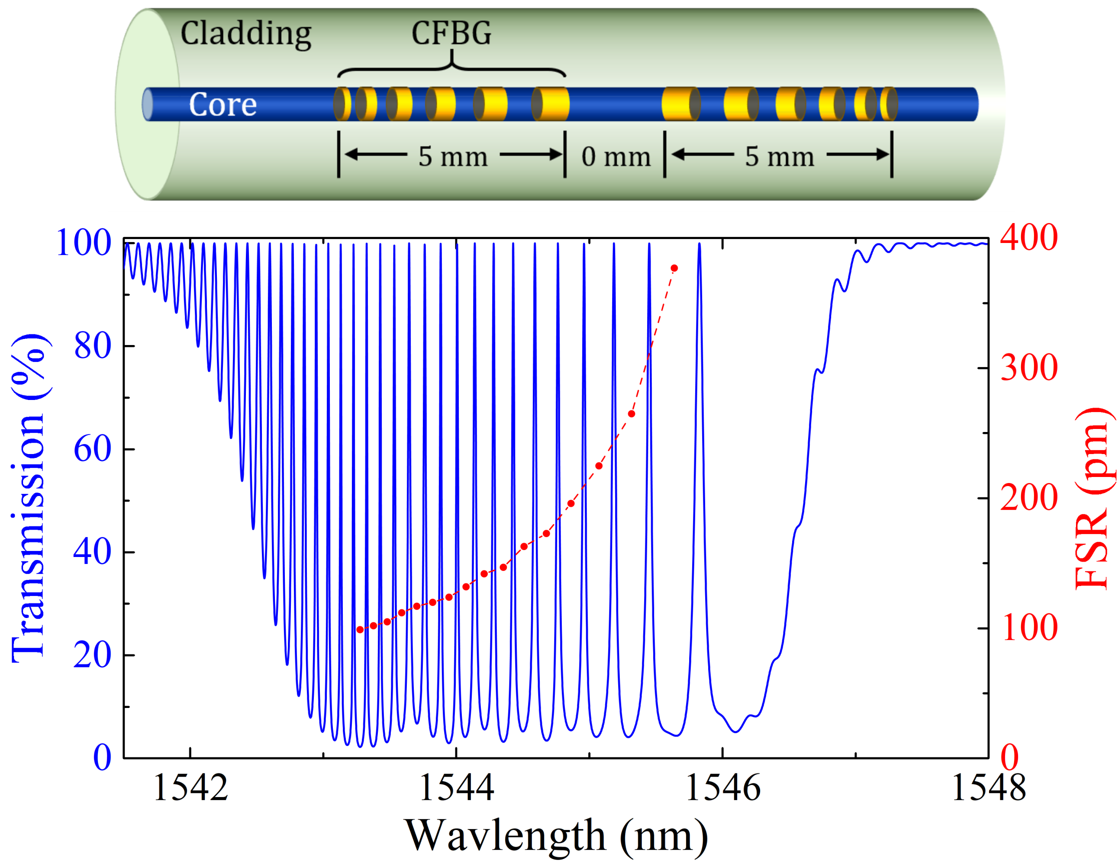

Figure 2.4: Structure of the CFBG-FP with larger pitch period sides close to each other (top) and the simulated transmission spectrum and the FSR feature (bottom).

lengths for different wavelength. As shown in Fig. 2.4, the larger pitch period sides close to each other, resulting a smaller effective cavity length for longer grating wavelength. Since the neighboring peak interval of the FP cavity (FSR) is approximately inverse proportion to the effective cavity length shown in Eq. (2.6), FSR will be larger at longer wavelength. Similarly, for the shorter pitch period sides close to each other structure shown in Fig. 2.5, FSR is smaller at longer wavelength. The FSRs in Fig. 2.4 and Fig. 2.5 are in good agreement with the theory. Therefore, by using CFBG-based FP cavities as a series of ideal FP cavities with different lengths, the apparent non-uniformity of the spectral lines can be clearly seen. The key idea to realize absolute measurement relies on the combination of initial reference with recognizable detection signal, i.e. unique FSR formed by the opposite chirp direction. Reversing one chirping direction can generate different "cavity length" for different wavelength. The unique FSR feature and the narrow linewidth of the resonance peaks can be used for absolute strain measurement and will be further discussed in Section 2.4.

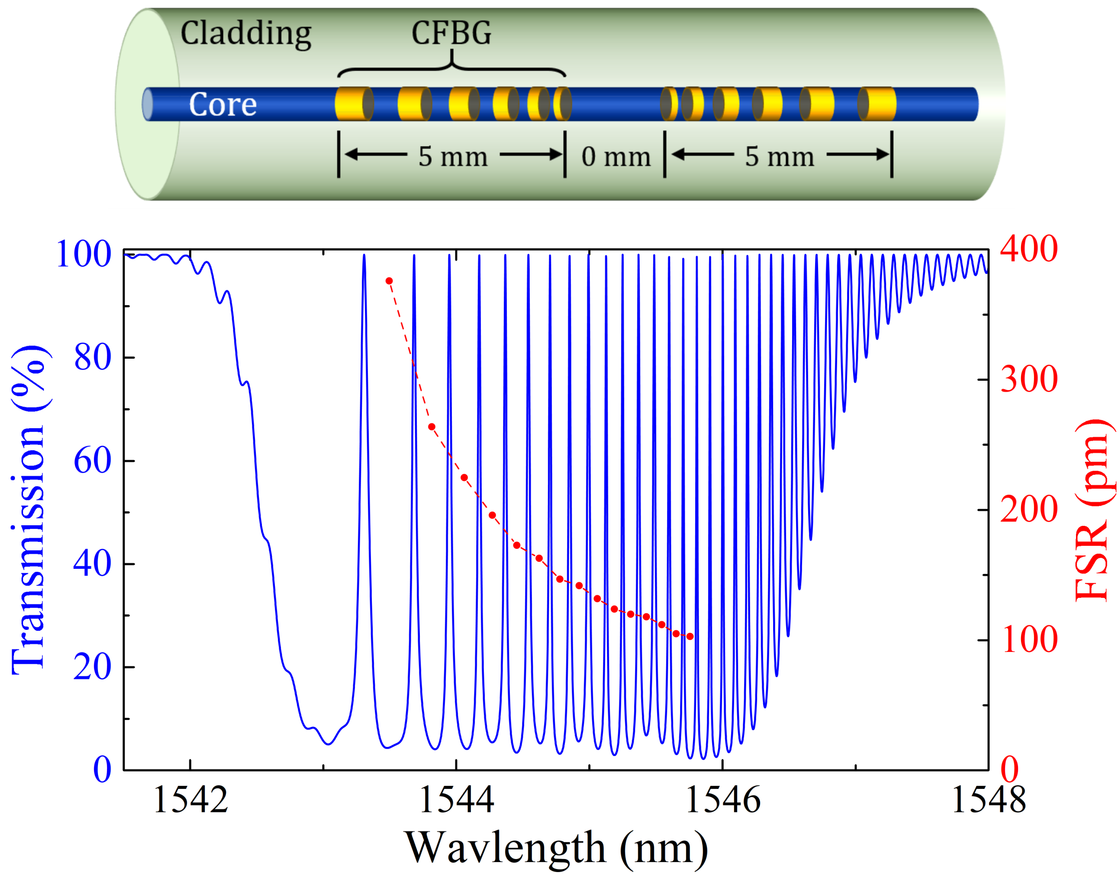

Figure 2.5: Structure of the CFBG-FP with smaller pitch period sides close to each other (top) and the simulated transmission spectrum and the FSR feature (bottom).

2.3 Dynamic strain demodulation of the FBG-based sensors

FBG-based pressure sensors, acceleration sensors, vibration sensors, acoustic emission sensors, and ultrasonic sensors can be collectively referred to as dynamic strain sensors. The large dynamic strains such as pressure, acceleration, and vibration can be demodulated by monitoring the spectral shifts of the FBGs. The demodulation methods can be classified as the spectrometric method, and the scanning method [3]. The spectrometric method includes a broadband light source and an optical spectral analyzer which is limited by the low resolution and low sensitivity, as shown in Fig. 2.6. On the other hand, the scanning method includes a tunable laser source and a fast respond photodiode which provides high resolution and high speed. However, due to the hysteresis effect caused by the scanning laser, it limits the scanning range and scanning speed which can not compare to the dynamic range of the spectrometric method.

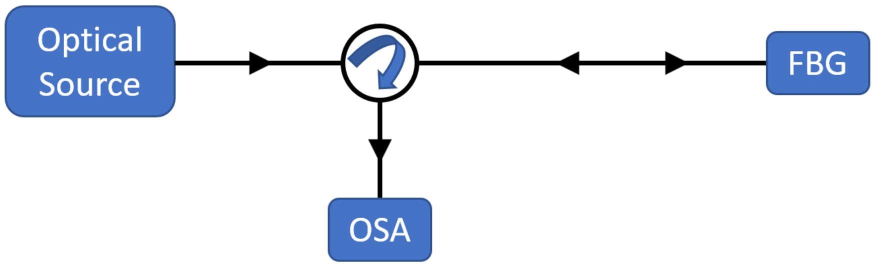

Figure 2.6: Schematic interrogation set up with spectrometric method.

In the case of small dynamic strain caused by small vibration, acoustic emission, or ultrasonic wave is applied to the FBG-based sensor, the demodulation using in this work is called edge filter detection method, as shown in Fig. 2.7.

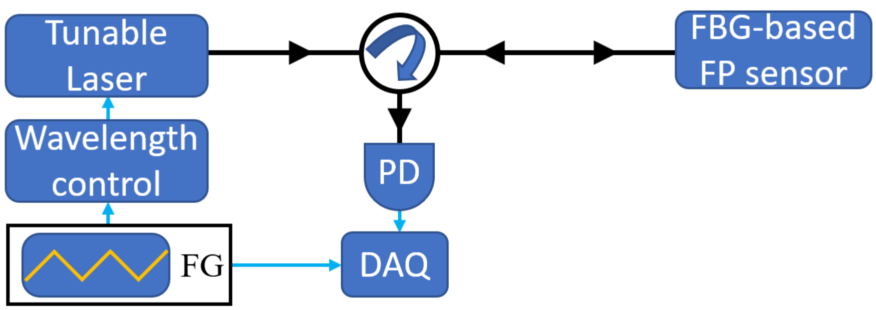

Figure 2.7: Example of experimental set-up for edge filter interrogation technique.

Specifically, narrow-band light such as laser light is used as the optical source and its wavelength is set to the slope of the reflectance spectrum of the sensor, as shown in Fig. 2.8. We assume the dynamic strain is small enough for the sensor reflectance spectrum to be kept unchanged in shape as well as for the shift not over the linear region of the slope. Therefore, the change in the reflectance of the sensor at the operation wavelength is proportional to the applied strain. As a result, we can directly measure the variation of the reflectance intensity to decode the dynamic strain.

By using a photodetector (PD) to receive the reflected or transmitted light power of the FBG sensor, the ultrasonic signal can be represented as a voltage function. With the linear range of the

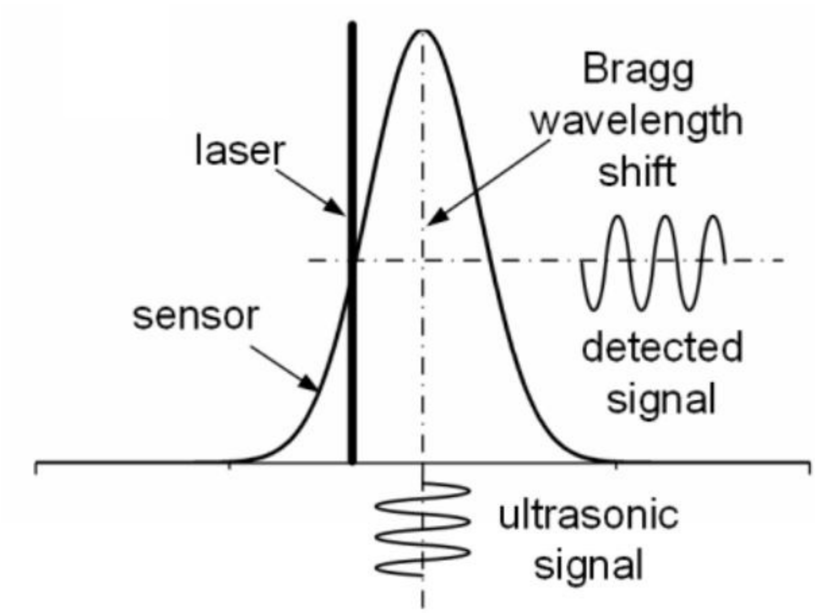

Figure 2.8: The principle of the edge filter detection interrogation technique.

grating slope, the amplitude of the detected signal is proportional to the ultrasonic signal. The AC components of the received voltage signal can be expressed as [6]

$$V_S = \Delta\lambda_B G R_D P \tag{2.8}$$

where V_S is the detected AC signal voltage, $\Delta\lambda_B$ is the Bragg wavelength shift caused by strain, G is the slope of the grating, R_D is the response factor of the PD, and P is the input laser power. It is clear that the detected voltage is proportional to the slope of the grating and the input laser power, using a sharp slope of the sensor with a high power laser benefits the amplitude of the detected signal. On the other hand, the noise level of the system limits the sensitivity, considerable efforts in this demodulation technique are made to optimize the signal-to-noise ratio. One example to reduce the frequency noise is using self injection locking technique on a DFB laser to achieve over 35 dB increase of the signal-to-noise ratio for ultrasonic signal detection.

FP interferometers (FPIs) formed by cascaded chirped fiber Bragg gratings (CFBGs) show unique spectral properties that can be explored to improve sensor performance. Due to the varying grating pitches in a CFBG, different positions of the CFBG reflect light at different wavelengths.

In most cases, the two CFBGs have the same chirp direction, resulting in multiple almost evenly-spaced spectral notches. The multiple spectral notches in a CFBG-FPI have also been explored for detection of acoustic emission under large quasi-static strains. As the transmission peaks of the CFBG-FPI are almost evenly spaced, the peaks cannot be unambiguously identified within a narrow wavelength-sweeping range; as a result, only relative measurement is possible. Moreover, achieving increased dynamic range requires the accurate and continuous counting of the peaks that enter the sweeping range throughout the measurement process. Any error in counting the peaks results in accumulative and large error corresponding to the spectral spacing of the peaks. We present a fiber-optic FPI sensor formed by cascaded CFBGs with opposite chirp direction. For such a CFBG-FPI, the cavity length of the FPI is wavelength dependent, leading to unevenly-spaced spectral notches. The spectrum of such FPIs has been studied theoretically and its application for improving resolution and dynamic range has been explored.

2.4 Fabry-Perot Sensor Using Cascaded Chirped Fiber Bragg Gratings with Opposite Chirp Directions

In this section, we demonstrate a fiber-optic strain sensor that can simultaneously achieve high resolution and large dynamic range. The sensor is a fiber-optic Fabry-Perot (FP) cavity formed by cascaded high-reflection chirped fiber Bragg gratings (CFBGs) with opposite chirp directions. The reflection spectrum of the sensor features a series of narrow spectral notches with unequal spacings. The sensor is demodulated by wavelength scanning of a distributed feedback laser diode through current-injection modulation. The narrow spectral notch leads to high measurement resolution; while the unambiguous identification of the spectral notches through their unique spectral spacings results in large measurement range without the need for fringe counting. We have demonstrated a linear axial strain response of the sensor with strain resolution of 0.033 $\mu\varepsilon$ over a range of 1000 $\mu\varepsilon$.

2.4.1 Introduction

Fiber-optic sensors based on various grating structures have been extensively studied for measurement of a wide range of physical and biochemical parameters [1, 25, 26]. In particular, Fabry-Perot interferometers (FPIs) formed by cascaded chirped fiber Bragg gratings (CFBGs) show unique spectral properties that can be explored to improve sensor performance [27, 28, 29, 30]. Due to the varying grating pitches in a CFBG, different positions of the CFBG reflect light at different wavelengths. In most cases, the two CFBGs have the same chirp direction, resulting in multiple almost evenly-spaced spectral notches [24]. The multiple spectral notches in a CFBG-FPI have also been explored for detection of acoustic emission under large quasi-static strains [17]. CFBG-FPIs have also been used as high-resolution sensors demodulated by a distributed feedback (DFB) laser diode whose wavelength is scanned through injection current modulation [29]. Although the wavelength scanning range of a DFB laser is limited (a few hundred pm), multiple transmission peaks of the CFBG-FPI can be used to increase the dynamic range of the sensor. As the transmission peaks of the CFBG-FPI are almost evenly spaced, the peaks cannot be unambiguously identified within a narrow wavelength-sweeping range; as a result, only relative measurement is possible [29]. Moreover, achieving increased dynamic range requires the accurate and continuous counting of the peaks that enter the sweeping range throughout the measurement process. Any error in counting the peaks results in accumulative and large error corresponding to the spectral spacing of the peaks.

In this section, we present a fiber-optic FPI sensor formed by cascaded CFBGs with opposite chirp direction. For such a CFBG-FPI, the cavity length of the FPI is wavelength dependent, leading to unevenly-spaced spectral notches. The spectrum of such FPIs has been studied theoretically [24] and its application for improving resolution and dynamic range has been explored [27, 30]. For example, in [30], the different spectral widths of the notches were used to tune the sensitivity in case of intensity demodulation by a laser. However, for wavelength demodulation, the demonstration was still limited to relative measurement and fringe counting was needed to use multiple notches for increased dynamic range. In [27], improving resolution and dynamic range was achieved by probing the sensor at two different wavelength windows through a widely wavelength-tunable laser.

The wavelength windows were separated by over 10 nm where the sensor had vastly different free-spectral ranges. Unfortunately, scanning over this large wavelength range greatly reduces the speed of the sensor system and makes it unsuitable for measurement of dynamic parameters. Here, we show that, through high-speed wavelength-scanning demodulation using a DFB laser, the sensor can achieve high resolution, large dynamic range, and absolute measurement for both static and dynamic strain measurement. Specifically, the unique spectral spacing of the reflection notches renders the possibility to unambiguously recognize each of the notches within the wavelength-sweeping range that covers at least two neighboring spectral notches. With the knowledge of the wavelength position of a specific notch, absolute measurement is achieved. Because of the notch is recognized during each wavelength sweep, no notch counting is needed to achieve large dynamic range. Similar to other CFBG-FPIs, the narrow spectral features allow high resolution measurement. The high-speed wavelength scanning achieved through injection current modulation of the DFB laser makes it possible for measurement of dynamic strains.

2.4.2 Sensor calibration and static strain measurement

The cascaded CFBGs are were fabricated on 80-μm single mode fiber by a chirp phase mask with 4 nm/cm chirping rate based on the scanning beam technique [31]. The reason to choose 80 μm single mode fiber instead of standard 125 μm single mode fiber is because of the smaller diameter and higher Ge-doped concentration which lead to easier grating fabrication with the UV laser system. The length of a single CFBG is 4.5 mm, no gap between the cascaded CFBGs. As shown in Fig. 2.4, the opposite chirp directions of the two CFBGs is realized by changing fiber direction before fabricating the second CFBG. Only one chirped phase mask is needed. During fabrication, the spectrum is monitored by an optical spectrum analyzer (OSA) with a broadband light source. Reflectivity of each CFBG is more than 90% over a spectral width of 1.6 nm. The reflection spectrum of the in-band peaks, and the notch spacings are shown in Fig. 2.9. Due to the limited resolution of the OSA (20 pm), the notching spacings were measured by the scanning DFB laser setup shown in Fig. 2.10, as described in detail later.

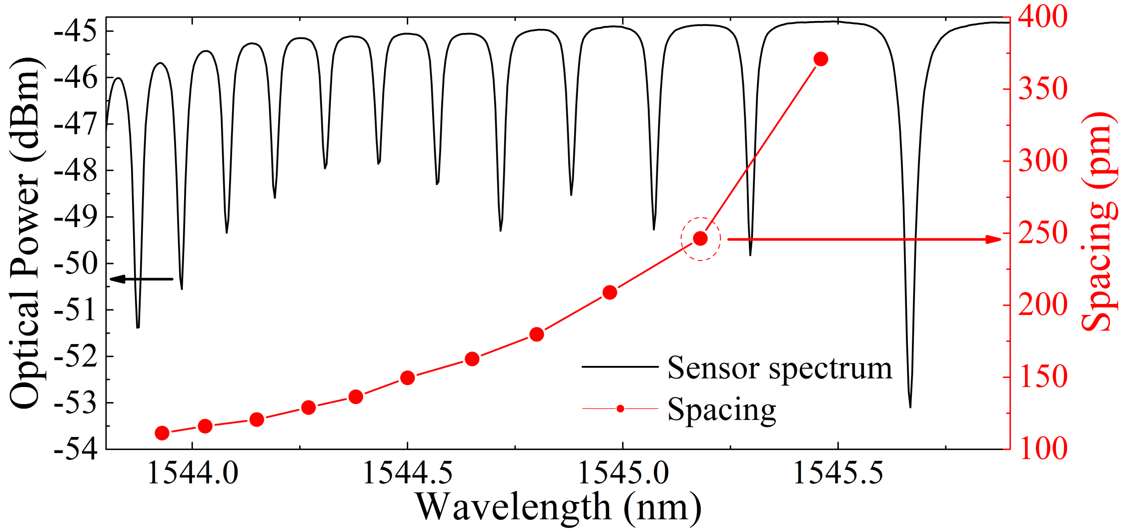

Figure 2.9: Reflection spectrum of the sensor measured by an OSA and the spectral spacing of 12 spectral notches

Static strain measurement using the setup shown in Fig. 2.10 was performed to calibrate the sensor sensitivity to strain and study the sensor performance in terms of dynamic range and resolution. The light from a DFB laser was directed to the CFBG-FPI sensor through a circulator. A polarization controller was used before the circulator to ensure that laser polarization was aligned with one of the principle axes of the sensor. Through the same circulator, the light reflected from the sensor was directed to the photodetector (PD) and the output was recorded by a data acquisition (DAQ) device at a sampling rate of 2.0 MS/s. The current controller for the DFB laser was biased at 225 mA and modulated with 500 Hz, 2 V (corresponding to 100 mA) peak-to-peak triangle wave to control the center wavelength and the scanning range of the laser. These parameters were set so that the scanning range of DFB laser diode covered at least two notches of the sensor over the designed measurement range.

Due to the tuning hysteresis of the DFB laser by injection current [32], calibration of the relative wavelength shift to the scanning voltage range is necessary. As shown in Fig. 2.11, triangular scanning waveforms are used to drive the DFB laser, up and down scanning experience different paths and form a hysteresis loop. The scanning range and frequency are selected based on the measurement condition. These calibrations curves were used to convert scanning voltage to

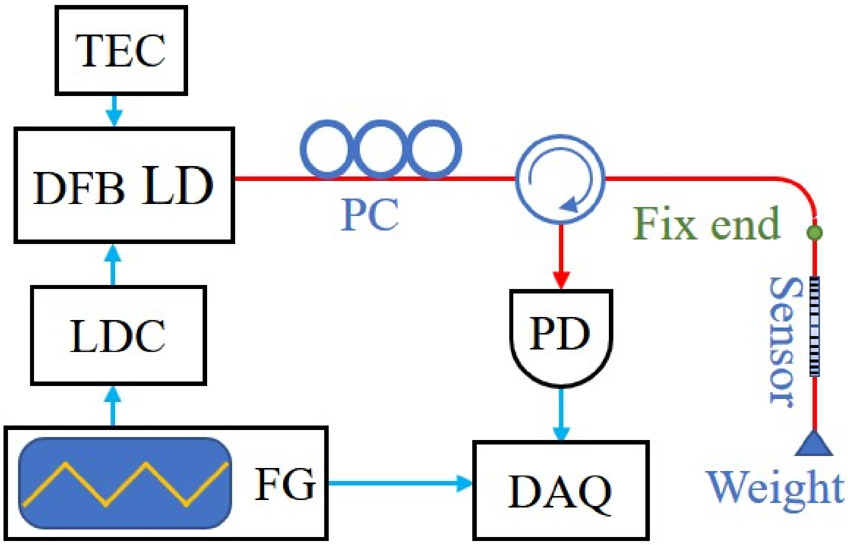

Figure 2.10: System setup for CFBG-FPI calibration and static strain measurement. TEC: temperature controller; LDC: laser diode controller; DFB LD: DFB laser diode; PC: polarization controller; PD: photodiode; DAQ: data acquisition; FG: Function generator.

wavelength shift.

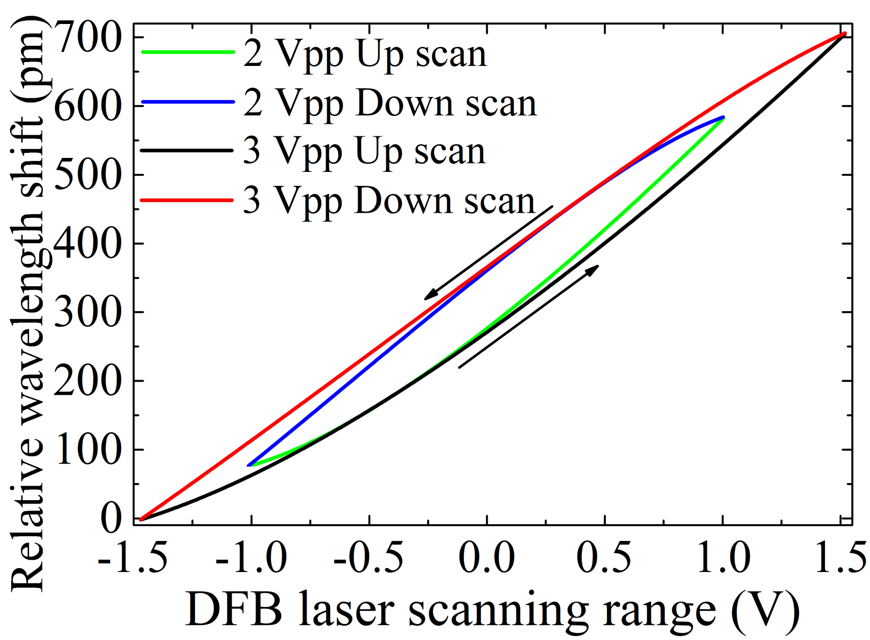

Figure 2.11: DFB laser calibration curve.

For sensor calibration and static strain measurement, the sensor is vertically placed with a fixed top end. Axial strain is applied by increasing weight on the free end of the sensor. The spectral notch spacings of the sensor were measured by applying weight to the fiber to induce axial strain on the CFBG-FPI sensor. By adding weight, spectral notches successively passed the wavelength scanning range to measure their wavelength positions and spectral spacings. The spectral spacings were used for the notch identification in the strain measurement.

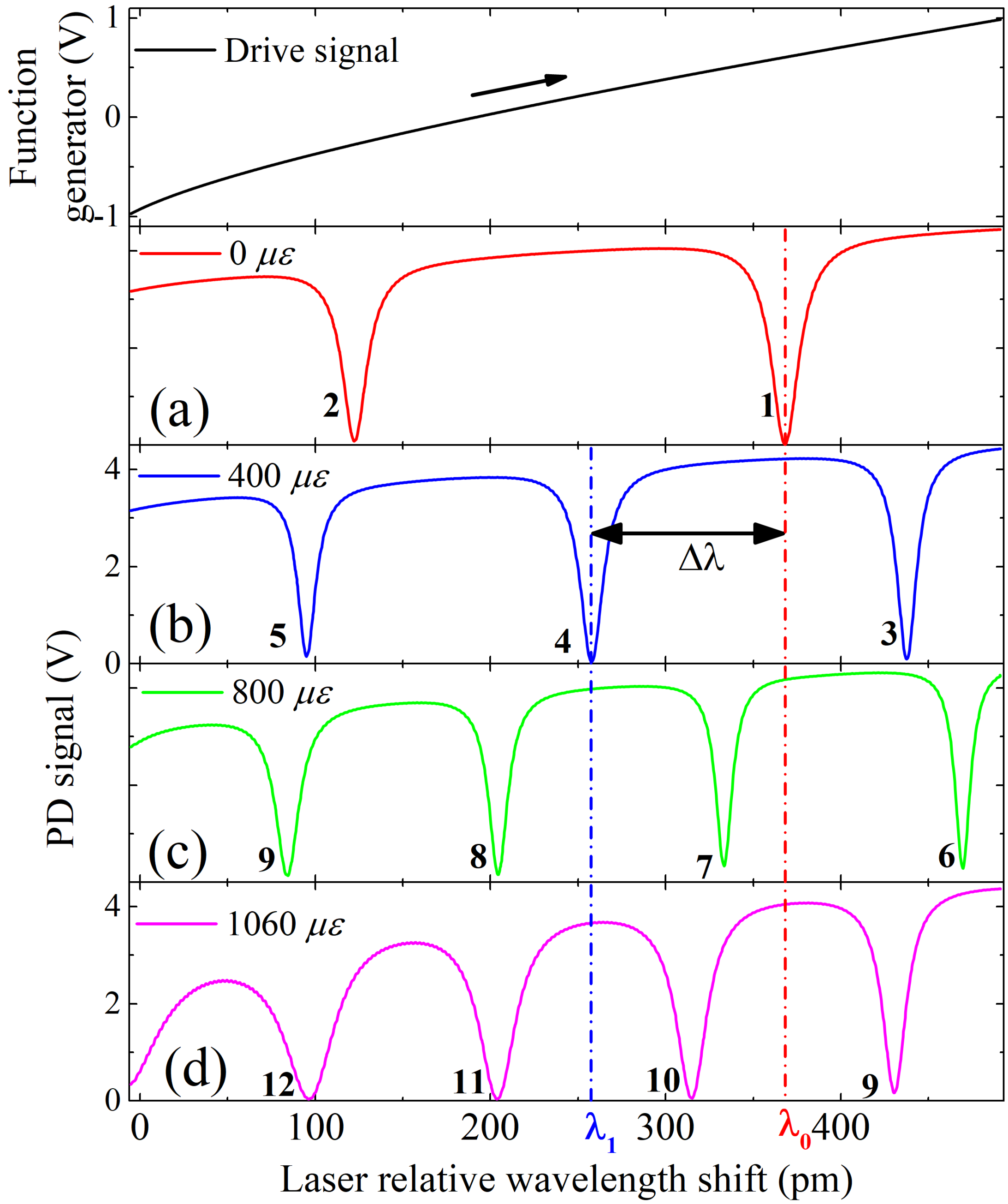

Figure 2.12: Scanning signal to drive the current controller for the laser (upper most) and the reflection spectra when different strains of (a) 0 $\mu\varepsilon$, (b) 400 $\mu\varepsilon$, (c) 800 $\mu\varepsilon$, and (d) 1060 $\mu\varepsilon$ were applied to CFBGs sensor.

Figure 2.12 shows the scanning signal that drove the current controller for the DFB laser and the measured reflection spectra of the sensor when different strain levels of 0, 400, 800 and 1060 $\mu\varepsilon$ were applied to the sensor. Although both the rising and falling edge of the wavelength scanning can be used for wavelength shift demodulation, here we only show the results obtained from the rising edge. When an arbitrary strain applied, the order of the notches in the scanning range were identified by measuring the spectral interval between them and match to the results shown in Fig. 2.9. Absolute wavelength shift can be calculated by measuring the precise location of a single notch in the tuning range with the initial notch location. Notches location within the scanning range are recorded and converted to relative wavelength based on the laser calibration curve. The unique spectral spacing provides the order of each notch even with only one scanning frame captured by the DAQ and enables absolute strain measurement. Specifically, the spectral notch at longer wavelength shown in Fig. 2.12(a) was set as the initial notch and its wavelength position at zero strain was recorded (red dot line). The order of the initial notch was named as 1 for reference. When arbitrary strain was applied on the sensor, notches position and spectral spacings are measured. The wavelength difference between Nth notch and the 1st notch is given by

$$L = \sum_{i=1}^{N-1} S_i \tag{2.9}$$

where S_i is the spectral interval between notch i and notch $i + 1$. As an example, assume the notch N is the first notch λ_1 located at the wavelength shorter than λ_0 (e.g. notch 4 in Fig. 2.12(b)). The wavelength interval $\Delta\lambda$ (see Fig. 2.12(b) between reference λ_0 and λ_1 can be measured with high resolution by this wavelength-scanning method, then the total wavelength shift caused by the strain applied on the sensor is given by $\Delta L = L - \Delta\lambda$.

As there were 12 spectral notches within a spectral bandwidth of 1.6 nm available for measurement, the strain measurement range is over 1000 $\mu\varepsilon$. Fig. 2.13 shows the measured wavelength shift as a function of applied strain which varied from 0 $\mu\varepsilon$ to 1060 $\mu\varepsilon$ in the step of 133.4 $\mu\varepsilon$. The sensor system shows excellent linear response with a strain sensitivity of 1.31 pm/$\mu\varepsilon$.

The resolution of strain measurement was characterized by continuously monitoring the wave-

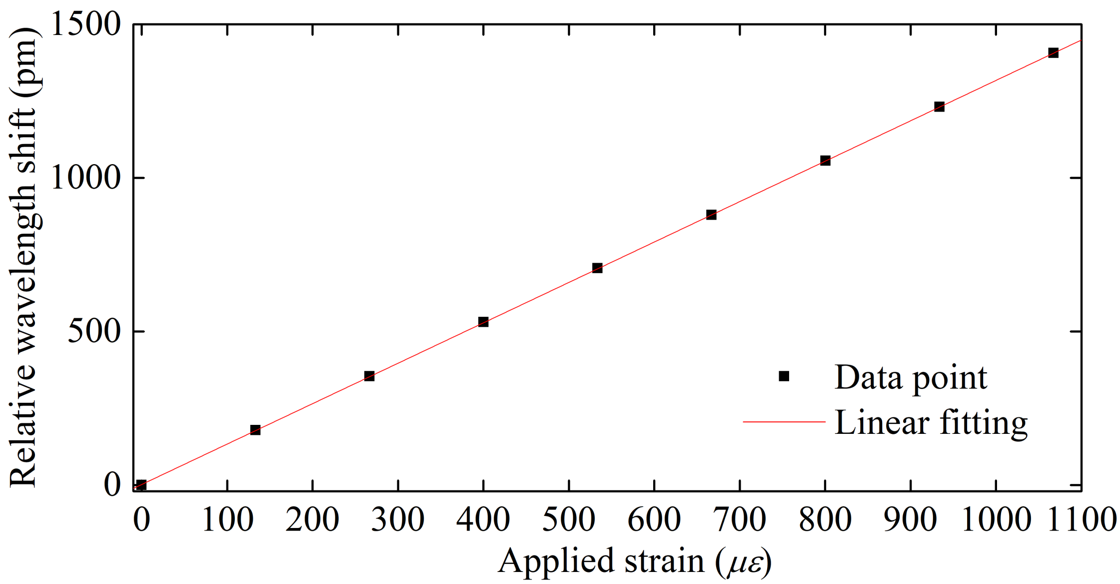

Figure 2.13: Measured wavelength shift with strain applied on the CFBG-FPI sensor.

length position of a spectral notch when no strain was applied on the sensor. The wavelength position of one spectral notch was continuously monitored for 0.6 s and the results (after conversion to strain) are shown in Fig. 2.14 with a standard deviation of 0.033 $\mu\varepsilon$. A slow drift toward lower strain may also be present, as indicated by the linear fitting of the results (red curve in Fig. 2.14). The drift is believed to arise from the laser wavelength drift from ambient temperature variation of the laser diode. The laser wavelength can be stabilized by an external wavelength reference, such as a reference fiber Bragg grating or a reference FPI.

2.4.3 Dynamic strain measurement

With the high-speed wavelength scanning of DFB lasers through current injection modulation, the sensor is also suitable for measurement of dynamic strains. The dynamic strain measurement setup is shown in Fig. 2.15. The sensor was glued on the center-line of a cantilever beam made from aluminum. The free end of the beam was excited by an electromagnetic shaker. A 20 Hz sinusoidal signal is generated by a function generator and amplified to drive the shaker. The wavelength sweeping rate of the DFB laser was set to 1000 Hz with the same bias current for high speed demodulation with a peak-to-peak current of 150 mA (corresponding to 3V). Calibration of laser

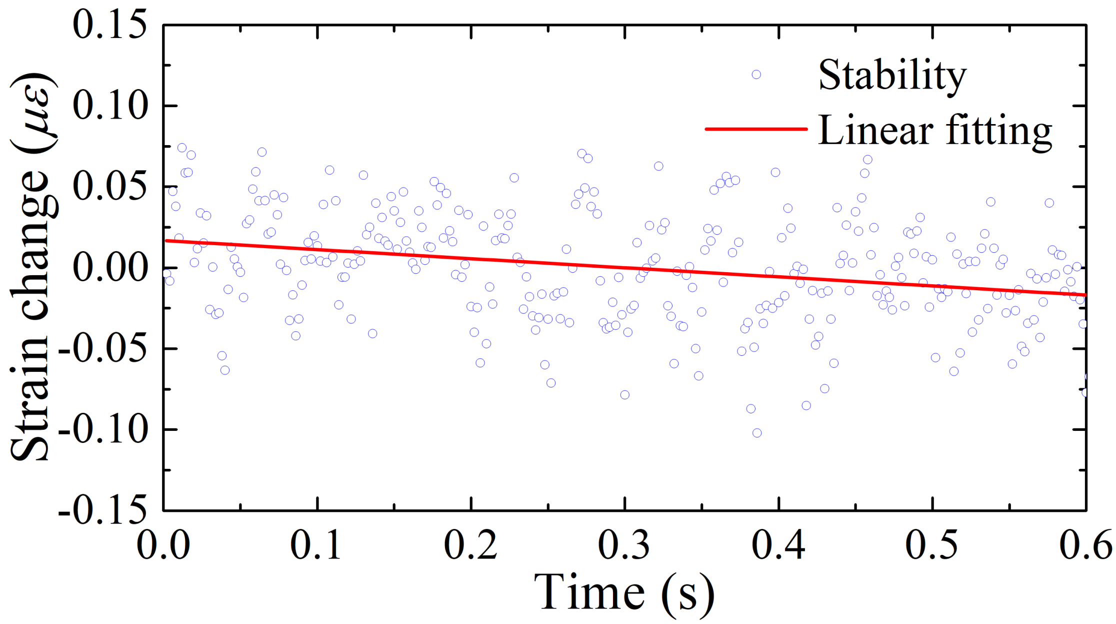

Figure 2.14: Characterization of sensor resolution: signal fluctuations when sensor was free from strain.

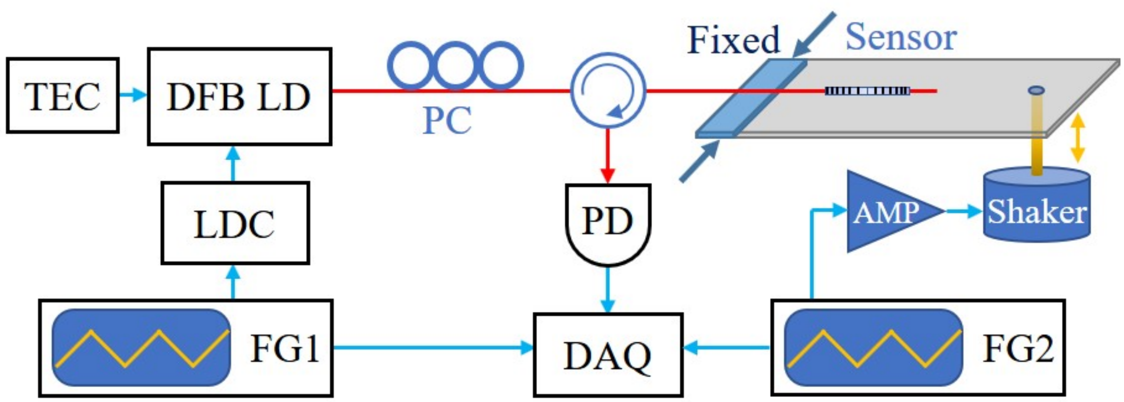

Figure 2.15: System setup for dynamic strain measurement. AMP: amplifier; TEC: temperature controller; LDC: laser diode current controller; FG: function generator; PC: polarization controller; DAQ: data acquisition.

wavelength to the laser injection current was performed to obtain the accurate wavelength positions of the sensor spectral notches. Even though the DFB laser scanning speed was over 30 times larger than the average strain changing speed, the effect of the laser wavelength scanning direction relative to the moving directions of the spectral notches should be considered. This effect is only present in dynamic strain measurement. When static strain is applied to the sensor, the spectral notch positions measured using the wavelength up scanning and down scanning of the DFB laser are identical, as shown in Fig. 2.16.

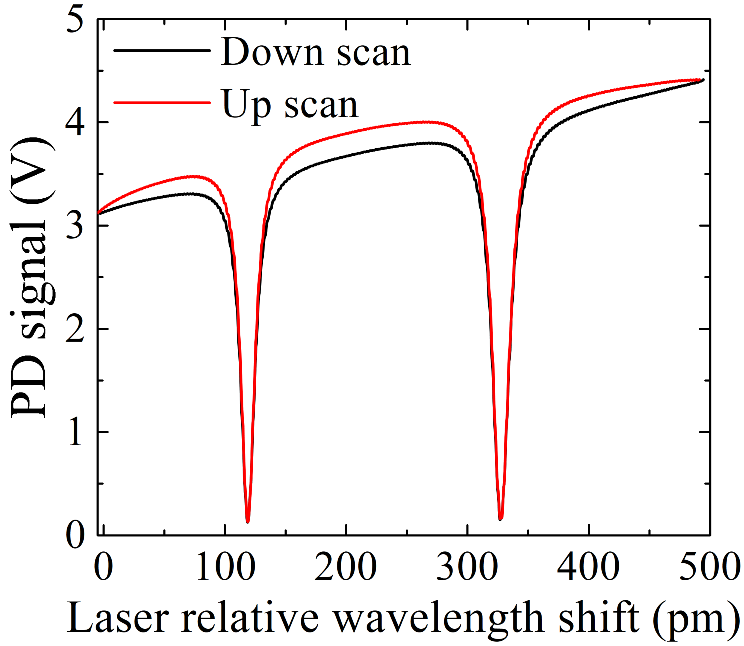

Figure 2.16: Measured spectra using the up and down scanning of the DFB laser when the sensor was under static strain.

However, under dynamic strain condition, if the laser wavelength and the spectral notches move in the same direction, it takes extra time for the laser wavelength to record the spectral notch (up scanning curve in red) compared to the case of static strain where the notches are stationary. Conversely, if the laser wavelength and the spectral notches move in opposite directions, it takes less time for the laser wavelength to meet the spectral notches (down scan curve in black). As a result, the wavelength position of spectral notch may be different when different directions of the wavelength scanning are used for wavelength measurement, as shown in Fig. 2.17.

Measurement errors could be introduced without considering the spectral shift of the notches during the dynamic strain change. Here, as each period of the wavelength scanning consists of a wavelength ramp up and a ramp down, we use the average position of each spectral notch calculated from both up and down ramps. The averaging can effectively eliminate the error caused by dynamic strain change.

The blue solid line in Fig. 2.18 shows the dynamic strain signal measured by the CFBG-FPI

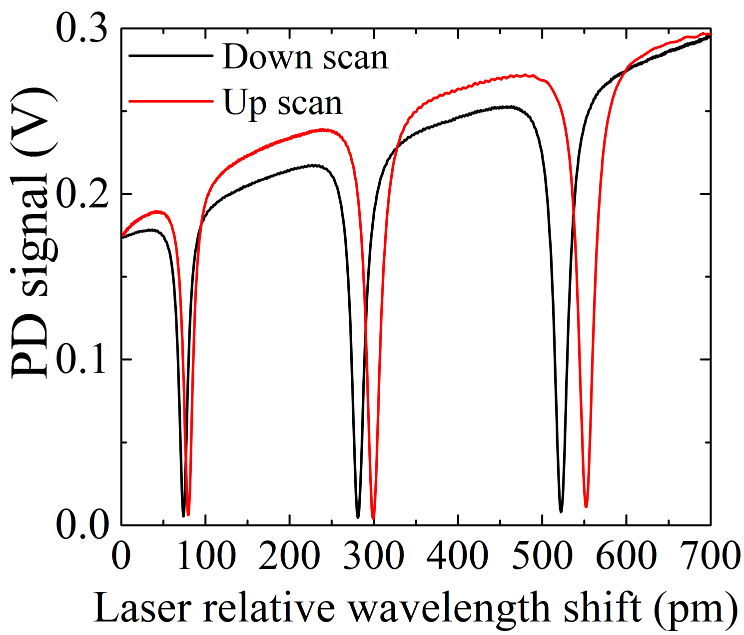

Figure 2.17: Measured spectra using the up and down scanning of the DFB laser when the sensor was under dynamic strain.

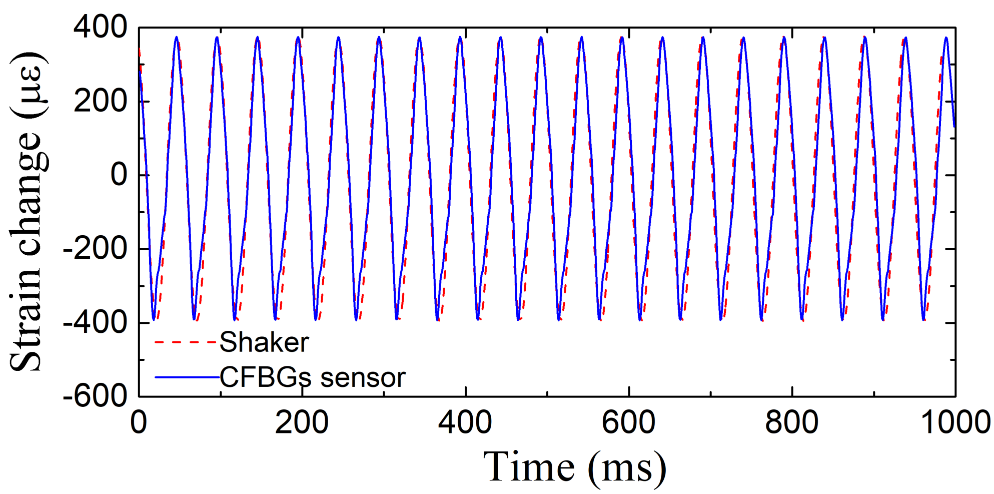

Figure 2.18: Measured dynamic strain change by the CFBG-FPI sensor. Red dash line: shaker signal for evaluation.

sensor, showing a 20 Hz, 768.6 $\mu\varepsilon$ peak-to-peak sinusoidal dynamic strain. Red dot line is the electronic signal used to drive the shaker. The average strain changing rate is 30.7 $\mu\varepsilon$/ms with a maximum strain change rates about twice of the average strain change rate for sinusoidal signal. The DFB laser tuning range is 691 pm, corresponding to a tuning rate of 1055.0 $\mu\varepsilon$/ms, which is sufficient to track the dynamic strain change. Higher tuning frequency with larger tuning voltage can be used for higher strain change rate. The distortion of the CFBG-FPI sensor signal mainly comes from the jerking movement of the shaker itself.

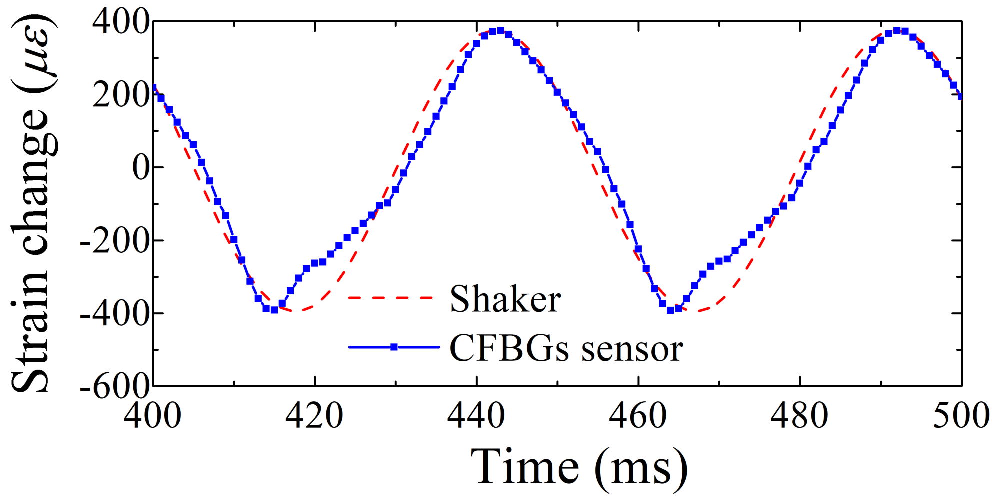

Figure 2.19: Zoom-in of the measured dynamic strain change by the CFBG-FPI sensor. Red dash line: shaker signal for evaluation.

2.5 Summary

This chapter discussed the analytical and numerical simulations on the spectra of CFBGs and CFBG-FP sensors. We introduced he grating spectrum is described based on the coupled mode equations. The transform matrix method is applied to solve these equations to generate the optical spectrum of grating with chirped structures. We also addressed the configuration of chirp direction and the effects to the spectra.

Then we proposed and demonstrated a novel absolute strain measurement system using an FPI formed by cascaded CFBGs with opposite chirp directions demodulated by a wavelength-scanning DFB laser. Due to the different and unique spectral intervals of the notches in the wavelength bandwidth used for measurement, the spectral notches can be unambiguously recognized in each spectral frame without the need for fringe counting. Using this principle, we demonstrated high-resolution and absolute static and dynamic strain measurement. The static strain experiment result shows a measurement range of 1000 $\mu\varepsilon$ with good linearity using 12 spectral notches within 1.6 nm effective bandwidth. The system resolution was 0.033 $\mu\varepsilon$ with a sensitivity of 1.31 pm/$\mu\varepsilon$. A 20

Hz, 768.6 $\mu\varepsilon$ peak-to-peak sinusoidal strain signal was tracked successfully. The laser wavelength scanning rate was 1055.0 $\mu\varepsilon$/ms and can be improved by increasing the frequency and/or the amplitude of the scanning signal. The above results show great potential of utilizing the CFBG-FP sensors for vibration and ultrasound detection system.

CHAPTER 3

ACOUSTIC EMISSION SENSORS BASED ON HIGH-FINESSE SHORT-CAVITY FPI

Part of the material in this chapter has been published in

- *"Fiber-optic acoustic emission sensor based on a chirped FBG pair for crack detection in aluminum plate." 11th International Workshop on Structural Health Monitoring 2017: Real-Time Material State Awareness and Data-Driven Safety Assurance, IWSHM 2017. DEStech Publications, 2017*
- *"Ultrasensitive ultrasound detection using an intracavity phase-shifted fiber Bragg grating in a self-injection-locked diode laser." Optics Letters vol. 44, no. 22, pp. 5525, 2019*
- *"Effect of Laser Polarization on Fiber Bragg Grating Fabry-Perot Interferometer for Ultrasound Detection," IEEE Photonics Journal, vol. 12, no. 4, pp. 1, 2020*

3.1 Crack detection with fiber-optic acoustic emission sensor based on a chirped FBG pair

In this section, a fiber-optic acoustic emission (AE) sensor system for the detection of AE signals generated from cracks within an aluminum plate is described. The sensor head consists of a pair of tandem chirped fiber Bragg gratings (CFBGs) that form a Fabry-Perot type interferometer (FPI). This CFBG-FPI features a series of resonant wavelength notches in the reflection spectrum, which are subject to the same wavelength shift as the sensor is stretched or compressed by AE signals. By locking a tunable laser to the slope of any individual notch, the AE induced high-frequency wavelength shift is converted into intensity variation. Using the sensor system, AE signals generated by three different types of sources, i.e., PZT actuator, pencil break, and cracks within aluminum plates, are detected and compared. Our experimental results suggest that cracks in the aluminum plates gave birth to broadband AE with peak intensity spanning over 100 kHz to 350 kHz.

3.1.1 Introduction

Acoustic emission (AE) signals with the frequency ranging from 100 kHz to 1 MHz are commonly regarded as fingerprint of damage-related structural evolution, such crack initiation and growth, corrosion, fiber breakage, etc. Therefore, nondestructive AE sensors are attractive in the field of structural health monitoring. As one of the most promising techniques, optical fiber based AE sensors are extremely competitive in terms of sensitivity, size, weight, multiplexing capability, and immunity to electromagnetic interference [33]. Among them, fiber Bragg grating (FBG) based AE sensors are attractive due to their easy operation and multiplexing capability [34, 35, 35, 36, 37]. The AE signals impinged on the FBG introduce strain within the fiber and thus shifts the Bragg wavelength. A FBG-based AE senor typically rely on a narrow-linewidth laser locked to the slope of a wavelength peak or notch and the wavelength shift is converted to intensity modulation. In practice, the tiny AE-induced wavelength shift is often superimposed on a large background shift caused by temperature and/or strain variation. Intuitively, a high performance laser with wide tuning range can be used to accommodate the large background wavelength shift. However, the cost would be unacceptable for most of the practical applications. Thus, a low cost laser, such as DFB semiconductor laser, is more desirable in practice. In this situation, the wavelength tuning range would be too limited to cover the large background wavelength shift. To tackle the above problem, we recently proposed an AE sensor system using a pair of tandem chirped FBGs (CFBGs) and smart feedback control [17]. The CFBG pair forms a Fabry-Perot interferometer and thus produces a series of resonant notches, a narrow linewidth laser is locked to one of the wavelength notches. As the background shifts the locked notch out of the laser tuning range, a new notch moves in and the laser is unlocked from the previous notch and relocked to the new one by resort to a smart feedback control unit. Thus, the large background shift is accommodated by the sensor system.

In this section, using the above CFBG-based AE sensor system, we investigate the detection of AE signals generated by pencil break and cracks within an aluminum plate. A comparison between these two difference sources will be given.

3.1.2 System and operation principle

The condensed system demonstrating the principle of operation is schematically shown in Fig. 3.1. Output of the laser diode, which is modulated by a current and temperature controller, is injected into the fiber sensor head and the reflected signal is directed to a photo-detector via a circulator. The converted electrical signal from the photo-detector provides feedback to a servo controller which is responsible for the input of the laser current driver. Through an embedded low-pass filter of the servo controller, the AE signal (AC component) from the photo-detector is eliminated and the remaining DC component is modulated by a proportional-integral controller. Using this close-loop feedback system, the output wavelength of the laser diode is locked around the quadrature point on the slope of any notch within the reflected spectrum of the CFBG pair.

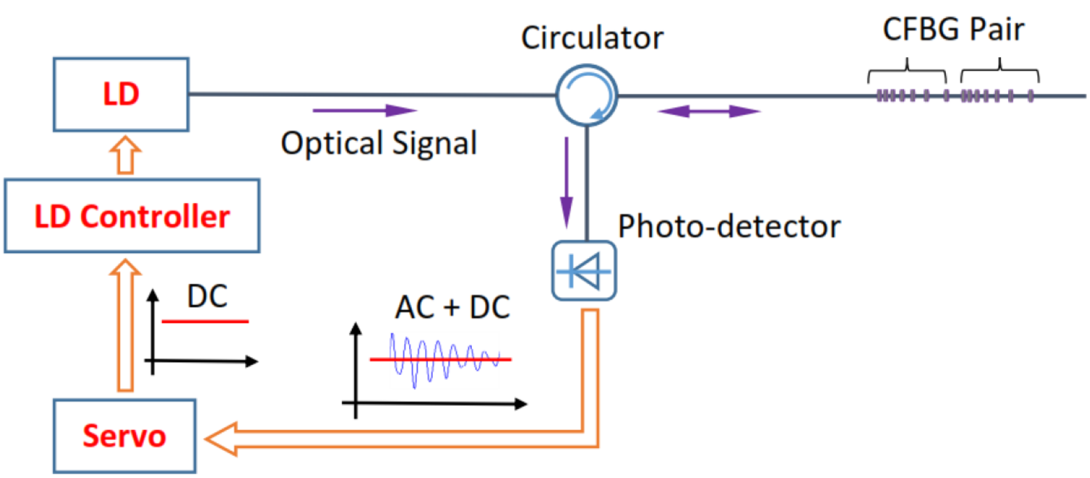

Figure 3.1: Schematic of the crack detection system. LD: Laser diode.

As depicted above, the sensor head is composed of a pair of the same CFBGs. For each CFBG, the reflection spectrum spans a couple of nanometers. The two cascaded CFBGs thus form literally a Fabry-Perot cavity, featuring a series of resonant wavelength notches in the reflection spectrum, as exhibited in Fig. 3.2. As the AE-induced stretching and compression are exerted on the sensor head, all the notches are shifted simultaneously and equally. Therefore, no matter which notch the laser is locked to, the AE signal can be picked by the sensor. Figure 3.3 schematically shows the detected AE signals by two neighboring notches. The AE-induced wavelength shift is converted into intensity change due to the fluctuation of reflectivity at the laser wavelength. Through an additional smart feedback control unit as elaborated in detail in our previous work [17], as one notch is knocked out of the laser tuning range by a large background disturbance, a new notch jumps in and takes over through the smart control. However, without the need to demonstrate the jumping again, the smart control is not incorporated in this section.

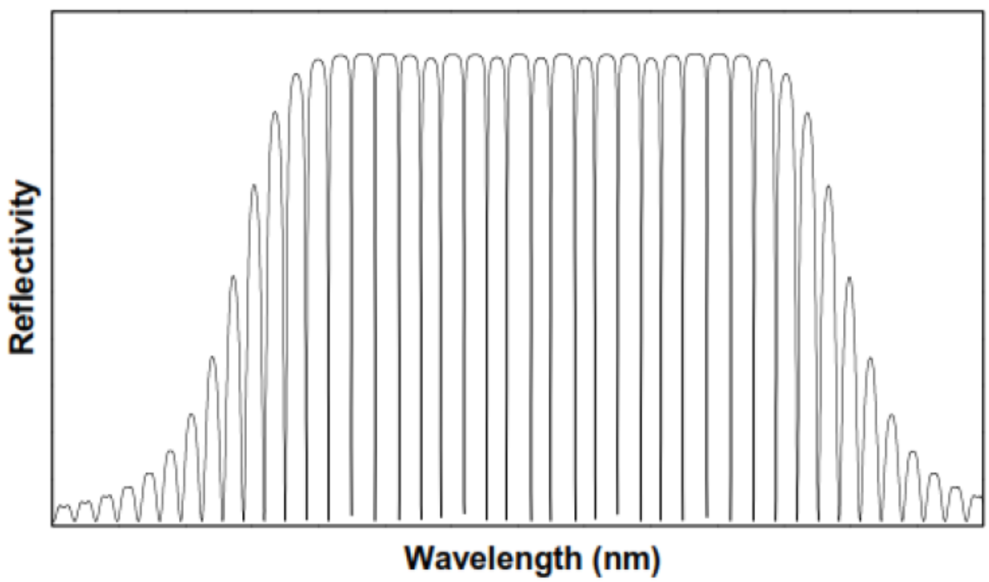

Figure 3.2: Reflection spectrum of the CFBG-FPI.

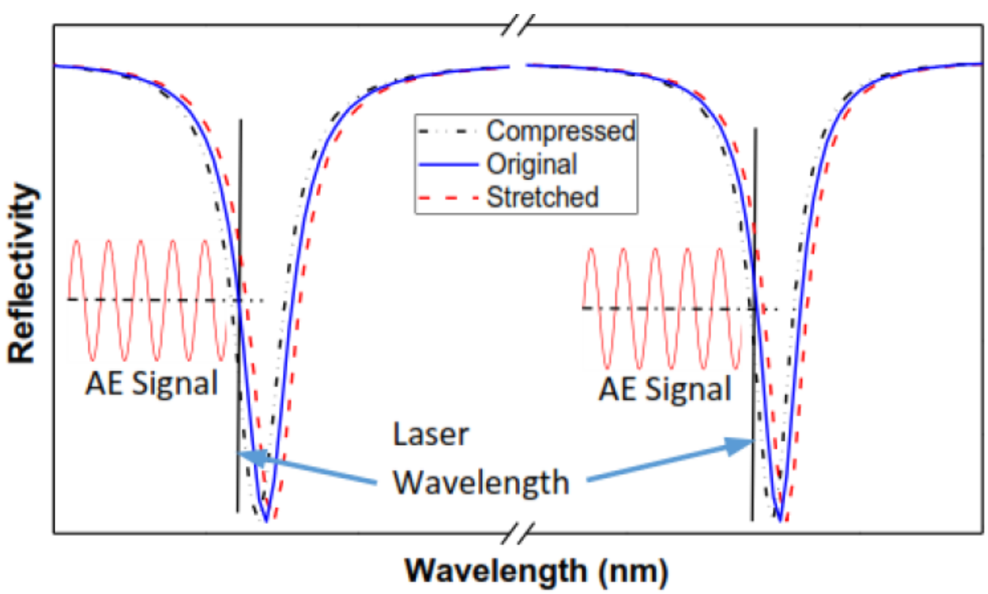

Figure 3.3: Principle of AE signal detection.

3.1.3 Experimental setup and results

Schematic representation of the detailed experimental setup is shown by the block diagram in Fig. 3.4. The LD was a tunable laser purchased from New Focus (Model 6328-H), and the LD controller was from the same vender (Model 6300). The servo controller (LB1005, New Focus) used a proportional-integral (PI) negative feedback control with a configurable cutoff frequency. The photodetector was purchased from Thorlabs (Model DET01CFC). The AE signal from the fiber sensor went through a broadband amplifier (Model AE2A, Physical Acoustics Co.) set at a gain value of 26 dB and a band pass filter (Model 3202R, Krohn-Hite) set at the range of 60 - 1000 kHz. The AE signal from the reference PZT sensor was amplified by 40 dB via a preamplifier (Model 5676, Olympus). Both PZT actuator (HD50) and sensor ($R15\alpha$) were purchased from Physical Acoustics Co. The two CFBGs were in contact and their specs were the same with a length of 10 mm and spectrum depth of 15 dB, the chirp rate of the phase mask was 4 nm/cm and the center wavelength was around 1545 nm.

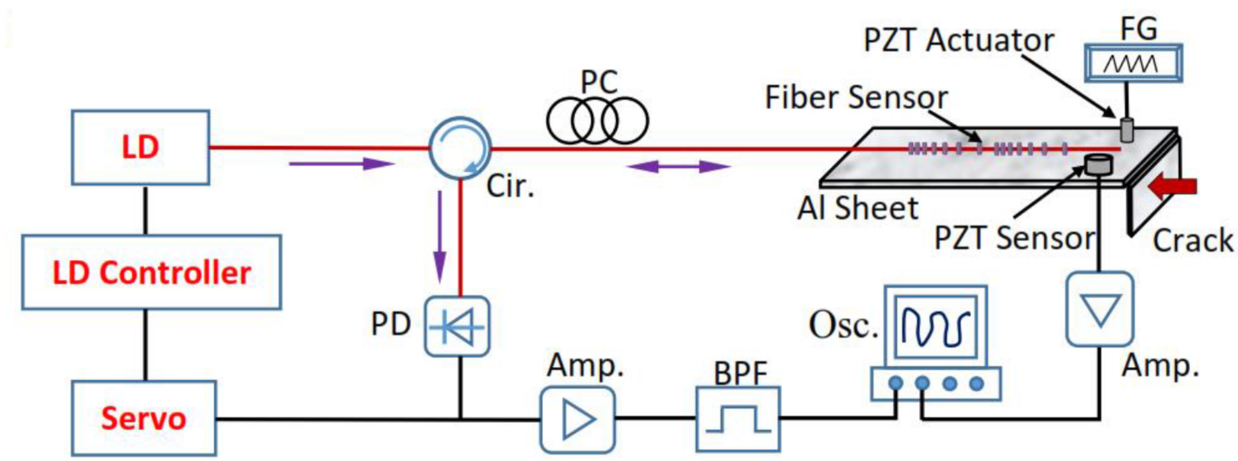

Figure 3.4: Schematic diagram demonstrating the crack AE detection system. LD, laser diode; PD, photo-detector; Cir., circulator; PC, polarization controller; Amp., amplifier; BPF, band-pass filter; Osc., oscilloscope; FG, function generator.

As described in the previous section, the laser wavelength was locked to one of the wavelength notches of the sensor through a close-loop feedback control. A polarization controller (PC) was incorporated to select one of the polarization states. The sensor head was attached to an aluminum sheet. In the meantime, one PZT sensor was placed in the vicinity of the fiber sensor for comparison. In addition to the AE signals originating from cracks within the sheet as described below, AE signals induced by PZT and pencil break were also investigated. Thus, another PZT actuator was also attached.

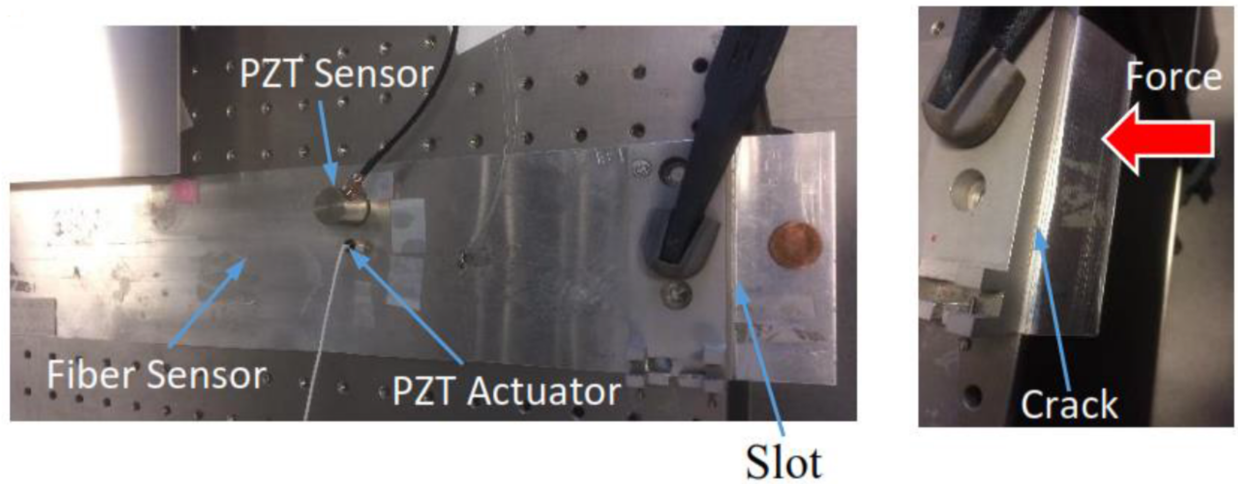

Figure 3.5: Photograph of the aluminum sheet on which a slot was initially introduced (left) and the crack expanded as part of the aluminum sheet was bent downward (right).

The aluminum sheet was clamped on the edge of an optical table. A tiny slot was initially engraved on the top surface and then the suspended part was pressed downward so that cracks were generated during the bending, as shown by the photos in Fig. 3.5. When any AE signal turned around, the oscilloscope was triggered to capture the waveform.

Because the sensitivity is proportional to the slope of the notch, the bandwidth of the notch is a directly related to the sensitivity. With the same depth, the smaller the bandwidth the higher the sensitivity. Thus, before the detection of AE signals, the wavelength notch that was used for sensing was first characterized, the results are shown in Fig. 3.6. It can be seen that the full width at half maximum is around 1.3 pm. Then the fiber sensor was used for the detection of AE signals. Firstly, the AE signals were generated by a PZT actuator operating in burst mode (3-cycle excitation at a frequency of 200 kHz), the results are shown in Fig. 3.7. It's apparent that both the PZT and fiber sensors caught the signals pretty well. Secondly, AE signal was generated by a pencil break

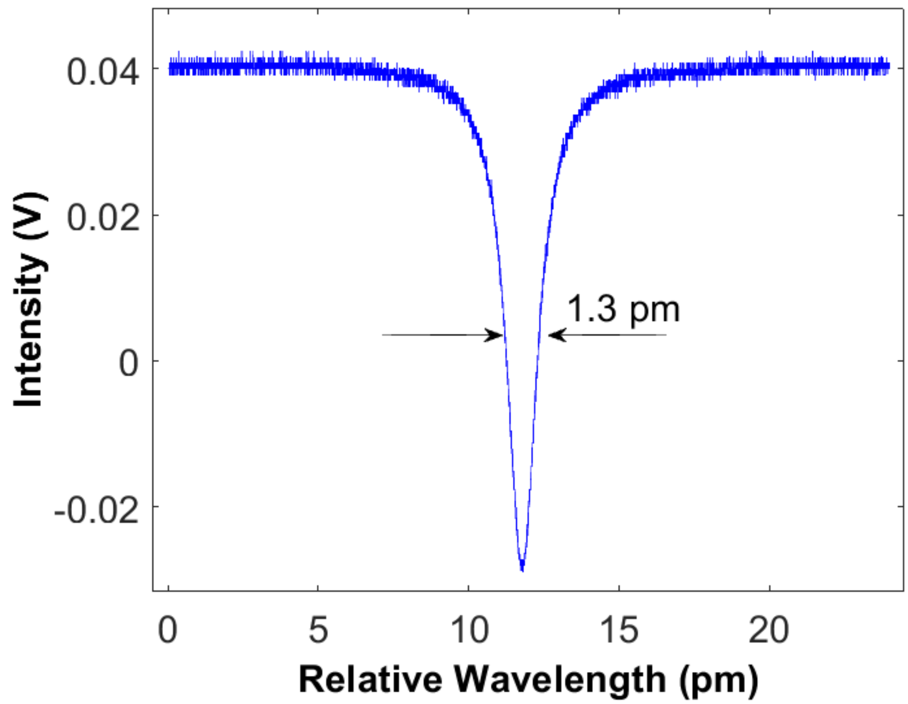

Figure 3.6: Spectrum of the wavelength notch used for AE detection.

and the captured signals are shown in Fig. 3.8. Again, both the PZT and fiber sensors worked very well in monitoring the AE signals. With the system verified for reliable interrogation, AE signals possibly generated from the cracks within the aluminum plate were monitored. One such AE waveform successfully captured by both PZT and fiber sensors is shown in Fig. 3.9.

In order to examine in detail the frequency range, fast Fourier transform (FFT) has been applied to the AE waveforms, the results are shown in Fig. 3.10-3.12. The FFT spectra in Fig. 3.10, 3.11, and 3.12 correspond to the temporal responses in Fig. 3.7, 3.8, and 3.9, respectively. The peak around 200 kHz in Fig. 3.10 coincides with the excitation frequency. For the pencil break shown in Fig. 3.11, the peak intensity resides around 100 kHz and the frequency extends to around 600 kHz with reduced intensity at higher frequency. In contrast, for the crack induced AE spectrum, the peak frequency covers a much broader range of 100 kHz to 350 kHz and the existing frequency extends to around 800 kHz. The comparison suggests that the crack induced AE covered a much broader frequency range than the pencil break did in our case.

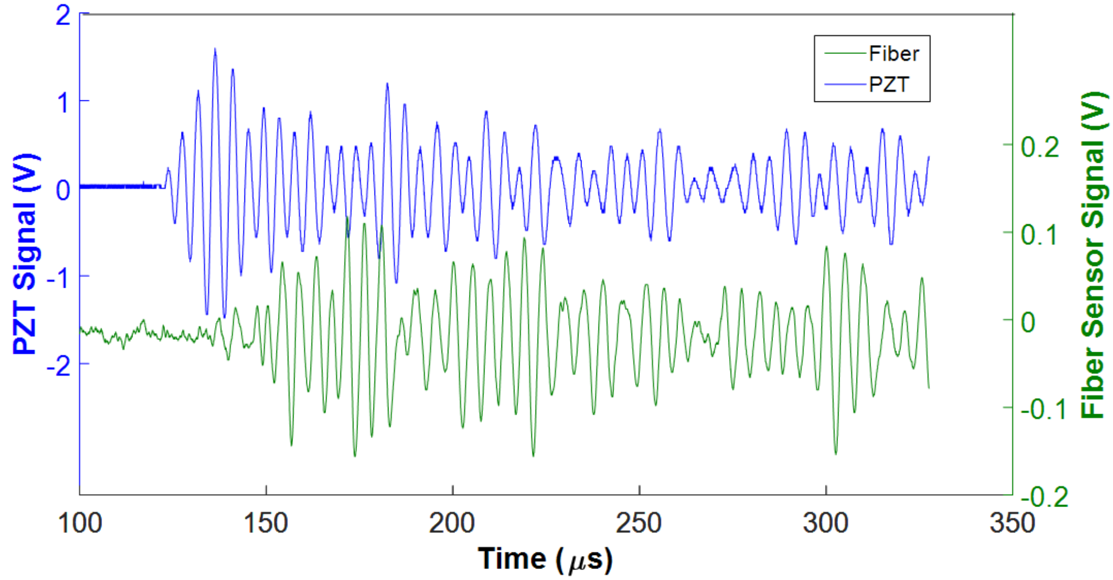

Figure 3.7: Captured AE signals when it was generated by PZT.

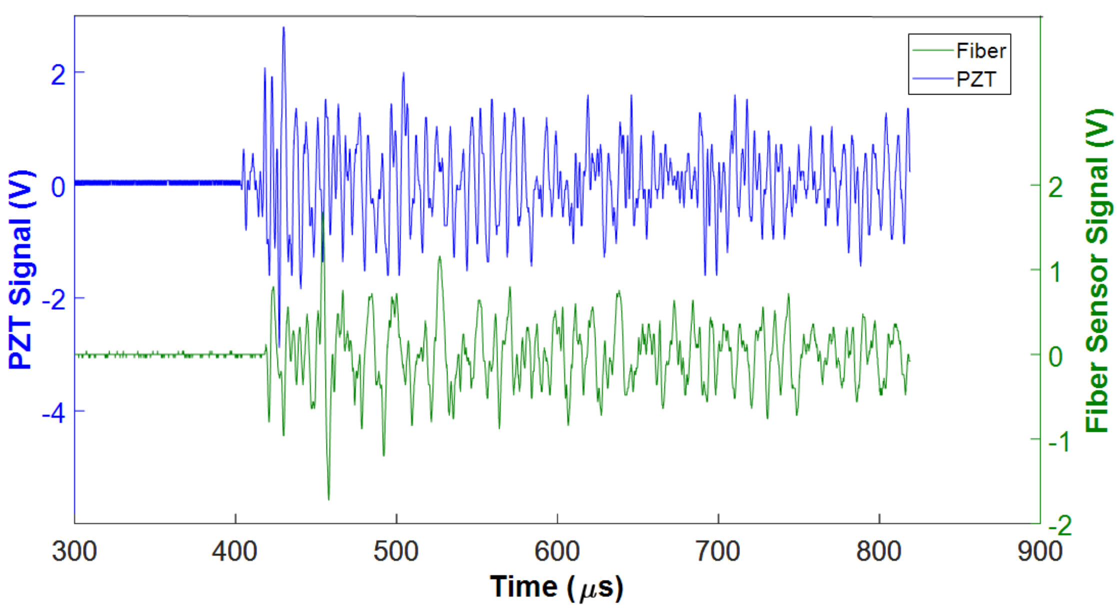

Figure 3.8: Captured AE signals when it was generated by pencil lead break test.

3.2 Ultrasensitive ultrasound detection using an intra-cavity phase-shifted fiber Bragg grating in self-injection-locked diode laser

In this section, we report a high-sensitivity fiber-optic ultrasonic sensor system using a self-injection-locked distributed feedback (DFB) diode laser where a π-phase-shifted fiber Bragg grating (πFBG) serves as both the locking resonator and the sensing element in a fiber ring feedback loop.

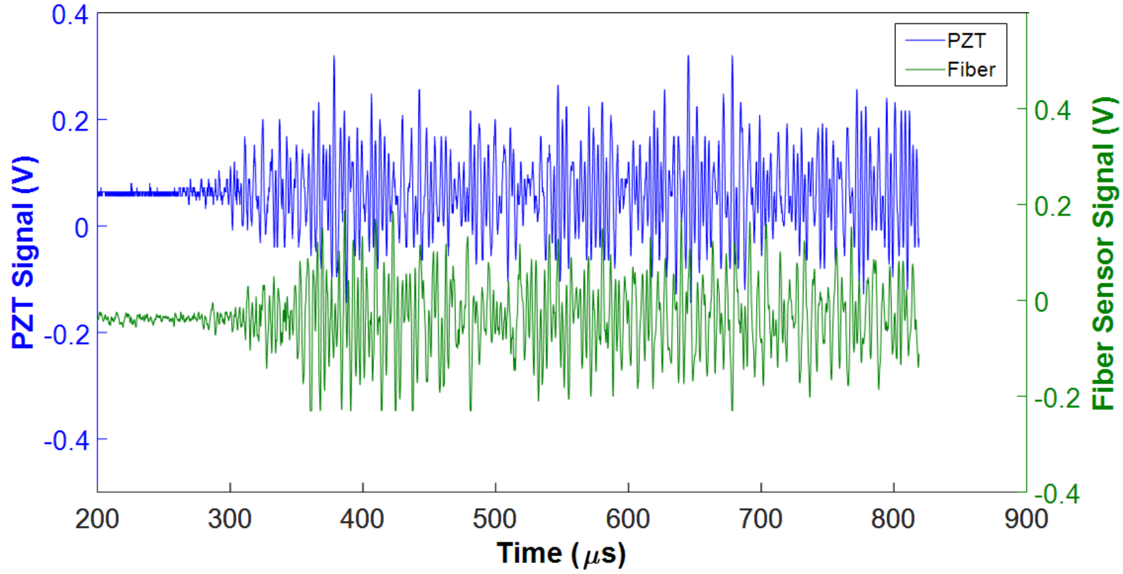

Figure 3.9: Captured AE signals when it was generated by crack within the aluminum plate.

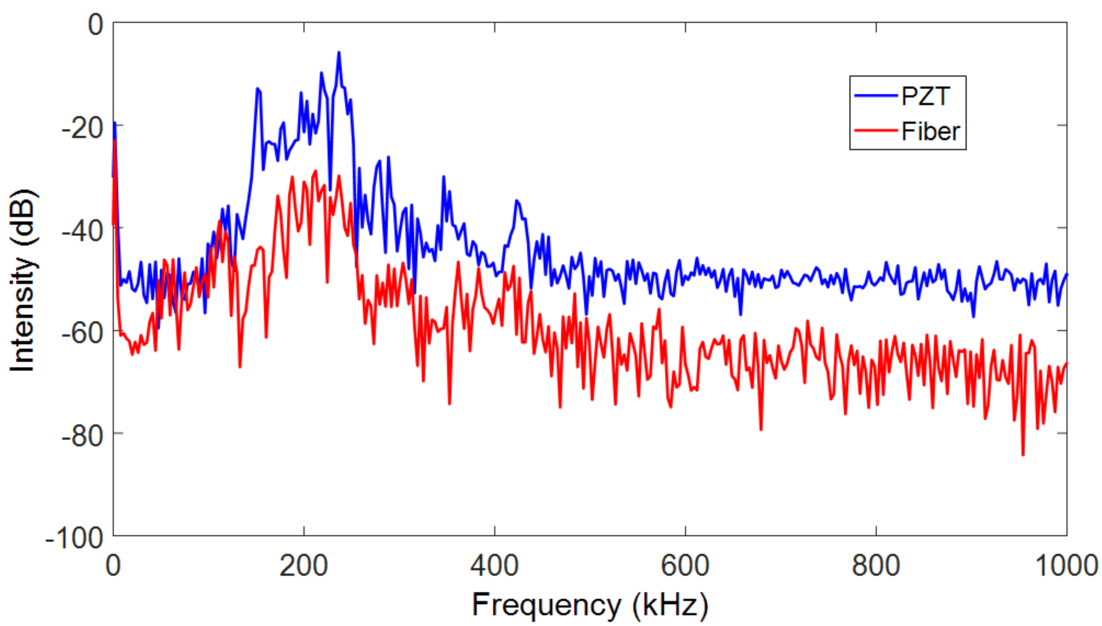

Figure 3.10: FFT spectrum of the AE signals generated by PZT.

By controlling the delay time of the feedback light through a fiber stretcher, the laser wavelength is locked to an external cavity mode on the spectral slope of the πFBG and the ultrasound-induced wavelength shifts of the πFBG is converted to laser intensity variation. The ultrasonic sensing scheme simplifies the feedback control because the self-injection locking automatically pulls the laser wavelength to the πFBG resonant wavelength. In addition, it improves the detection sensitivity

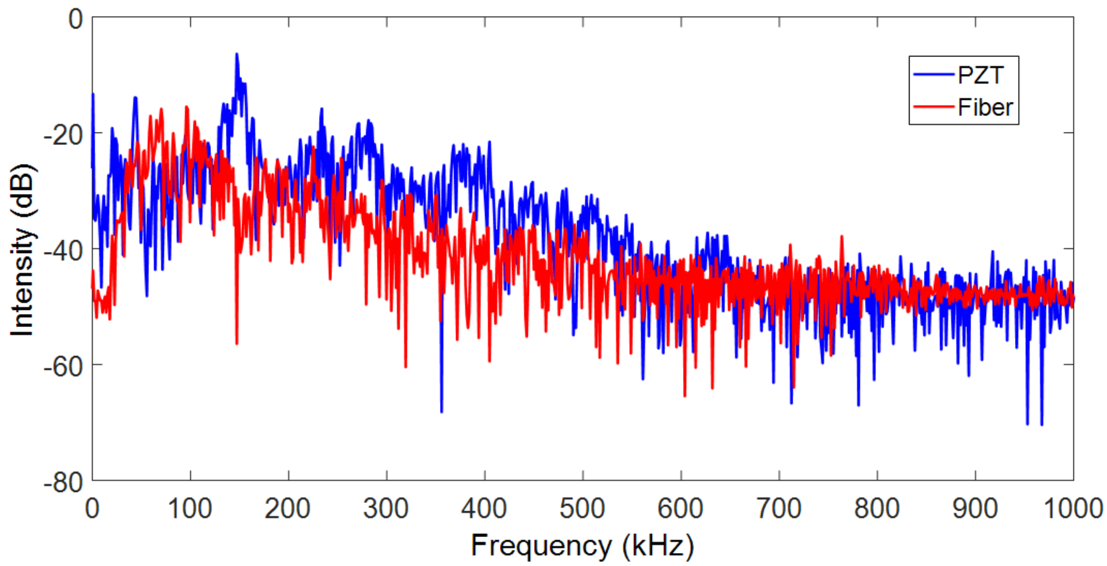

Figure 3.11: FFT spectrum of the AE signals generated by pencil lead break test.

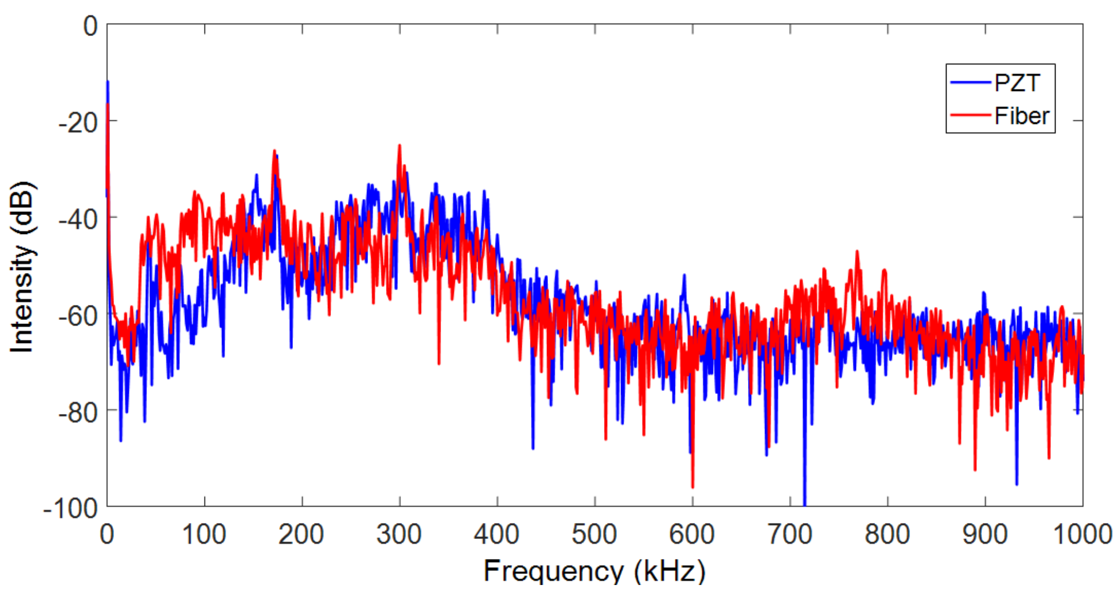

Figure 3.12: FFT spectrum of the AE signals generated by crack within the aluminum plate.

because of the frequency noise of the DFB laser is drastically reduced. We show that the sensor system achieves a strain sensitivity of 78 fε/Hz$^{1/2}$ at around 200 kHz.

3.2.1 Introduction

Ultrasonic sensors are widely used in a number of diverse applications including non-destructive testing [38], structural health monitoring [39], range measurement [40], and biomedical imaging [41]. High sensitivity is often needed for performance optimization in these systems. Compared to traditional piezoelectric sensors, fiber-optic sensors, particularly those based on fiber Bragg gratings (FBGs), exhibit many advantages such as small size, light weight, immunity to electromagnetic interference, corrosion resistance, and multiplexing capabilities. Due to the required detection speed, these sensors typically use a laser as the light source with edge filter detection method to demodulate the Bragg wavelength shift for high sensitivity. Specifically, the laser wavelength is locked to the linear region of the spectrum of an FBG sensor. The slope of the spectrum converts the ultrasound-induced spectral shift into intensity variations that can be measured by a photodetector (PD) [34, 42, 6]. The signal strength is proportional to the slope in the linear region of the spectrum of an FBG sensor. FBG-based optical resonators, such as π-phase-shifted FBGs (πFBGs) [43, 44] or chirped FBG Fabry-Perot interferometers [17], provides narrow spectral feature to increase the response to the ultrasound signal and the systems can often approach the signal-to-ratio (SNR) whose limit is set by the frequency noise of the laser. In these cases, a narrow linewidth laser with minimum frequency noise is the key for high-sensitivity ultrasonic detection. External cavity diode lasers (ECDL) based on dispersive components offer superior performance relative to conventional distributed feedback (DFB) or distributed Bragg reflector (DBR) diode lasers because of the high quality-factor the laser cavity resulting from the long cavity length. Although ECDL can offer superb performance in terms of frequency noise, the bulk size, the complexity of the cavity, and the stringent requirement on the optical alignment have limited their applications in fiber-optic ultrasound detection.

Laser frequency can be stabilized by locking the laser to an optical resonator. This can be achieved through an electrical locking technique where an error signal is generated to correct the deviation of the laser frequency [45]. Complicated and high-speed feedback control system is needed in this approach. Self-injection locking technique [46] is widely accepted as a powerful yet simple method for laser frequency-noise suppression. Unlike electronic locking schemes, self-injection locking is an all optical operation with significantly reduced system complexity. It has been demonstrated that low-cost semiconductor lasers, such as DFB diode lasers and Fabry-Perot diode lasers, can achieve remarkably narrow linewidth by locking the lasers to structures like external ring fiber cavity [47], fiber grating [48], whispering gallery mode resonator [49], confocal Fabry-Perot cavity [50]. However, the implementation of a self-injection locked laser as the laser source in a fiber-optic ultrasonic sensor system is not trivial because the laser wavelength needs to be tunable in order to be locked to the spectral slope of the sensor. Tuning the wavelength of a self-injected locked laser requires the synchronized adjustment of the resonator wavelength, the delay time of the optical feedback, and the free-running laser wavelength, which is a challenging task due partially to the difficulty in knowing the free-running laser wavelength when the laser is under locked state.

In this section, we propose and demonstrate an ultrasonic detection scheme with high sensitivity using a πFBG in a fiber-ring feedback loop of a self-injection-locked DFB semiconductor laser. The πFBG serves as both a locking component in the self-injection operation and the sensing element for ultrasonic detection. By using a relatively long delay line, the laser wavelength and tuning the feedback delay time (using a fiber stretcher), the laser wavelength is locked to an external-cavity mode on the slope of the πFBG transmission spectrum and ultrasound-induced wavelength shift of the πFBG is converted to laser-intensity variations. We show that the sensor system achieves a sensitivity of 78 fε/Hz$^{1/2}$ around 200 kHz. Although πFBGs have served as self-injection locking components for DFB lasers [51], this is the first report to use the feedback component as the sensing element for ultrasonic detection. Compared with other ultrasonic sensor systems based on πFBGs or other types of FBGs [17, 52], this system has the following two major advantages:

1. Self-injection locking effectively suppresses the laser frequency noise, allowing high sensitivity ultrasonic detection with low-cost semiconductor lasers.

2. It significantly simplifies the wavelength locking system, especially minimizes complex

electronic locking system.

Self-injection automatically locks the laser wavelength to the πFBG when the free-running laser wavelength is set close to the locking region by adjusting the temperature and current of the DFB laser. With the assistance of a simple fiber stretcher, the laser wavelength can be fixed at the slope of the sensor spectrum for maximal responsivity.

3.2.2 Principle of operation

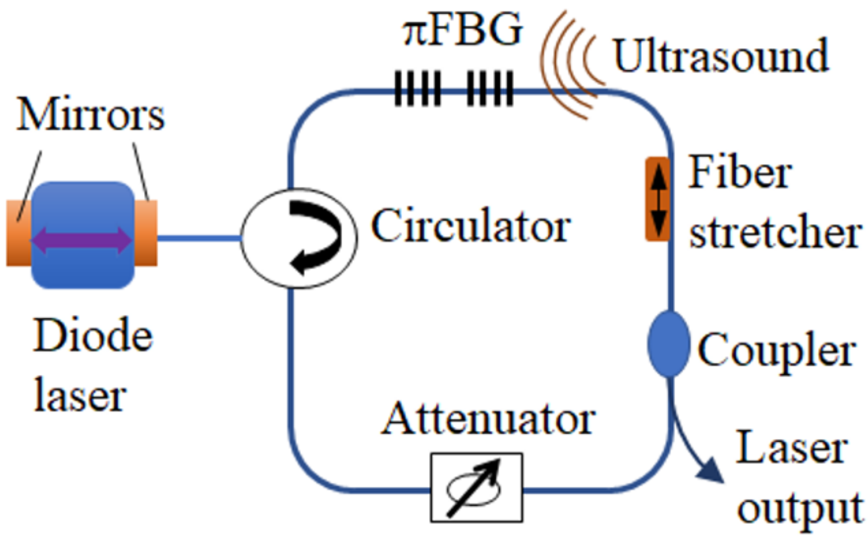

Figure 3.13: Schematic of the ultrasonic sensor system with the πFBG sensor inside the self-injection feedback loop.

The proposed ultrasonic sensor system is schematically shown in Fig. 3.13. The laser output from a diode laser is injected back to the laser cavity after it travels through a fiber ring that consists of a circulator, a πFBG, a coupler, an attenuator, and a fiber stretcher. The front mirror of the laser diode and the fiber ring forms an external cavity, whose transmission spectrum exhibits dense sinusoidal fringes (due to the relatively long external cavity length with an envelope determined by the transmission spectrum of the πFBG, as schematically shown in Fig. 3.14. By tuning the attenuator to obtain appropriate feedback coefficient, the laser can be locked to an external cavity mode around the transmission peak of the πFBG with significantly reduced laser linewidth and good locking stability. The locking point can be fine-tuned by adjusting the time delay of the feedback light (through, e.g. a fiber stretcher in the external cavity) to ensure the locking point is on the slope of the πFBG spectrum. Ultrasound that impinges onto the πFBG causes wavelength shifts of the πFBG but has little effect on the wavelength positions of the external cavity mode due to the long external cavity length (L_{ext}) relative to the πFBG length (L_{FBG}) and the ultrasonic wavelength (Λ). More specifically, the fiber length change (ΔL) in πFBG region caused by the ultrasound would result in a spectral shift of $\Delta\lambda_{ext} = \lambda\Delta L/L_{ext}$ for the external cavity mode and a spectral shift $\Delta\lambda_{FBG} = \lambda\Delta L/L_{FBG}$ for the πFBG. Because $L_{ext} >> L_{FBG}$, $\Delta\lambda_{ext} << \Delta\lambda_{FBG}$. In addition, $L_{ext} >> \Lambda$, the ultrasound induces both compressive and tensile strains on the external cavity fiber with their effects on the cavity length canceling out each other. As a result, the laser wavelength remains unchanged and the ultrasound-induced spectral shift of the πFBG is converted to laser intensity variations after the πFBG, which is tapped out of the fiber ring via a coupler and detected by a photodetector.

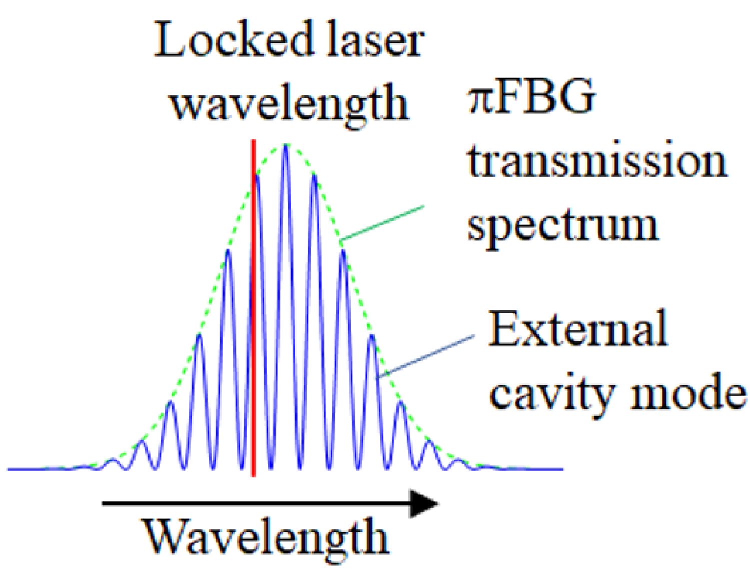

Figure 3.14: Illustration showing the laser line is locked to an external cavity mode on the slope of the πFBG transmission spectrum.Schematic of the ultrasonic sensor system with the πFBG sensor inside the self-injection feedback loop.

3.2.3 Experiments

The experimental setup for demonstration of the proposed ultrasonic detection scheme is schematically shown in Fig. 3.15. An 8-mm πFBG fabricated in-house using a 193 nm UV laser and a phase mask [53] was bonded along the center line of an aluminum plate to detect the ultrasonic waves generated from a commercial piezoelectric actuator (HD50, Physical Acoustics) glued at a position on the plate 80 mm away from the πFBG sensor. The laser source is a butterfly-packaged DFB diode laser operating at $\sim$ 1545.5 nm without an internal isolator. The isolator is a standard component inside the commercial DFB laser. Because of the DFB laser is sensitive to optical back reflections. Internal isolator is used to suppress back reflections to avoid output fluctuation and increase signal to noise ratio of the DFB laser. Therefore, stable single mode operation of the DFB laser can be achieved. Here in our experiments, a DFB laser was customized to remove the internal isolator. With such configuration, back reflections can easily return to the laser cavity to minimize to the frequency noise of the laser.

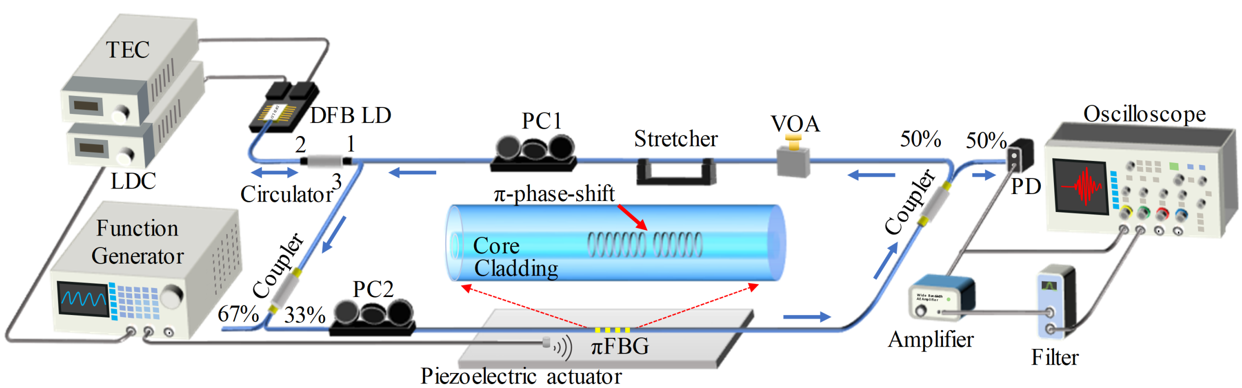

Figure 3.15: Experimental setup for DFB laser self-injection locking and AE signal measurement. TEC: temperature controller; LDC: laser diode controller.

The wavelength of the DFB laser diode can be tuned by adjusting the injection current with an experimentally measured tuning coefficient of 10.9 pm/mA at 25 °C. The light from the DFB laser is coupled to the fiber ring through a circulator, where the light first travels through a 33:67 coupler, used to tap out the light for analysis, and a polarization controller (PC) before reaching the πFBG sensor. The PC was used to align the laser polarization with one of the principle axes of the πFBG as birefringence was introduced from the πFBG fabrication process. The transmitted light from the πFBG was partially coupled out of the ring by a 50:50 coupler and detected by a photodetector (PD). The quasi-dc component of the signal from the PD was used for locking point analysis. The ac signal was amplified and filtered by a 50−500 kHz band-pass filter for ultrasonic signal analysis. The other half that remained in the ring was attenuated by a variable optical attenuator (VOA) before being injected back to the DFB laser through the circulator. For optimal locking, another PC was placed before the circulator to control the polarization of the light that was injected to the DFB laser. A fiber stretcher was placed between the VOA and PC to tune the external fiber-ring cavity length, and consequently the feedback delay time, through which the relative position of the locking wavelength to the peak of the πFBG can be precisely controlled. Compressing the fiber caused a shift toward the shorter wavelength (blue shift) of the locked laser. Conversely, stretching the fiber caused a shift toward the longer wavelength (red shift). The external cavity length is about 10 m, corresponding to free spectral range (FSR) of 10 MHz.

A piezoelectric actuator glued to on the plate was used to generate the ultrasonic pulses for testing. It was driven by a five-cycle sinusoidal burst wave centered at 200 kHz with a peak-to-peak voltage of 5 V is generated by a function generator. For comparison, the πFBG sensor was also interrogated by the same DFB laser in free running mode. In this case, the self-injection loop was opened at the position of the VOA so no laser was injected back to the laser. The laser wavelength was tuned to the spectral slope of the free running by manually adjusting the electrical current injected to laser through the current controller.

Figure 3.16 shows the transmission spectrum of the πFBG with a transmission peak at 1545.65 nm measured by an OSA with a spectral resolution of 20 pm. The detailed spectral profile of the central peak was measured by a scanning wavelength-tunable narrow linewidth (< 300 kHz) laser along with a PD, as shown in Fig. 3.17, which reveals that the central peak has a full-width at half-maximum (FWHM) of 2.6 pm (323 MHz) and a spectral slope of 0.39 pm^{-1} in the linear region.

When the laser is locked in the linear region of the πFBG, the ac signal V_s after the amplifier

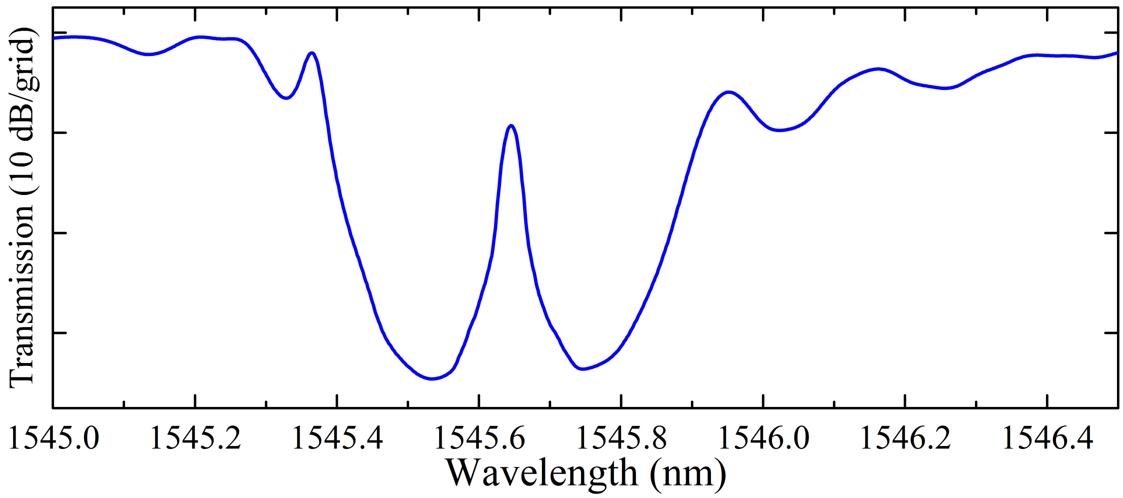

Figure 3.16: Transmission spectrum of the πFBG measured by an OSA.

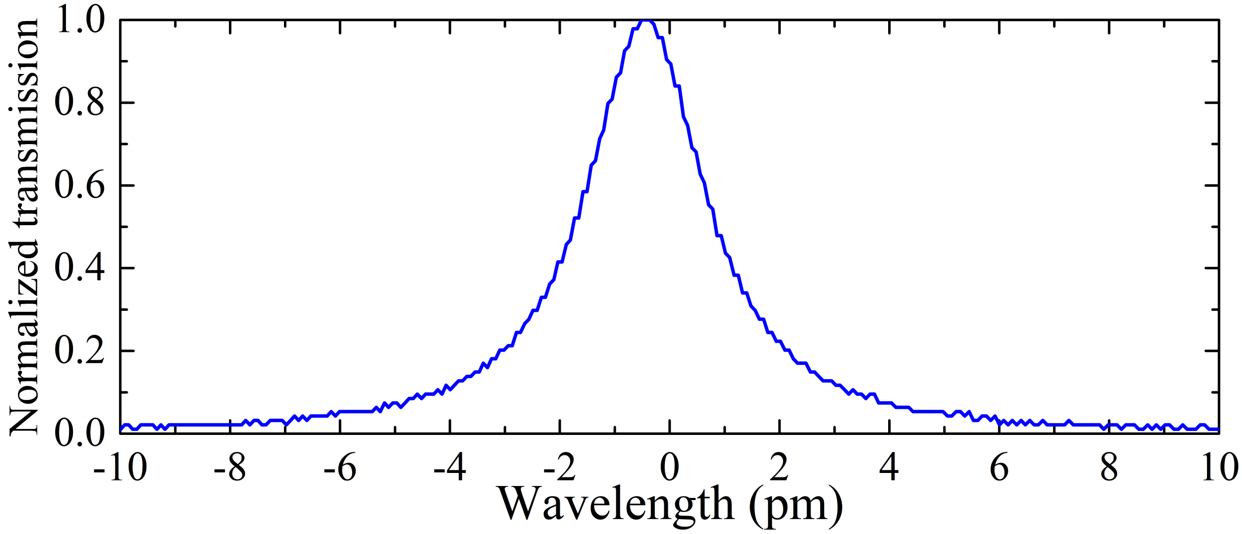

Figure 3.17: Transmission spectrum of the πFBG measured by a wavelength-scanning laser.

can be determined by

$$V_S = \Delta\lambda S_T V_{DC} G \tag{3.1}$$

where $\Delta\lambda$ is the Bragg wavelength shift of the πFBG induced by the ultrasound, S_T and T_{DC} are, respectively, the slope and transmission of the normalized transmission spectrum of the πFBG (Fig. 3.17) at the locked wavelength, V_{DC} is the detected DC signal voltage from the PD, and G is the gain setting of the amplifier.

The Bragg wavelength shift is proportional to the applied strain, which is expressed as $\Delta\lambda = a\varepsilon$.

a is the strain sensitivity of the Bragg grating, the expected value is $\sim$1.2 pm/$\mu\varepsilon$ when Bragg wavelength is around 1550 nm [54]. Therefore, the detected strain is expressed as:

$$\varepsilon = \frac{V_S}{aS_T V_{DC} G} \tag{3.2}$$

3.2.4 Results and discussion

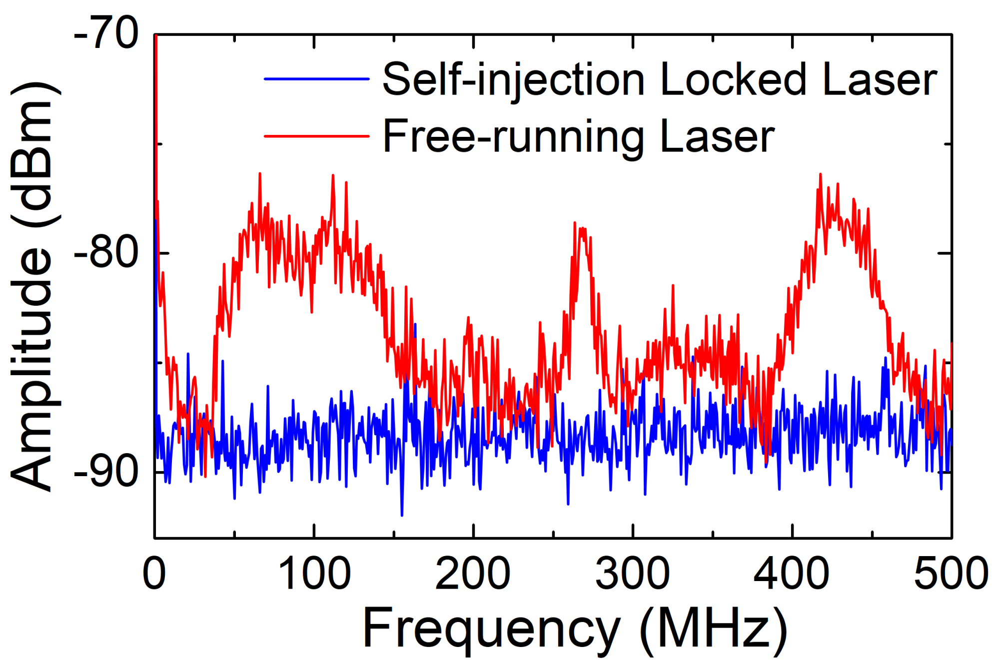

Figure 3.18: Noise behavior of the free-running DFB diode laser (red line) and the self-injection locked DFB diode laser (blue line) to the πFBG sensor.

The noise characterization of the DFB diode laser is examined first. The typical noise includes the relative intensity noise (RIN) and the frequency noise. In order to show frequency noise behavior, the slope of the sensor is used to amplify the frequency fluctuation of the laser. The noise behavior is measured by setting the laser wavelength at the maximum slope of the sensor peak which is also within the locking range. An electrical spectrum analyzer is connected to the PD. Figure 3.18 shows the noise of the free-running DFB diode laser (red line) and the self-injection locked DFB diode laser (blue line). It is clear to observe a flatten noise floor after the laser is self-injection locked. Also at low frequencies ($<$ 20 MHz) range, $1/f$ noise of the self-injection locked DFB diode laser drops quickly than the free-running mode.

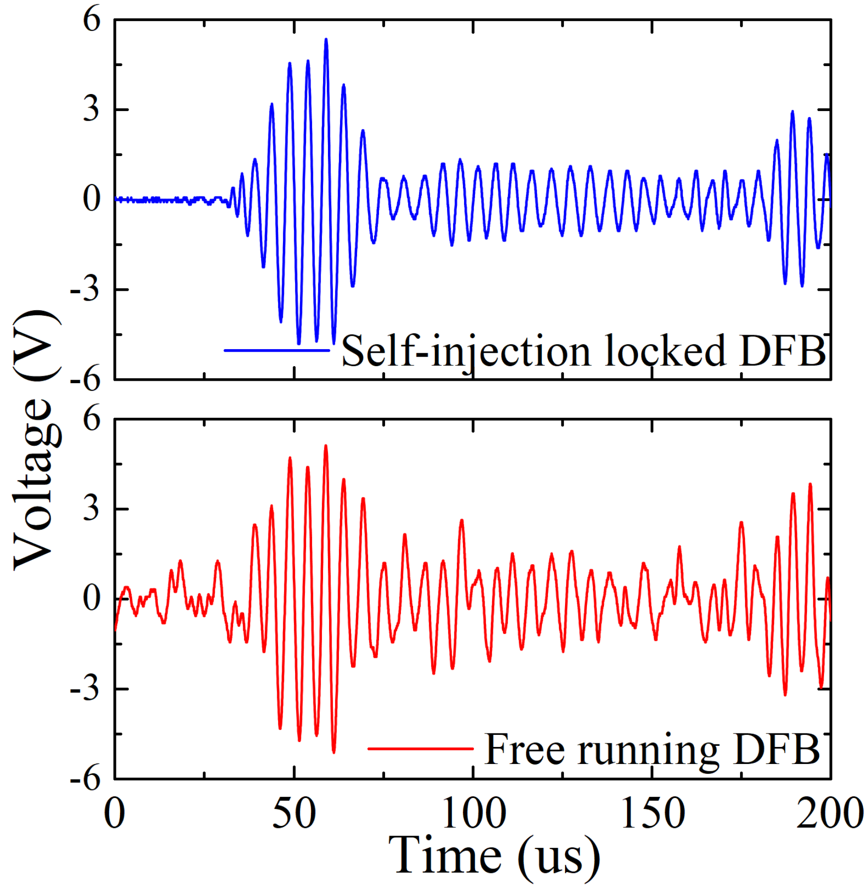

Figure 3.19: Temporal AE responses obtained from two different laser setting for the πFBG sensor.

The responses of the sensor system with the laser in self-injection locked mode and in free-running mode to the ultrasound generated by the piezo transducer on the plate are shown in Fig. 3.19 and 3.20, respectively. Both configurations show similar waveforms with similar peak-to-peak values (V_{pp} = 10.2 V), However, the self-injection locked system shows much smaller noises as evidenced by large fluctuations of the signal leading to the first ultrasonic pulse packet in Fig. 3.20 for both cases. To more accurately characterize the noise performance of the systems, we turned off the piezo-transducer and recorded the system outputs, as shown in Fig. 3.19 and 3.20 for these two configurations with a standard deviation (V_{sd}) of 8.6 mV, and 692.0 mV for the noise, respectively. It shows that the configuration with the self-injection locked DFB laser has much better signal-to-noise (SNR), which is over 35 dB larger than the configuration with the free running DFB laser. According to Eq. (3.2), the spectral slope at the normalized transmission of 0.76 is ~

0.5 pm^{-1}, V_{DC} is 1.05 V, the 10.2 V peak-to-peak voltage corresponds to a 62 nε peak-to-peak strain applied to the πFBG sensor. With the noise level of 8.6 mV and 450 kHz system bandwidth, the the configuration with the self-injection locked laser shows a strain sensitivity of ~78 fε/Hz$^{1/2}$. It is more than 60 times smaller than the sensitivity. For comparison, the thermodynamic limit of the phase noise for an 8 mm long regular optical fiber at 200 kHz is 4.0×10^{-10} rad/Hz$^{1/2}$, corresponding to a strain limit of ~ 12 fε/Hz$^{1/2}$.

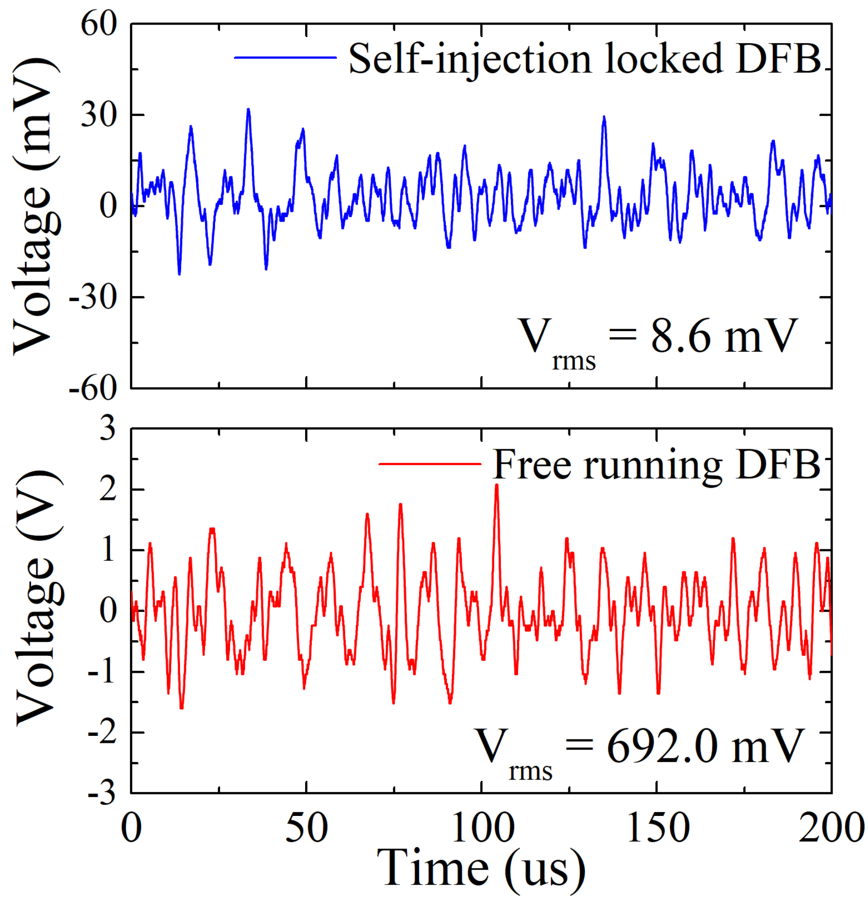

Figure 3.20: The noise output level without AE signal obtained from two different laser setting for the πFBG sensor.

The working point tunability of the self-injection locked laser system is shown in Fig. 3.21. The shadowed region in Fig. 3.21 is the tuning range of the locking point when controlling the fiber stretcher. To study the effect of the locking positions on ultrasonic detection, we tuned the lock point to three different positions (A, B, and C) on the πFBG spectrum and recorded the temporal responses of the sensor system. Fig. 3.22 shows the responses for locking positions A and C, where they were close to the boundaries of the locking range with maximum spectral slopes of πFBG. Their responses are waveforms with similar amplitudes (V_{pp} ~ 10 V) and a 180° phase difference, which is expected because spectral slopes at A and C have similar absolute values but opposite signs. Working point B was chosen to be close to the transmission peak of the πFBG with minimal spectral slope. The temporal responses to the ultrasound is shown in Fig. 3.22 and 3.23. Compared to operation at A and C, the response was much smaller with V_{pp} reduced from ~ 10 V to < 0.3 V. A double frequency component was observed in Fig. 3.23, as expected.

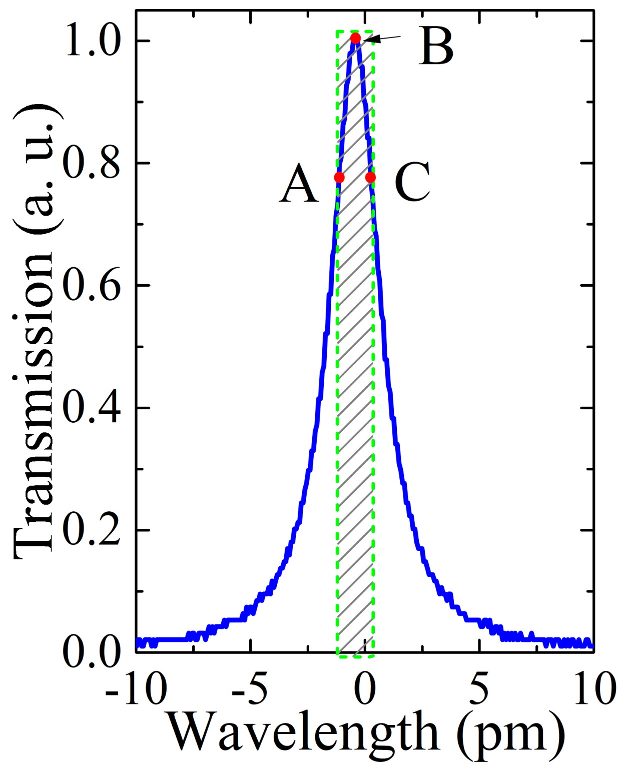

Figure 3.21: The locking rang of the self-injection locking laser and three working points set by adjusting the fiber stretcher.

The tolerance range to the free-running laser wavelength of the locked laser was also studied. The free-running laser wavelength was tuned by adjusting the current injected to the laser through the laser controller. At the beginning, the current was around 125 mA. During the current adjustment, the VOA was bypassed. It is found that the laser became unlocked when the current was less than 117 mA or larger than 133 mA with a locking range of 16 mA. Based on the wavelength tuning coefficient 10.9 pm/mA, a 16 mA current range corresponds to a wavelength range of ~ 174 pm for the free running laser. The laser could be re-locked by tuning the laser current into the range between 120 mA and 128 mA. These experimental demonstrations confirm that the self-injection locking system is resistant to the fluctuations of the laser injection current.

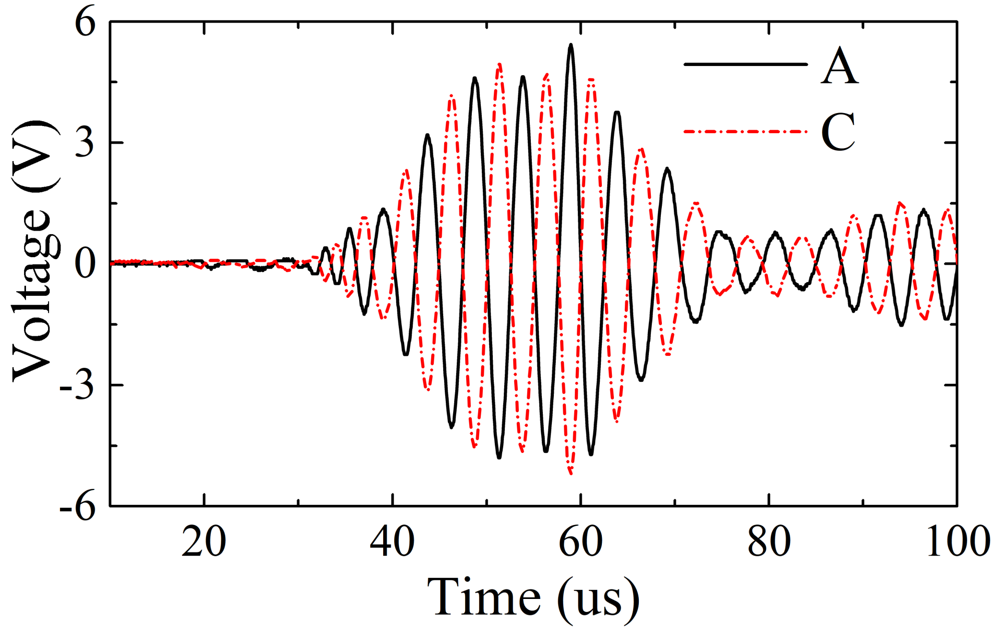

Figure 3.22: Ultrasonic responses at working points A and C.

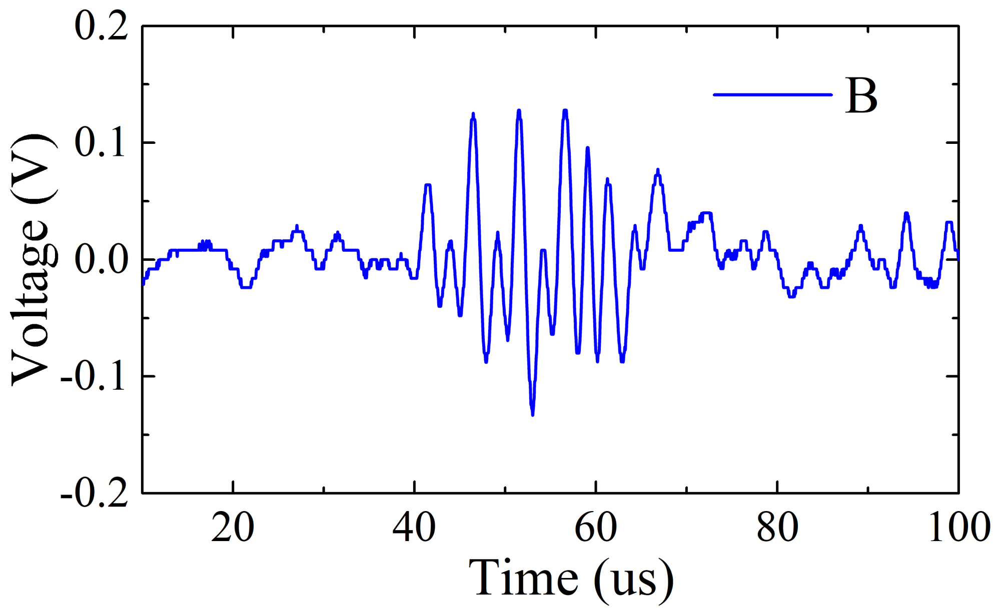

Figure 3.23: Ultrasonic responses at working points B.

It is seen that controlling the phase of the injected light (through the fiber stretcher shown in Fig. 3.15) is critical to optimize the detection sensitivity. Our experiment shows that, without adjusting the fiber stretcher, the laser wavelength under locked condition was always centered within the half of the linewidth of the πFBG central transmission peak., the wavelength of self-injection locked laser drifted randomly within the locking range, which is attributed to the random phase shift of the injected light from ambient perturbations. In addition mode hopping between different external cavity modes occurred from time to time during the drift With the fiber stretcher, the laser wavelength could be controlled to be locked at a position with a maximal slope, though mode hopping still could occur due to the dense external cavity modes. determined by the optical length of the feedback loop. However, the frequency of the signal caused by mode-hopping is much higher than the frequency of the ultrasound being detected (tens of MHz $vs.$ hundreds of kHz), the signal from the mode hopping can be easily filtered out without affecting the detected ultrasonic signal.

3.2.5 Conclusions

In conclusion, an ultrahigh sensitivity fiber-optic ultrasound sensor system with a πFBG sensor inside the optical feedback loop of a self-injection locked DFB diode laser was proposed and demonstrated. This intra-cavity πFBG functions as a locking element and an ultrasonic sensing element. Through a fiber stretcher to control the phase delay of the injected light, the wavelength of DFB laser source was locked to the slope of the narrow transmission peak of the πFBG. with significantly reduced laser frequency noise. The strain induced to the πFBG by ultrasound cause shifts of the πFBG transmission spectrum but has little effect on the wavelength of the locked laser. As a result, the ultrasound signal is converted to laser intensity variations after the πFBG. The experimental results show that the sensitivity of the proposed system based on the intra-cavity πFBG in a self-injection locked laser system Achieved a strain of 78 fε/Hz$^{1/2}$ at around 200 kHz, which is more than 35 dB higher than that of the same πFBG interrogated by the same laser in free running mode .The system is resistance to the fluctuations of free running laser wavelength.

3.3 Effect of Laser Polarization on Fiber Bragg Grating Fabry-Perot Interferometer for Ultrasound Detection

In this section, we are focusing on one key parameter in FBG sensors: Birefringence. During the fabrication of the FBG sensors, especially using UV laser beam side exposure technique with a phase mask to periodically modify the refractive index of the fiber core, extra birefringence is introduced by the asymmetrical refractive index distribution. Since the Bragg wavelength is highly related to the polarization, birefringence causes polarization dependent center-wavelength shift (PDCW). And the polarization depend loss (PDL) also increases.

3.3.1 Introduction

Ultrasonic sensors are commonly used for structural health monitoring [39], nondestructive testing [38], biomedical imaging [41], and range measurement [40]. Fiber-optic ultrasonic sensors, especially those based on fiber Bragg gratings (FBG), are extremely competitive to traditional piezoelectric sensors in terms of size, weight, immunity to electromagnetic interference, and multiplexing capability [34]. Ultrasonic impinging on the FBG senor induces strain to the fiber and shifts the reflection peak of the FBG. The sensor is usually demodulated by setting the wavelength of a laser to the slope of spectrum of an FBG sensor. Therefore, the wavelength shift is converted to intensity variations that can be measured by a photodetector (PD) [34]. In order to achieve high sensitivity, large spectral slope in the linear region of the spectrum of the sensor is required [55]. High reflective FBG-based optical resonators, such as π-phase-shifted FBG (πFBG) [55, 56], FBG Fabry-Perot interferometer (FPI) [57], or chirped FBG-FPI [17, 58], can provide narrow spectral features with width on the order of picometer to increase the sensitivity. A potential issue in practical applications that has been overlooked in the past is the fiber birefringence induced during FBG fabrication. Although regular single-mode optical fibers have little birefringence, laser illumination involved in FBG fabrication, either UV lasers or NIR ultrafast lasers, can induce birefringence to the fiber [59, 60]. Due to the fiber birefringence, the shape of the reflection spectrum of the sensor seen by the laser will be dependent on the state of polarization of the laser. As a result, the laser polarization can greatly affect the detection sensitivity of the sensor. Typically, the laser polarization is manually controlled to be linear and aligned to one of the principal axes using a polarization controller (PC) to achieve optimized ultrasound detection sensitivity [17]. This configuration is sufficient for relatively short fibers in laboratory environment, where the laser polarization can be stable over extended time. However, for practical applications where the fiber could be long and undergo various mechanical perturbation and ambient temperature changes, laser polarization may experience random and large changes [61], which can lead to reduced or even vanishing sensor sensitivity. Tackling this problem is difficult because of the lack of economically practical ways in both the detection and the automatic control of laser polarization.

In weak refractive index modulation FBG sensor, a small amount of the birefringence is expected to be negligible in low sensitive applications. On the other hand, high finesse feature is typical required for high sensitive fiber optic ultrasound sensor, that means strong refractive index modulation is required, multiple FBGs in series are necessary, which further intensify the birefringence with the conventional one-side UV laser beam exposure fabrication method. In order to use these types of sensors, polarization management is required in the ultrasound detection system. Typically, at least one polarization controller (PC) is placed before the sensor to align the polarization of the light source to one of the principal axes of the sensor to reach the maximum response to the ultrasound signal. For long-term operation, the laser drift and also ambient environment such as temperature, strain, bending could cause misalignment between the laser polarization and the principal axis of the sensor. Therefore, the response to the ultrasound signal will be degraded. Frequent polarization alignment is requires for long-term stability and limits the practical implementation of the sensors.

In order to decrease the polarization dependency to the laser, the birefringence of the sensor can be reduced by the 90-degree rotation method during the fabrication of the sensor. Hanawa *et al.* proposed the birefringence reduction technique for cascaded FBGs [62] and the experimental results of the polarization dependency is reported in [63]. The sensor consists a pair of FBGs cascaded to form an FPI structure. Both FBGs have very similar reflectivity, therefore the refractive index distribution introduced by each FBG is the same. In order to reduce the birefringence, the fiber is rotated 90 degrees before the fabrication of the second FBG. As expected, the overall index distributions for two orthogonal polarization states are the same for the FBG-FPI. Thus, the sensor is insensitive to the polarization state of the laser. This technique did not draw much of attention while the application scenario was limited. While in high finesse resonance spectral features for ultrasonic detection, the birefringence reduction is critical.

In this section, we developed a theoretical model to analyze the effect of laser polarization on the sensitivity of high-finesse FBG-PFI ultrasonic sensors with refringence. The results highlight the importance of minimizing the birefringence of such sensors for practical applications in ultrasonic detection. Experimentally, we fabricated an FBG-FPI sensor formed by two cascaded high-reflectivity FBGs that has reduced overall birefringence. By introducing a 90° rotation to the fiber between the fabrication of the two individual FBGs, the birefringence introduced during the FBG fabrication cancel out each other. The reflection spectral notch of the fabricated FBG-FPI has a narrow width of 2.0 pm and the overall birefringence of the sensor is reduced to a negligible level. This polarization-insensitive FBG-FPI sensor is characterized and tested for ultrasonic detection. For comparison, a regular FBG-FPI without birefringence control was also fabricated and tested. The experimental results show that the regular FBG-FPI exhibited large variations in the sensor response as the laser polarization was varied, while the polarization-insensitive FBG-FPI shows little degradation in the sensitivity with polarization. As a result, no control on the laser polarization is needed during the operation of the polarization-insensitive FBG-FPI for ultrasonic detection, which is a significant step towards the practical applications of such sensors.

3.3.2 Theoretical Analysis

We developed a theoretical model to analyze the effect of laser polarization and fiber refringence on the detection sensitivity of the ultrasonic sensor. We assume that the fiber-optic ultrasonic sensor is made from a high-finesse FPI, such as an FBG-FPI formed by two highly reflective FBGs. The transmission spectrum of a high-finesse FPI can be approximated by a Lorentzian function

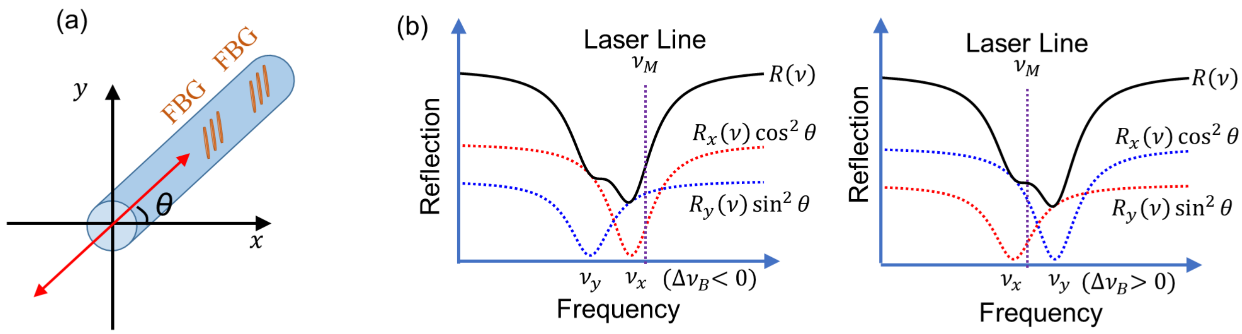

Figure 3.24: Schematics of (a) an FBG-FPI with x and y being the two principal axes of the sensor and the red arrow indicating the polarization of the probe laser, and (b) the reflection spectra measured by light polarized along its two principal axes as well as along an arbitrary direction for the cases of $\Delta\nu > 0$ and $\Delta\nu < 0$.

(narrow-peak approximation) [64]. As shown in Fig. 3.24(a) let x and y be the two principal axes of the birefringent FBG-FPI; then the normalized reflection spectra of the FPI probed by light polarized along $x-$ and $y-$axes, $R_{x,y}$, and their corresponding spectral slope, $S_{x,y}$, can, respectively, be expressed as

$$R_{x,y}(\nu_M) = 1 - \frac{(\Delta\nu/2)^2}{(\nu - \nu_{x,y})^2 + (\Delta\nu/2)^2}, \tag{3.3}$$

and

$$S_{x,y}(\nu) = \frac{\partial R_{x,y}}{\partial \nu} = \frac{2(\nu - \nu_{x,y})(\Delta\nu/2)^2}{[(\nu - \nu_{x,y})^2 + (\Delta\nu/2)^2]^2}, \tag{3.4}$$

where ν denotes optical frequency, ν_x and ν_y are the center frequencies of the corresponding spectral notches, and $\Delta\nu$ is the full-width-at-half-maximum (FWHM) of the notches. We further assume that the laser line for sensor demodulation is set at the maximum slope of the spectrum for one of the polarizations. This assumption is consistent with the common practice in which the laser polarization is adjusted using a PC to be aligned with one of the principal axes and the laser wavelength is set to a point on the spectral notch with maximum slope for optimized detection sensitivity. Without loss of generality, we assume the laser line is set on the rising edge with positive slope of the reflection spectrum corresponding to the $x-$polarization (R_x). The frequency at which R_x has the maximum slope, ν_M, can be found by solving $\partial^2 R_x/\partial \nu^2 = 0$ and the result is

$$\nu_M - \nu_N = \frac{\sqrt{3}}{6}\Delta\nu \approx 0.29\Delta\nu. \tag{3.5}$$

Substituting ν in Eq.3.4 with ν_M, we obtain the maximum slope as

$$S_{x,y}(\nu_M) = \frac{3\sqrt{3}}{6\Delta\nu} \approx \frac{1.30}{\Delta\nu}. \tag{3.6}$$

As discussed above, laser polarization can vary as it propagates along the fiber due to environmental perturbations. The overall reflection spectrum of the sensor is a superposition of the spectra measured by the $x-$ and $y-$components of the light and its exact shape is dependent on the exact state of polarization of the light arriving at the sensor. For simplicity, we consider the case where the polarization of the laser arriving at the sensor is simply rotated by an angle of θ from its original linear polarization along $x-$axis, as shown in Fig. 3.24(a). The overall reflection spectrum and the corresponding spectral slope seen by the laser is given, respectively, by

$$R(\nu) = R_x(\nu)\cos^2\theta + R_y(\nu)\sin^2\theta \tag{3.7}$$

and

$$S(\nu) = S_x(\nu)\cos^2\theta + S_y(\nu)\sin^2\theta. \tag{3.8}$$

The spectral slope for the polarization-rotated laser at the previously set frequency is evaluated by plugging $\nu = \nu_M$ into Eq.3.8, and, after some algebra, we obtain the normalized spectrum slope, defined by $s_n \triangleq S(\nu_M)/S_x(\nu_M)$, as

$$s_n = 1 - \sin^2\theta \left\{1 - \frac{16(1 - 2\sqrt{3}\Delta\nu_B/\Delta\nu)}{[(1 - 2\sqrt{3}\Delta\nu_B/\Delta\nu)^2 + 3]^2}\right\}, \tag{3.9}$$

where $\Delta\nu_B = \nu_y - \nu_x$ is the spectral separation of the FPI fringes caused by the birefringence of the FPI. Note that $\Delta\nu_B$ can take both positive and negative values, depending on whether x-axis is the slow axis or the fast axis of the sensor, as illustrated in Fig. 3.24(b). Also note that $-1 \leq s_n \leq 1$, where a negative s_n means that the spectral slope becomes negative under that particular polarization angle. Eq.3.9 is the main result of the theoretical model that can be used to analyze how the polarization angle (θ) and the spectral separation of fringes corresponding to the two polarizations relative to the spectral width ($\Delta\nu_B/\Delta\nu$) affect the detection sensitivity of the sensor.

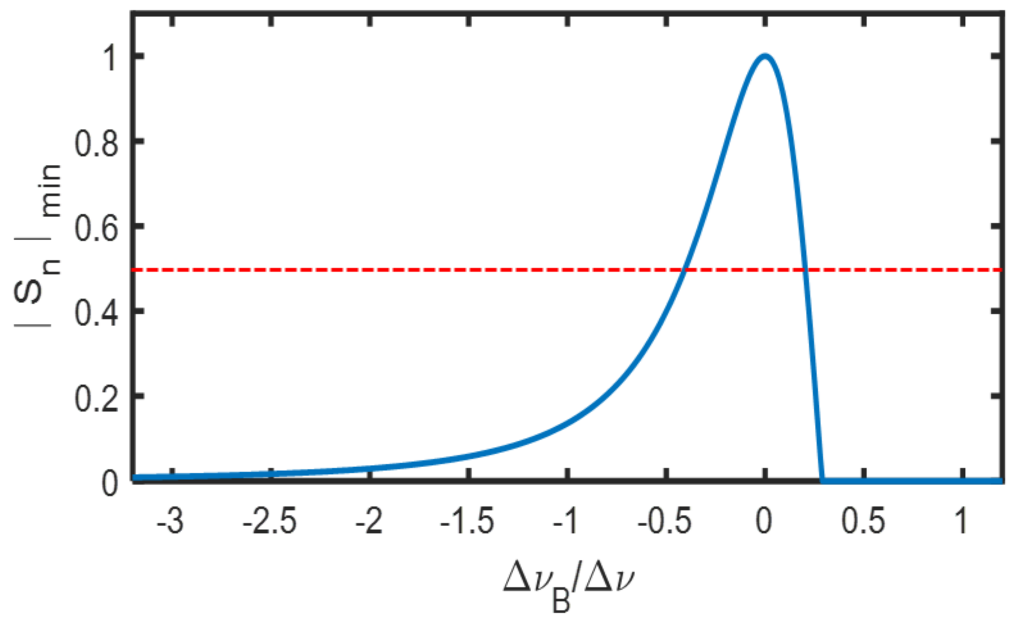

Figure 3.25: Minimum normalized sensitivity obtained by varying laser polarization angle vs. normalized sensor birefringence.

In practical applications, both positive and negative slopes can be used for sensor demodulation and the light polarization in the optical fiber may experience large changes over an extended time. Therefore, it is meaningful to vary the polarization angle (θ) and find the minimum of the absolute value of $s_n(|s_n|)$, which is used for characterizing the overall sensitivity of the sensor to laser polarization at different birefringence values ($\Delta\nu_B/\Delta\nu$). The result is shown in Fig. 3.25. When $\Delta\nu_B/\Delta\nu < 0$, which means that $\nu_y < \nu_x$, the minimum sensitivity gradually decreases and eventually vanishes as the sensor birefringence ($|\Delta\nu_B|$) increases. In this case, the minimum sensitivity occurs when the polarization is rotated by 90° from the x axis to the y axis. When $\Delta\nu_B/\Delta\nu \approx -0.41$, the minimum sensitivity is reduced to 0.5, representing a 6-dB reduction in sensor sensitivity. When $\Delta\nu_B/\Delta\nu > 0$, the minimum sensitivity decreases more rapidly as the sensor birefringence increases. The 6-dB sensitivity reduction occurs at $\Delta\nu_B/\Delta\nu \approx 0.20$, approximately half of the birefringence required for the same reduction for the case where $\Delta\nu_B/\Delta\nu < 0$. To maintain the sensitivity above half of its maximum, the spectral notch separation caused by sensor birefringence ($\Delta\nu_B$) should be less than ~ 61% of the spectral width of the notch. The minimum sensitivity reduces to 0 when $\Delta\nu_B/\Delta\nu \approx 0.29$. In this case, the notch valley for the $y-$polarization coincides with the laser wavelength ($\nu_y = \nu_M$), where the spectral slope vanishes for this specific polarization. The minimum sensitivity remains to be 0 as the sensor birefringence continues to increase beyond $\Delta\nu_B/\Delta\nu \approx 0.29$. Fig. 3.26 shows the sensitivity vs. polarization angle for several values of $\Delta\nu_B/\Delta\nu$. It is worth noting that for $\Delta\nu_B/\Delta\nu < 0.29$, the minimum sensitivity is non-zero and always occurs at $\theta = 90°$ or the laser polarization is rotated to the $y-$axis. For $\Delta\nu_B/\Delta\nu > 0.29$, the sensitivity is reduced to 0 at an angle that depends on the sensor birefringence and is less than 90°. For example, the sensitivity decreases to 0 at angle $\theta = 46°$ for $\Delta\nu_B/\Delta\nu = 0.5$; while it decreases to 0 at $\theta = 55.3°$ for $\Delta\nu_B/\Delta\nu = 1$. Then the sensitivity changes to negative values as the polarization angle continues to increase.

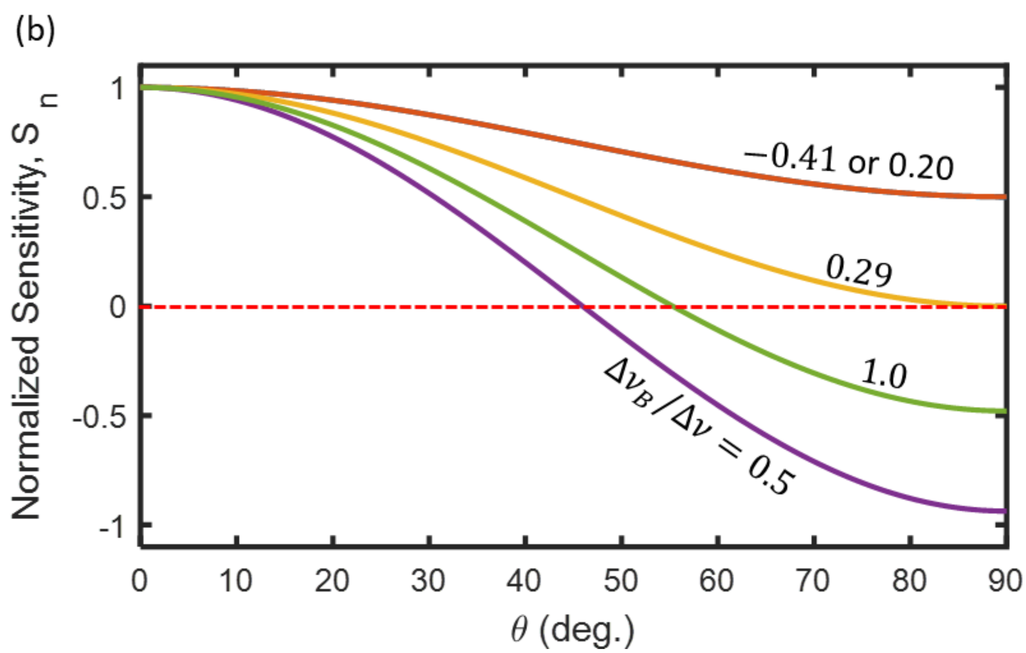

Figure 3.26: Normalized sensitivity vs. polarization angel for several sensor birefringence levels.

In order to response to a large frequency band of the ultrasonic signal, the total length of the sensor should keep as short as possible. In general, the length of the sensor should be less than half of the ultrasonic wavelength. If the sensor length is longer than the ultrasonic wavelength, the tensile strain and compressive strain caused by the ultrasonic signal would partially average out each other. Therefore, in our design, two FBGs should be short as well as the distance between them.

The depth of the FBG is designed as 16 dB, corresponding to a reflectivity of 97.5%. The full width at half-maximum (FWHM) of the FBG is about 0.35 nm. To ensure at least one interference peak locates within the FBG spectrum, the FSR should be smaller than half of the FWHM. The FSR is given by:

$$\Delta\lambda = \frac{\lambda^2}{2n_g L_c}, \tag{3.10}$$

where λ is the Bragg wavelength of the FBG, n_g is the group refractive index of the LP_{01} mode of the fiber. For conventional single mode optical fiber, group refractive index $n_g \approx n_{eff}$, where n_{eff} is the effective refractive index. The n_{eff} for our fiber is about 1.446. L_c is the effective length, which is a sum of the effective lengths of both the FBGs forming the cavity and the edge-to-edge distance between between the two FBGs: $L_c = L_s + L_{eff1} + L_{eff2}$. From Eq. (3.10), for a pair of 5-mm FBG with an FSR smaller than 0.17 nm, the effective length of the grating L_c should be larger than 4.89 mm.

The grating effective length L_{eff} at the Bragg wavelength is given by:

$$L_{eff} = L\frac{\sqrt{R}}{2\,\mathrm{arctanh}(\sqrt{R})}, \tag{3.11}$$

where R is the grating peak reflectivity. As shown in Fig. 3.27, with a low reflectivity value, the effective length of the grating L_{eff} is around half of the grating physical length L; while at high reflectivity value the effective length is close to zero. It can be physically comprehended by the fact that for a weak FBG, the reflected light along the grating is homogeneously distributed, while a high reflective FBG reflects most of the light from its initial part.

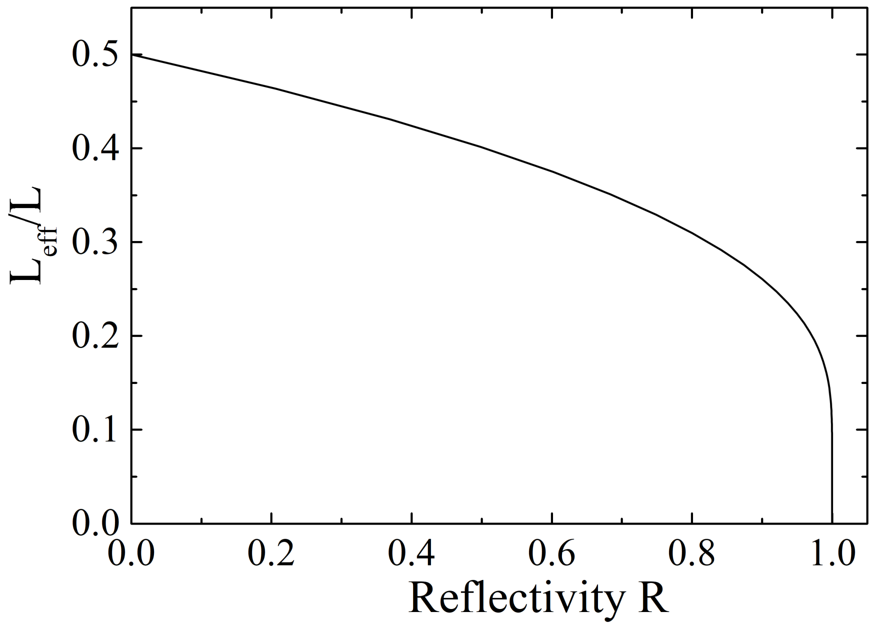

Figure 3.27: Relative effective length of a FBG versus its reflectivity R.

3.3.3 Structure and Fabrication of Polarization-Insensitive FBG-FPI Sensor

In our design, the relative effective length L_{eff}/L is about 0.195 for a single 5-mm FBG with 97.5% reflectivity. For a pair of FBGs with the same 97.5% reflectivity, $L_{eff1} = L_{eff2} = 0.975$ mm. Therefore, the edge-to-edge distance L_s should be larger than 2.94 mm.

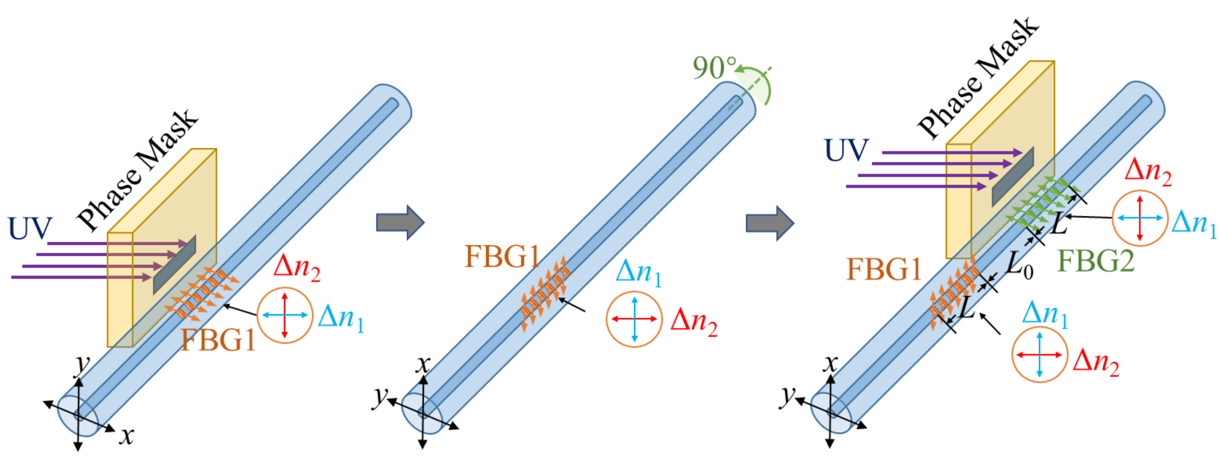

Figure 3.28: Fabrication of polarization-insensitive FBG-FPI sensor and its transmission spectrum.

We fabricated an FBG-FPI sensor on 125-μm single mode fiber that is insensitive to laser polarization using a phasemask and a UV laser. The fabrication procedure is schematically shown in Fig.3.28. The fiber was clamped between a pair of fiber rotators (Thorlabs, HFR007) through which the fiber could be rotated with a precise control of the rotation angle. First, one of FBGs that form the FPI was fabricated and a certain amount of fiber birefringence was induced to the fiber. Assume the index modifications along the $x-$ and $y-$directions are, respectively, $\Delta n_x = \Delta n_1$ and $\Delta n_y = \Delta n_2$, where $\Delta n_1 \neq \Delta n_2$ due to the induced fiber birefringence. Then the fiber was manually rotated by 90° to write the other FBG. Assuming the writing conditions were the same as for the previous FBG, the same amount of birefringence was induced. However, due to the 90° fiber rotation, the index modifications along the x and y directions for this FBG become, respectively, $\Delta n_x = \Delta n_2$ and $\Delta n_y = \Delta n_1$. Note that the wavelength position of the spectral notches of an FPI is determined by the optical length of the FPI. In this case, the optical lengths for $x-$ and $y-$polarization directions are the same, both being $(2n_0 + \Delta n_1 + \Delta n_2)L + n_0 L_0$, where n_0 is the unmodified effective refractive index of the fiber, L is the grating length, identical for both FBGs, and L_0 is the separation of the two FBGs. As a result, the spectral notches for $x-$ and $y-$polarization directions overlap and the sensor is insensitive to laser polarization variations. It is noted that a similar structure intended for application in fiber-optic communication systems has been reported [62, 63]. However, its application as polarization-insensitive ultrasonic sensors has not been demonstrated. During the fabrication process, transmission spectrum was monitored by an optical spectrum analyzer (OSA) with a white-light source to determine the reflectivity of the FBG. Reflectivity of each FBG was more than 97.5%. The pitch of the phasemask was 1071.5 nm, resulting a Bragg wavelength at around 1550 nm. The length of each of the FBGs was L=5 mm with a gap of $L_0 = 3mm$ between them, resulting in a total length of 13 mm for the FBG-FPI. The transmission spectrum of the FBG-FPI is shown in Fig. 3.29(a).

Due to the limited resolution of the OSA (20 pm), the interference peaks within the FPB-FPI spectrum were measured by a wavelength-scanning laser along with a photodetector (PD) as schematically shown in Fig. 3.30. Note that the same setup was also used for testing of the sensor for ultrasound detection, as described later. With a 3-paddle manual fiber PC, the laser polarization could be tuned randomly, which also allowed us to study the sensitivity of the FBG-FPI to laser

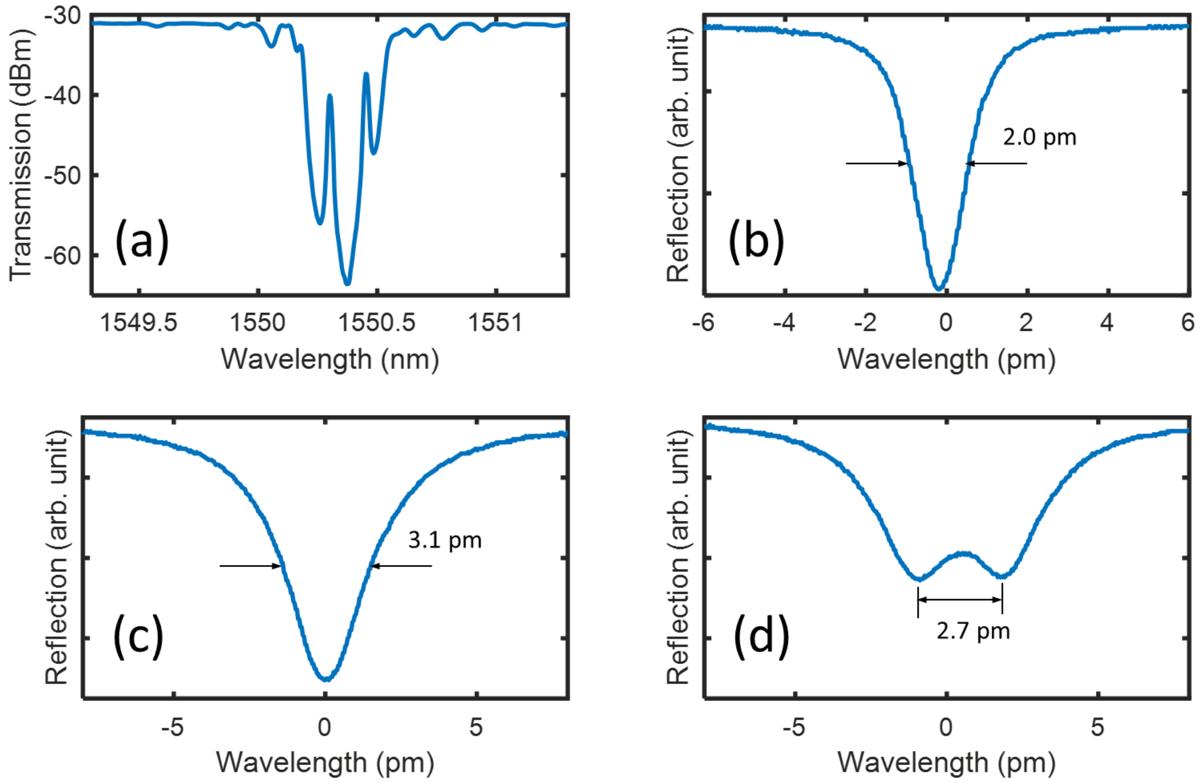

Figure 3.29: (a) measured by an OSA and the reflection spectrum (b) measured by a wavelength-scanning laser. (c) and (d) are the reflection spectra of a regular FBG-FPI fabricated without fiber rotation measured by the wavelength-scanning laser at two different polarization states.

polarization. The detailed reflective spectral profile of the reflection notch used for ultrasound detection is shown in Fig. 3.29(b), which reveals that the notch has a FWHM of $\Delta v = 2.0 pm$. Then the polarization of the laser was changed by rotating the three paddles of the PC and the reflection spectrum was monitored. No visible change in the shape of the notch or the splitting of notch was observed, indicating a negligible overall birefringence of the FBG-FPI sensor with respect to the spectral width ($\Delta v_B/\Delta v \approx 0$).

For comparison, a regular FBG-PFI sensor was fabricated without fiber rotating and characterized with the same experimental setup and process as described above. The UV illumination during the FBG fabrication induced significant birefringence to the fiber and the reflection spectrum of the FBG-FPI shows a large dependence on the polarization state of the probing laser. Figure 3.29(c) is the reflection spectrum recorded when a single narrow notch was obtained by tuning the laser polarization. In this case, it is expected that the laser polarization was aligned with one of the principal axes of the regular FBG-FPI. The notch has a FWHM of $\Delta\nu = 3.1pm$. This increased spectral width compared with the polarization-insensitive FBG-FPI is believed to arise from the differences in the alignment of focused UV beam and the fiber core that resulted in a slight difference in the grating strength. Figure 3.29(d) is another case where the spectrum split into two valleys with the same depth. In this case, the laser was polarized in such way that the laser power was equally distributed between the two principal axes of the FBG-FPI and the spectrum was a superimposition of the two spectra probed by the laser components at the two principal polarization directions. The two valleys were separated by 2.7 pm. Note that this separation of the two valleys cannot be simply treated as the separation of the notches corresponding to the two individual polarizations ($\Delta\nu_B$). Using the model for the spectrum described by Eq. 3.3, the 2.7 pm valley separation correspond to a relative birefringence of $|\Delta\nu_B/\Delta\nu| \approx 0.97$ with $\Delta\nu_B = 3.0pm$. As shown in Fig. 3.25, such level of birefringence would make the FBG-FPI highly sensitive to laser polarization with relative sensitivity that can be reduced to 0 for the case of $\Delta\nu_B/\Delta\nu > 0$ and to the minimum value of 0.15 for the case of $\Delta\nu_B/\Delta\nu < 0$ at certain polarization angles.

3.3.4 Sensor Testing for Ultrasonic Detection

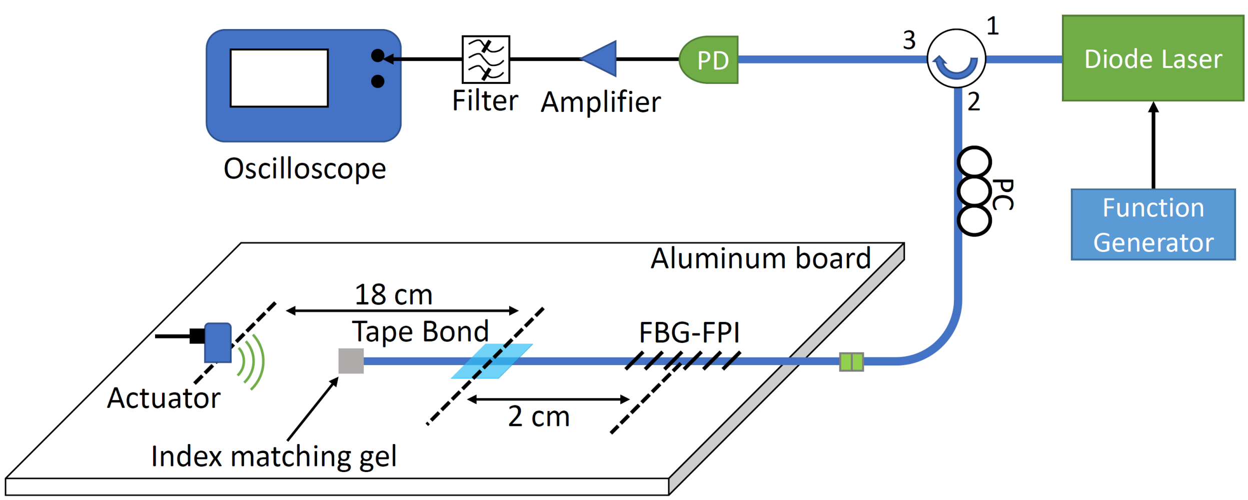

Figure 3.30: Experimental setup for sensor polarization dependency measurement and ultrasound detection. PC: polarization controller, PD: photodetector.

The experimental setup used for studying the dependence on laser polarization of the sensor for ultrasound detection is shown in Fig. 3.30. The light from a wavelength-tunable narrow linewidth diode laser was directed to the FBG-FPI sensor through a circulator. After the circulator, the light first passed through a 3-paddle PC before reaching the sensor. The PC allowed us to manually change the laser polarization. The end of the fiber with the sensor was covered with index matching gel to eliminate the light reflection from the fiber end. The light reflected from the sensor, after passing through the PC, was routed to a PD through the same circulator. The signal from the PD was then amplified and filtered by a 50-500 kHz bandpass filter for ultrasonic signal analysis. A piezoelectric actuator glued to the plate was used to generate ultrasonic pulses for testing. It was driven by a four-cycle 5 V peak-to-peak sinusoidal burst wave centered at 200 kHz generated by a function generator. The sensor fiber was bonded with Scotch tape to an aluminum plate at a position close to but away from the sensor position. Through this remote-bonding configuration [65, 66], the ultrasonic wave traveling on the plate was first coupled to the fiber in the bonding region, then traveled along the fiber to the sensor for detection. This so-called "remote-bonding" configuration can effectively prevent the potentially large quasi-static strain of the plate from being applied to the sensor. The center to the center separation between the bonding region and the FBG-FPI was 2 cm. The distance between the piezoelectric actuator and the bonding center was 18 cm. Other than the bonding area, other parts of the fiber were isolated from the aluminum board to avoid undesirable ultrasound coupling.

First, the polarization-insensitive FBG-FPI sensor was tested. To determine the operating point, the reflection spectrum was monitored by scanning the laser wavelength as the laser polarization was changed by randomly rotating the three paddles of the PC. As described above, the shape of the spectral notch did not show observable changes. Then the laser was changed to single-frequency operation and ultrasonic pulses were generated by the piezo transducer. The laser wavelength was tuned to a position that yielded maximum response to the ultrasonic pulses observed on the oscilloscope. Once the laser operating point was set, the sensitivity to laser polarization was tested by monitoring the sensor response to the ultrasonic pulses as the laser polarization was again changed randomly using the PC. A video displaying the sensor response as the laser polarization was randomly changed. It is seen that the sensor response showed only slight changes. The black and red curves in Fig. 3.31 are, respectively, the responses with maximum and minimum responses as the polarization was changed. Both of them have similar peak-to-peak amplitude of $\sim 2.2V$. The slight difference between them is attributed to the changes in the attenuation of the PC as the paddles of the PC were rotated.

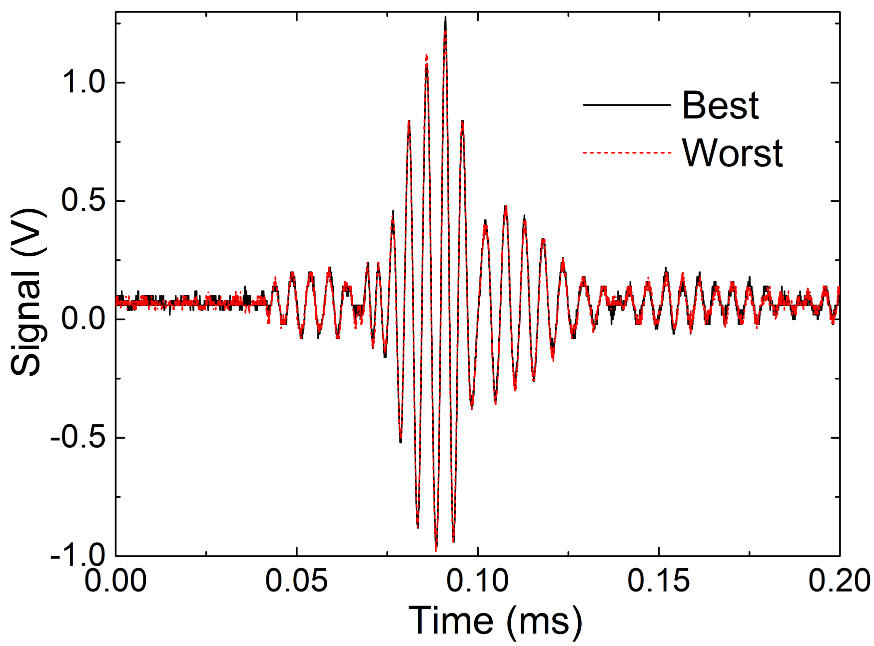

Figure 3.31: Ultrasonic responses of the polarization-insensitive FBG-FPI sensor.

Next, the regular FBG-FPI sensor with the two FBGs fabricated without rotating the fiber was tested. Again, the reflection spectrum of the sensor was monitored as laser polarization was changed until the spectral notch reached its narrowest width, which indicates that the laser polarization was aligned with one of the principal axes of the sensor. Then, following the similar process used for polarization-insensitive sensor, the laser wavelength was tuned to the point with maximum response, as shown by the black curve in Fig. 3.32 with a peak-to-peak output of $\sim 1.2V$. Note that, compared with the polarization-insensitive FBG-FPI, the reduction of the maximum response of the regular FBG-FPI (1.2 V vs. 2.2 V) is consistent with its smaller maximum spectral slope due to its wider spectral notch (3.1 pm vs. 2.0 pm). The sensor response to the ultrasonic pulses was monitored as the laser polarization was randomly changed. Clearly, the sensor response shows large variations with polarization. It is also seen that around certain polarization states, the sensor response vanished completely and then increased but with a 180° phase change. The red curve in Fig. 3.32 is the response of the sensor when the laser was tuned to an arbitrary polarization state. The peak-to-peak voltage was 0.05 V, a 30 dB reduction from its maximum response.

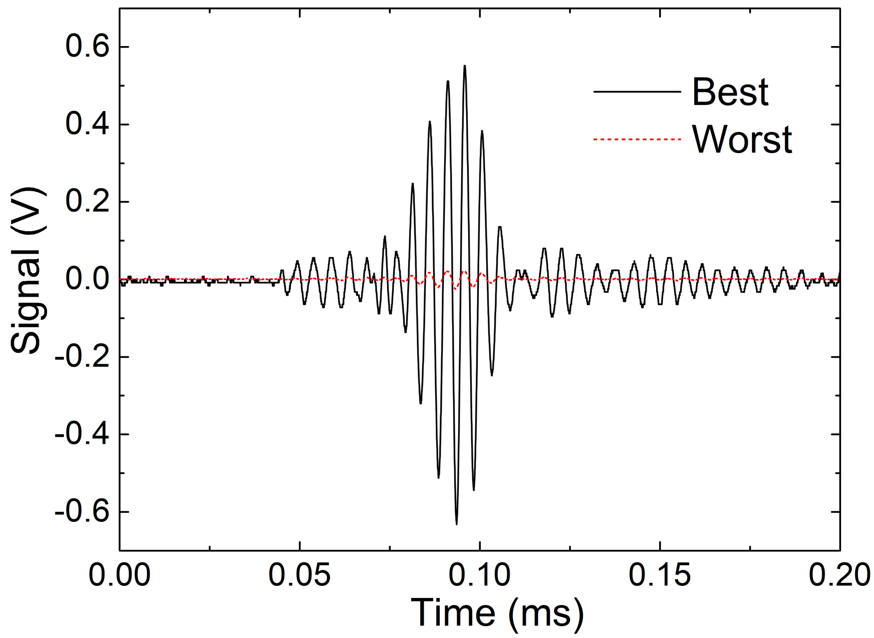

Figure 3.32: Ultrasonic responses of the conventional one-side exposed FBG-FPI sensor.

3.3.5 Conclusions

In conclusion, we have developed a model to analyze the effect of laser polarization on the sensitivity of high-finesse FBG-FPI sensors for ultrasonic detection. The analysis shows that, to maintain the sensitivity above half of its maximum, the spectral notch separation caused by the sensor birefringence should be less than $\sim 61\%$ of the full-width-at-half-maximum of the notch of the FBG-FPI, highlighting the importance in controlling the birefringence of the sensor in practical applications. We have fabricated an FBG-FPI with reduced overall birefringence by a 90° rotation of the fiber between the fabrication of the two FBGs. Due to this 90° rotation, the birefringence induced during the fabrication of the two FBGs cancels out each other. The fabricated FBG-FPI shows a narrow notch width of 2.0 pm and negligible birefringence. For comparison, a regular FBG-FPI was also fabricated without fiber rotation, which exhibits a notch width of 3.1 pm that split into two peaks with a 2.7 pm separation at certain polarization states of the probe laser. Both sensors were tested for ultrasonic detection. The experimental results show that the regular FBG-FPI exhibited large variations in the sensor response as the laser polarization was varied, while the polarization-insensitive FBG-FPI shows little degradation in the sensitivity with polarization. As a result, no control on the laser polarization is needed during the operation of the polarization-insensitive FBG-FPI, representing a significant step towards the practical applications of such sensors.

3.4 Summary

This chapter presents the study of various ultrasonic wave detection system based on FBG-based resonators. We investigated a high-sensitivity fiber-optic ultrasonic sensor system using a self-injection-locked distributed feedback (DFB) diode laser where a π-phase-shifted fiber Bragg grating (πFBG) serves as both the locking resonator and the sensing element in a fiber ring feedback loop. FBG-FPIs have shown great promise as sensitive ultrasonic sensors. However, the fabrication process of the sensors usually introduces birefringence to the fiber, which makes the sensor operation sensitive to the polarization of the probe laser. Here, we theoretically study the effect of laser polarization on the sensitivity of the sensor with birefringence. Then we studied the polarization insensitive FBG-FP sensor with 90° rotation fabrication method to realize stable ultrasonic response to arbitrary polarization state of the laser source. As a result, the birefringence introduced during the fabrication of the two FBGs cancels out each other. No control on the laser polarization is needed during the operation of the polarization-insensitive FBG-FPI for ultrasonic detection, an important attribute required in many practical applications of the sensor. At last, an AE detection system based on a CFBG pair has been described. By introducing cracks on the aluminum plate, real AE signals are examined, which are also compared with those from pencil break tests. Our experimental results suggest that the crack-induced AE spans over a broad ultrasonic frequency range, with a peak intensity ranging from 100 kHz to 350 kHz.

CHAPTER 4

ACOUSTIC EMISSION SENSORS BASED ON LOW-FINESSE FIBER-COIL FPI

Part of the material in this chapter has been published in

- *“Passive quadrature demodulation of birefringent low-finesse fiber-optic Fabry–Perot interferometric sensors," Optics Letters, vol. 45, no. 13, pp. 3419, 2020*
- *"Polarization-insensitive, omnidirectional fiber-optic ultrasonic sensor with quadrature demodulation," Optics Letters, vol. 45, no. 15, pp. 4164, 2020*

4.1 Passive quadrature demodulation of coiled polarization maintaining fiber Fabry-Perot interferometer for ultrasonic sensing

In this section, we propose and demonstrate a fiber-optic ultrasonic sensor using coiled polarization maintaining (PM) fiber with low-finesse Fabry-Perot interferometer formed by two chirped fiber Bragg gratings (CFBG). By controlling the bending radius, the bending length, and the twist of the coil structure, extra birefringence is introduced between the gratings and resulting a total phase delay close to 90° between the fast and slow polarizations of the PM fiber. Then the laser signal pass through a polarization beam splitter and measured by two photodetectors. Combining the coil structure, wide spectral range, and quadrature demodulation, a strain and temperature insensitive fiber-optic ultrasonic detection is realized. The ultrasonic sensing scheme is immune to the laser wavelength drift, therefore no wavelength locking mechanism is needed.

4.1.1 Introduction

Ultrasound detection using fiber optic resonators has been widely investigated as a substitute to piezoelectric transducers. As mentioned before, compare to piezoelectric transducer, fiber-optic sensor is commonly immune to electromagnetic interference, light weight, and resistance to corrosion. In order to achieve high response to the disturbance to the fiber Bragg grating type of sensor, edge filter detection method is usually used to demodulate the ultrasonic signal. Specifically, probing laser wavelength is locking to the slope of the spectrum of the sensor. For ultrasonic signal detection application, the dynamic strain caused spectrum shift translates to laser intensity change. Theatrically, the variations of the detected laser intensity are proportional to the magnitude of the ultrasonic signal. The sensitivity is proportional to the slope of the spectrum of the resonator. To maximize sensitivity, high Q-factors are required for fiber optic resonators. Contradictory, high Q-factor lead to small linear range which limits the detectable signal strength and vulnerable to external disturbances. In practice, laser wavelength should be locked to the sensitive region of the resonator spectrum.

Fiber-optic Fabry-Perot (FP) interferometric sensors [67] possess several favorable characteristics including high sensitivity, simple structure, easy fabrication, and capability to withstand harsh environment. They are becoming attractive options for measurement of a variety of physical parameters such as pressure, temperature, strain, and acoustic and ultrasonic waves. Sensor demodulation has been a long-recognized challenge in the practical applications of these sensors for measuring small and highly dynamic signals such as acoustic and ultrasonic waves. Laser-based demodulation where the wavelength of the laser is set on the spectral slope of the sensors fringes to convert the measurand-induced phase changes into laser intensity variations is typically used to achieve the required detection sensitivity and speed. However, the operating point can change from the optimal positions due to the laser wavelength drift and/or spectral shift of the sensor from environmental perturbations, leading to signal fading at the fringe valleys or peaks where the sensitivity vanishes. A straightforward solution is to lock the laser wavelength to the linear range of the sensor spectrum [68, 17]. However, the stringent requirement on the tuning range and tuning speed of the laser and the complex electronic system for locking makes it impractical in many applications. For low-finesse FP sensors whose spectrum features sinusoidal fringes, quadrature demodulation provides an elegant solution to the issue of signal fading. The essence of quadrature demodulation is to generate a pair of signals or fringes whose phases are quadrature shifted. Environmental perturbations shift the both fringes simultaneously by the same amount so that the quadrature phase shift is maintained, and sensitive detection is possible for at least one of them regardless the relative position of the laser wavelength on the spectral fringes of the sensor. In particular, phase-generated carrier demodulation [69] is a well-known active quadrature demodulation technique where the quadrature signals are generated by actively modulating the laser frequency or the sensor itself. A drawback of the method is the requirement of a wavelength-tunable laser or a sensor whose cavity length can be modulated in operation with high speed.

Passive quadrature demodulation methods that does not require tuning the laser source or the sensor, which significantly simplifies the wavelength locking system, especially minimizes complex electronic locking system. Many passive quadrature demodulation methods have been proposed and demonstrated. One of them is to use a pair of FP cavities with quadrature phase shifted fringes that work in tandem [70]. However, producing such pair of FP cavities requires precise control over the cavity lengths, which is a non-trivial task. Another method is to use multiple lasers whose wavelengths are in quadrature positions of the sensor fringes [71, 72, 73]. The use of multiple lasers may significantly increase the system complexity and cost. In addition, for sensors with dense spectral fringes, the laser wavelengths are close, causing difficulty in maintaining the quadrature phase shift due to the laser wavelength drift as well as difficulty in separating the two laser signals. Recently, we demonstrated another passive quadrature demodulation method in which the two wavelengths at the quadrature points are generated by a laser and a frequency shifter [52]. However, the method is only applicable to sensors with long FP cavities because of the limited frequency shift that can be generated by the frequency shifter.

Therefore, we propose and demonstrate a different passive quadrature demodulation method where quadrature phase-shifted fringes are generated by light of the two orthogonal polarizations in the fiber and the FP cavity. The method is enable by a new fiber-optic FP sensor design that has a birefringent FP cavity with precisely controllable birefringence.

4.1.2 Sensor design and theoretical analysis

4.1.2.1 FP cavity with linear birefringence

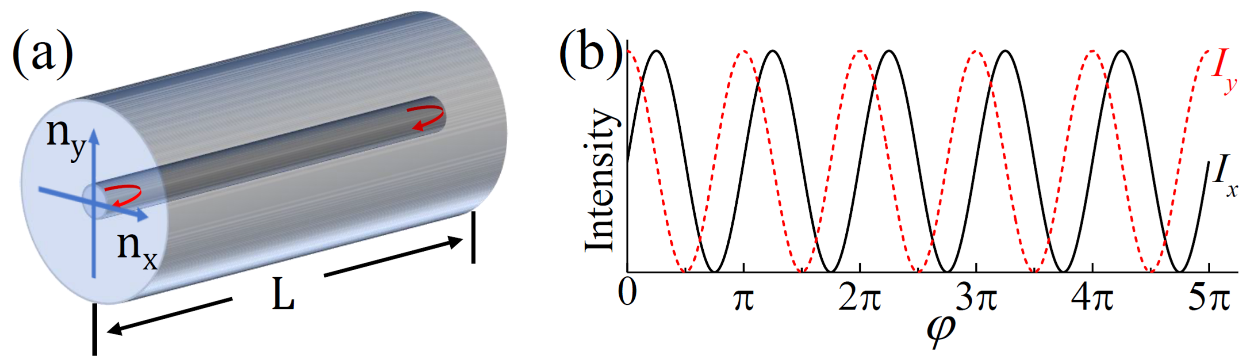

Figure 4.1: Schematics of (a) a sensor with a birefringent FP cavity and (b) spectral fringes with quadrature phase shift probed by light linearly polarized along two principal axes of the cavity.

The principal of operation can be more clearly illustrated using Fig. 4.1 as an example, which depicts an FP cavity formed by a short section of fiber with linear birefringence. Assuming the refractive indices of the fiber corresponding to the two principal axes of the FP cavity are n_x and n_y, the spectral fringes probed by the light at these two polarizations are given by

$$\begin{aligned} I_x &= A[1 + b\cos(4\pi n_x L/\lambda + \theta)] \\ I_y &= B[1 + b\cos(4\pi n_y L/\lambda + \theta)], \end{aligned} \tag{4.1}$$

where λ is the wavelength of operation, L is the physical length of the FP cavity, A and B are two constants determined by the optical power of the light at two polarizations, and b and θ denote, respectively, the fringe visibility and the initial phase of the fringes. For simplicity, b and θ are assumed to be identical for both polarizations. The phase shift between the two fringes are given by

$$\Delta\theta = 4\pi\Delta n L/\lambda, \tag{4.2}$$

where $\Delta n = n_x - n_y$ is the cavity birefringence. From Eq. (4.2), around a small range of a given operating wavelength, a quadrature phase shift between the two fringes, as shown in Fig. 4.1(b), can be obtained by controlling the cavity birefringence (Δn) and/or the cavity length (L). Specifically, letting

$$\Delta\theta = (m + 1/2)\pi \ (m = 0, 1, 2, ...), \tag{4.3}$$

gives

$$\Delta nL = (m/2 + 1/8)\lambda. \tag{4.4}$$

If the two polarizations are both excited and separately detected, at least one of the polarizations will give a signal that is sensitive to the measurand-induced spectral shift of the FP sensor.

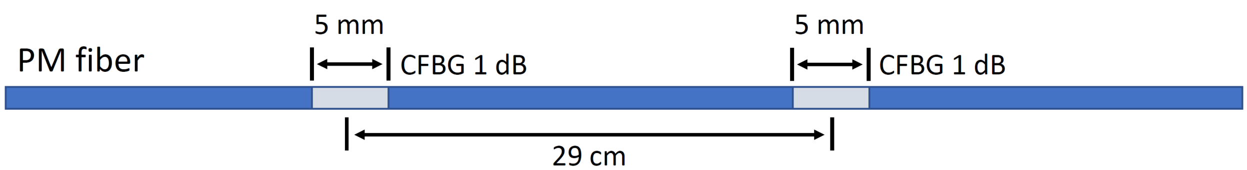

Figure 4.2: The CFBG-FP sensor structure.

The structure of the sensor is show in Fig. 4.2. The sensor contains a pair of chirped fiber Bragg gratings (CFBG) with the same chirping rate and direction. The CFBGs are weakly written on the polarization maintaining (PM) fiber. Two CFBGs function as two mirrors and form a low-finesse Fabry-Perot interferometer (FPI), as schematically shown in Fig. 4.3. In order to generate sharp spectral slope, the fringes should be dense. Therefore, the separation between the two CFBGs should be large enough. To achieve responsive to ultrasonic signal whose wavelength is much shorter than the fiber length between the two CFBGs. The fiber between the CFBG-FPI is coiled in one layer tight loops. The diameter of the outer loop is shorter than the ultrasound wavelength. Then the coiled loops is glued to the aluminum plate for ultrasound detection.

4.1.2.2 Quadrature demodulation

The key idea for quadrature demodulation is that a 90-degree phase difference between the two channels. In our design, the quadrature phase difference is formed by controlling the birefringence in the PM fiber. Specifically, the birefringence in the PM fiber contains three components:

1. Original birefringence of the PM fiber itself;

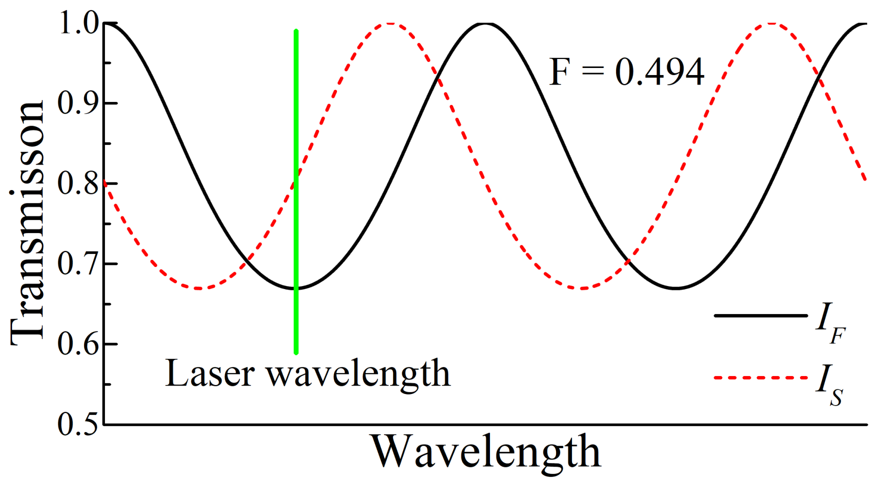

Figure 4.3: Simulated CFBG-FPI transmission spectrum with low-finesse FPI features sinusoidal fringes.

2. CFBG introduced birefringence;

3. Bending introduced birefringence.

The first two components are fixed and hard to tune since the CFBG fabricated onto a specific type of PM fiber. However, the birefringence introduced by the bending can be tuned by controlling the coil diameter and the twist status. Therefore, a quadrature phase difference is achievable between the fast and slow axes of the PM fiber.

In order to form sinusoidal fringes with a CFBG-FPI structure, the reflectance of the CFBG should be small. The free spectral range (FSR) is defined as the wavelength separation between adjacent transmission peaks $\Delta\lambda$ and given by:

$$\Delta\lambda = \frac{\lambda_0^2}{2n_g l}, \tag{4.5}$$

where λ_0 is the wavelength within the bandwidth of the CFBG, n_g is the group refractive index, l is the separation between the two CFBGs.

If both CFBG have a reflectance R, the transmittance function of the CFBG-FPI is given by:

$$T = \frac{(1-R)^2}{1 + F\sin^2(\varphi/2)}, \tag{4.6}$$

where

$$F = \frac{4R}{(1-R)^2} \tag{4.7}$$

is the coefficient of finesse. The finesse is defined as the FSR divided by the bandwidth (full-width half-maximum) of the transmission peak:

$$F = \frac{\Delta\lambda}{\delta\lambda} \tag{4.8}$$

where $\delta\lambda$ is the full-width half-maximum (FWHM) of the transmission peak.

The finesse is only determined by the reflectance of the resonator and is independent of the cavity length.

Since the shape of the spectrum is not perfect sinusoidal, a 90° phase delay between the fast and slow polarizations is not optimal for quadrature demodulation. As shown in Fig. 4.6, when the laser wavelength locates at the spectrum valley of the fast polarization, the magnitude of the slope of the slow polarization is not reaching the maximum. Besides, the minimum response to the ultrasonic signal is determined by the minimum magnitude of the intersection points of the slope curves between the fast and slow polarizations. In order to achieve maximum and full-time response to the ultrasonic signal, the magnitude of the intersection points should as large as possible. Therefore, the phase delay between the fast and slow polarizations should larger than 90°. Based on the analysis above, simulation results (Fig. 4.7) show that a 104° phase delay provides the optimal response to the ultrasonic signal. The minimum magnitude of the slope is about 0.1 rad^{-1} for an FP sensor with 10% reflectance of each CFBG.

4.1.3 Experimental demonstration

4.1.3.1 System setup

We demonstrated the polarimetric quadrature demodulation method for ultrasonic detection on a metal plate using an experimental setup shown schematically in Fig. 4.4. The sensor structure, depicted in Fig. 4.5, is a low-finesse FP interferometer formed by two chirped fiber Bragg gratings

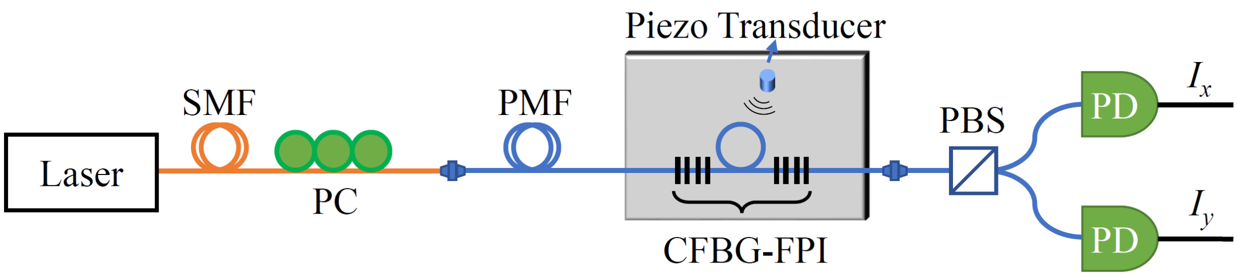

Figure 4.4: Schematics of the sensor system with polarimetric passive quadrature demodulation for ultrasonic detection.

(CFBGs) at the ends of a coiled polarization maintaining (PM) fiber. The purpose of the PM fiber is to maintain the polarization states of the light in the FP cavity. The CFBGs provide optical reflections over a relatively wide bandwidth that has the potential to accommodate a large spectral shift of the fringes from environmental perturbations. There are several benefits of using the fiber-coil FP cavity as the sensing element for ultrasonic detection. Compared with ultrasonic sensors with straight fibers whose response is dependent on the direction of the ultrasonic signal, a fiber coil sensor [74] is omnidirectional due to its circularly symmetric structure.

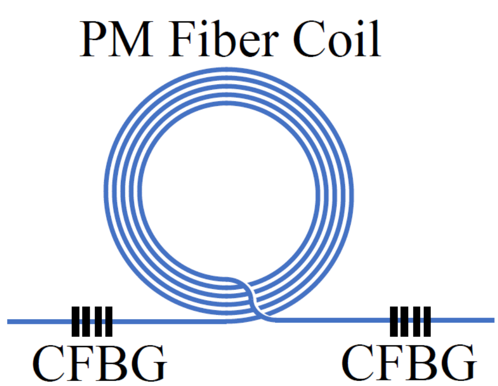

Figure 4.5: The PM fiber-coil FP sensor.

A fiber coil with multiple loops can incorporate a long span of fiber into a small sensor footprint. A long fiber length results in dense spectral fringes with large spectral slopes for sensitive detection of spectral shift; while a small sensor size can minimize the phase cancellation effect, which is important for detecting of high-frequency ultrasound. The fiber coil also provides a convenient way to precisely adjust the total birefringence of the FP cavity even after the CFBGs are fabricated and the fiber length of the FP is determined. By controlling the bending radius and the length of the coiled fiber and twisting the fiber, extra birefringence and phase shift can be introduced to the fiber in the FP cavity to achieve a total phase difference close to 90° of the two fringes corresponding to the two polarizations. Specifically, bending-induced birefringence of a fiber is determined by the bending curvature radius (R) and the fiber diameter ($2r$) and is given by [75]

$$\Delta n_B = 0.25n^3(p_{11} - p_{12})(1 + v)r^2/R^2, \tag{4.9}$$

where p_{11} and p_{12} are the elasto-optic coefficients, and v is the Possion's ratio of the fiber.

For a regular silica fiber with a diameter of $2r = 125\ \mu m$, $n = 1.45$, $p_{11} - p_{12} = 0.15$, $v = 0.17$, the bending-induced birefringence of a fiber coil with a diameter of $2R = 1.2$ cm, which is the diameter of the fiber coil used in the experiment, is $\Delta n_B = 1.8 \times 10^{-5}$. In the worst scenario, a maximum phase shift of $\pi/2$ needs to be provided by fiber bending to achieve a quadrature phase shift between the fringes of the two polarizations. Letting $m = 0$ in Eq. (4.4), we obtain the length of the coiled fiber corresponding to this $\pi/2$ phase shift, which is $\Delta L = \lambda/8\Delta n_B = 1.1$ cm at wavelength $\lambda = 1550$ nm.

Then, regardless of the initial phase difference of the two fringes, if necessary, we only need to straighten a short a span (at most 1.1 cm) of fiber from the fiber coil to achieve a quadrature shift between the fringes. Note that if the principal axes of the bending-induced birefringence do no align with those of the inherent birefringence of the fiber, the bending may cause a rotation of the principal axes of the overall birefringence of the fiber coil with respect to the uncoiled PM fiber. Because the bending-induced birefringence is much smaller than that of the PM fiber ($\Delta n = 3 \times 10^{-4}$ for a PM fiber with a beat length of 5 mm at 1550 nm), the rotation, if exists, is expected to be small and slightly twisting the PM fiber may align the principal axes of the fiber coil with the straight PM fiber [76].

Due to the birefringence introduced by CFBG fabrication, the coil and twist of the PM fiber, a total phase delay of 90° between the fast and slow polarizations of the PM fiber is generated within the sensor spectrum and the simulated transmission spectra are shown in Fig. 4.6. The magnitude slopes of the fast and slow polarization spectra are shown at the bottom of Fig. 4.7.

For ultrasonic sensing with edge filter detection method, the signal strength is proportional to the slope in the linear region of the spectrum of an FBG-based optical resonator. As a result, the ultrasound-induced spectral shift of the CFBG-FPI is converted to laser intensity variations after the CFBG-PFI. In the proposed scheme, ultrasound that impinges on to the coiled fiber causes fringes shifts of the CFBG-FPI but has little effect on the phase difference between of the fast and slow polarizations. Hence, the fast and slow polarizations spectra of the CFBG-FPI shift simultaneously. The slope curves above cross section between fast and slow polarizations can be selected for highly sensitive ultrasonic signal detection. Since the slope curves above cross section between fast and slow polarizations are non-zero, the sensor is always response to ultrasonic signal by combining the fast and slow polarization signal with arbitrary laser wavelength and insensitive to environment changes to the sensor. Therefore, there is no need for laser wavelength locking nor temperature/strain compensation to the sensor which greatly reduce the complexity of the system.

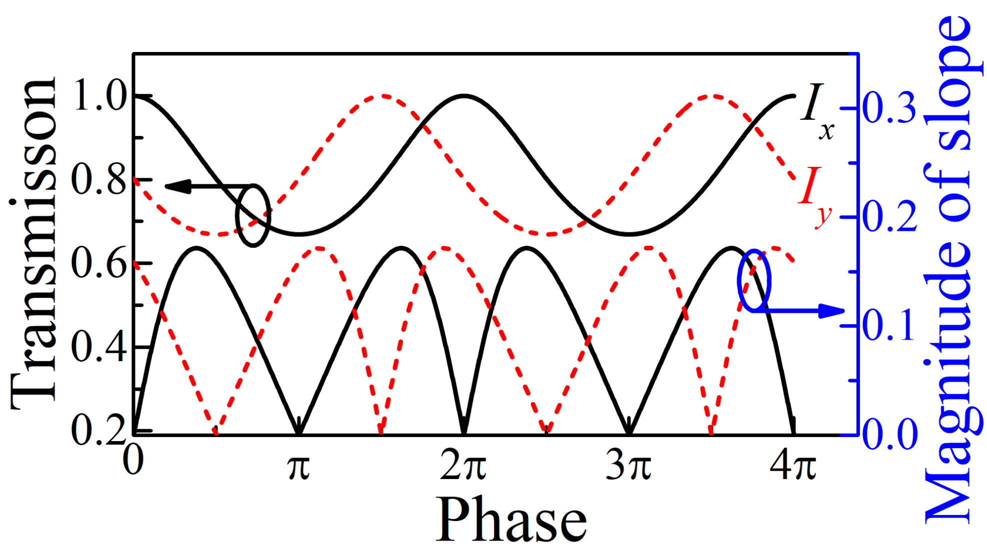

Figure 4.6: Spectral fringes at two polarizations and the corresponding slope (absolute value) when the phase shift of the fringes is 90 degree.

The sensor was demodulated in the transmission as shown in Fig. 4.4. Linearly polarized light from a narrow-linewidth laser with a single-mode fiber (SMF) pigtail passed through a polarization controller (PC) and the fiber-coil FP sensor. The transmitted light from the sensor was then directed to a polarization beam splitter (PBS) so that the light polarized at the two principal axes of the

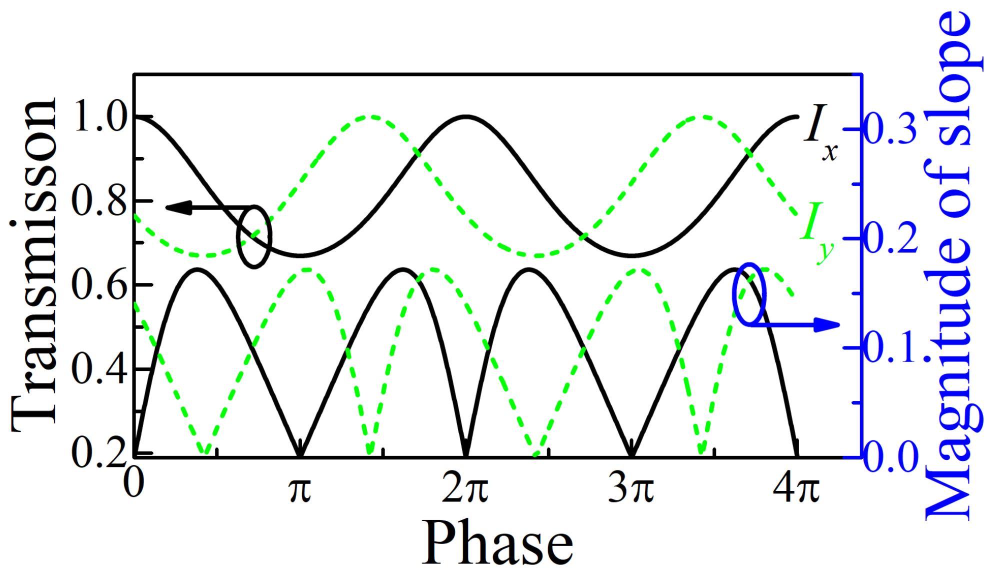

Figure 4.7: Spectral fringes at two polarizations and the corresponding slope (absolute value) when the phase shift of the fringes is 104 degree.

PM fiber were separated into two fibers and received by two photodetectors (PDs). The outputs form the PDs were amplified in the frequency range of 50 – 500 kHz with identical amplifiers and bandpass filters for ultrasonic detection, while the un-amplified dc components of the outputs were used to analyze the operating points. The PC was adjusted to control the polarization of light so that approximately equal optical power was distributed between the two polarization states. The fiber-sensor was glued to a aluminum plate for detecting the ultrasonic pulses on the plate generated by a piezoelectric transducer (HD 50, Physical Acoustics) glued close to the fiber sensor.

A pair of 5-mm CFBGs were fabricated on a PM fiber (PM1550-XP, Nufern) in-house using 193 nm UV laser and a chirped phase mask. The beat length of the PM fiber is less than 5 mm at 1550 nm. The Bragg wavelength of the phase mask is 1067.7 nm with a chirping rate of 4 nm/cm. The center-to-center separation between the two CFBGs was approximately 29 cm. The transmission spectra (normalized to the peak transmission) of the first CFBG and the CFBG-FP sensor, measured by an optical spectrum analyzer (OSA) with a resolution of 0.02 nm, are displayed in Fig. 4.8, showing a reflection window of > 2 nm centered at 1545 nm. Note that the fine sinusoidal-like fringes of the FP are not visible on the measured spectrum because of the low wavelength resolution of the OSA. The system is operated at around at 1545 nm around the center of the CFBG bandwidth where the reflectivity for each of the CFBGs is estimated to be ~ 10%.

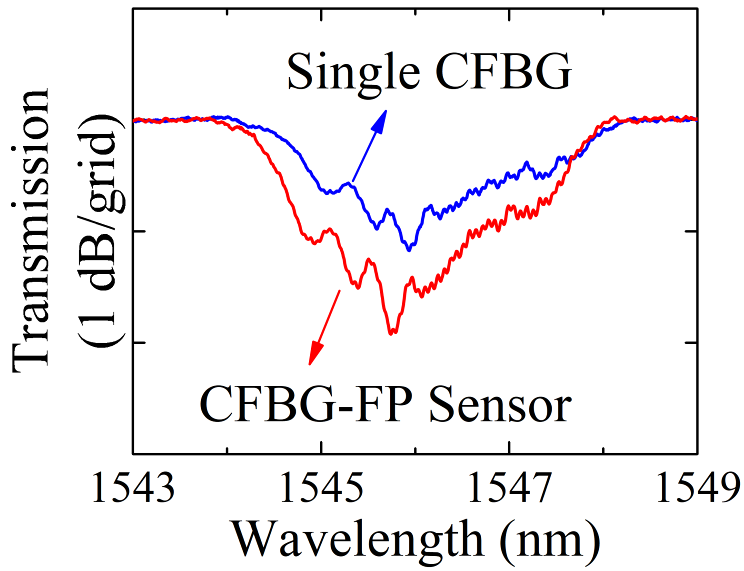

Figure 4.8: Normalized transmission spectra of one CFBG and the FP sensor measured by a whitelight source and an OSA.

The 10% reflectivity of the CFBGs caused the fringes to have a small but noticeable deviation from a perfectly sinusoidal form due to the non-negligible multipath interference. As a result, an exact phase delay of 90° between the two polarizations may not be optimal for quadrature demodulation. Simulation was carried out to find the optimal phase shift. Figure 4.6 and 4.7 show, respectively, the simulated fringes with a 90° phase shift and 104° phase shift and their corresponding absolute values of the spectral slope for an FP cavity formed by two mirrors with 10% reflectivity. Due to the deviation of the fringes from a perfectly sinusoidal waveform, the absolute values of the spectral slope for one polarization did not reach the maximum at fringe valleys or peaks of the other polarization for the case of 90° phase shift. The minimum response of the sensor is determined by the minimum magnitude of the intersection points of the slope curves for the two polarizations, which is 0.07 rad^{-1} for the case of 90° phase shift. An optical phase shift between the two fringes should maximize the minimum response, which occurs when the phase shift is 104° based on our simulation. In this case, the minimum response of the sensor increases to its maximum value of 0.1 rad^{-1}, as shown in Fig. 4.7.

To obtain the desirable phase shift of the fringes, the fiber between the two CFBGs were coiled

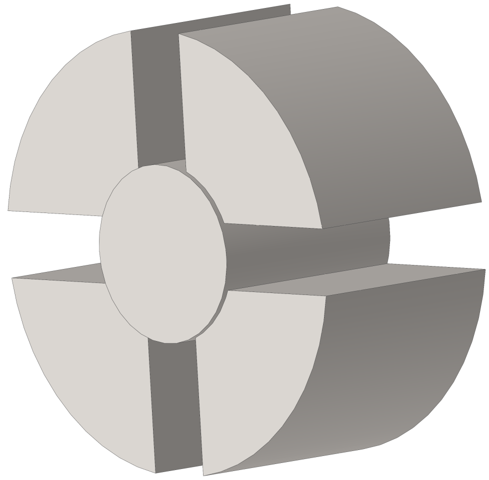

Figure 4.9: 3D printed structure of the mold.

with a diameter of ~ 12 mm with the help of a 3D printed mold (Fig. 4.9). A total optical loss of 0.3 dB was introduced with the fiber coil. The phase difference between the fringes of the two polarizations was continuously monitored during the coiling process using a wavelength-scanning laser along with the two PDs that gave enough resolution to resolve the fine fringes. The laser was scanned over a range of 10s pm centered around 1545 nm. By controlling the fiber length in the coiled region and twisting the PM fiber, we obtained a phase difference close to 104° for the two fringes.

Then the fiber coil was surface bonded onto the aluminum plate with super glue. Note that the CFBGs were protected with a metal tube and laid freely on the plate. Figure 4.10 is a picture of the fiber-coil sensor on the plate, an HD50 is glued on the right as the actuator, while an $R15\alpha$ is attached to the plate with coupling agent on the left as a reference sensor. Figure 4.11 shows the two transmission fringes of the fiber-coil FP sensor at the two polarizations measured after it was bonded on the plate. Both fringes have a similar free-spectral range of ~ 3.0 pm, which agree reasonably well with the theoretical values of 2.8 pm for an FP cavity with 29-cm optical fiber assuming the effective index of the fiber is 1.45. The small discrepancy may arise from the inaccuracy of the scanning range of the laser used for the fringe measurement. A spectral shift of approximately 0.9 pm was observed between the fringes of the two polarizations corresponding to 108° phase difference, which agree well with the theoretical design. In practice, both environmental

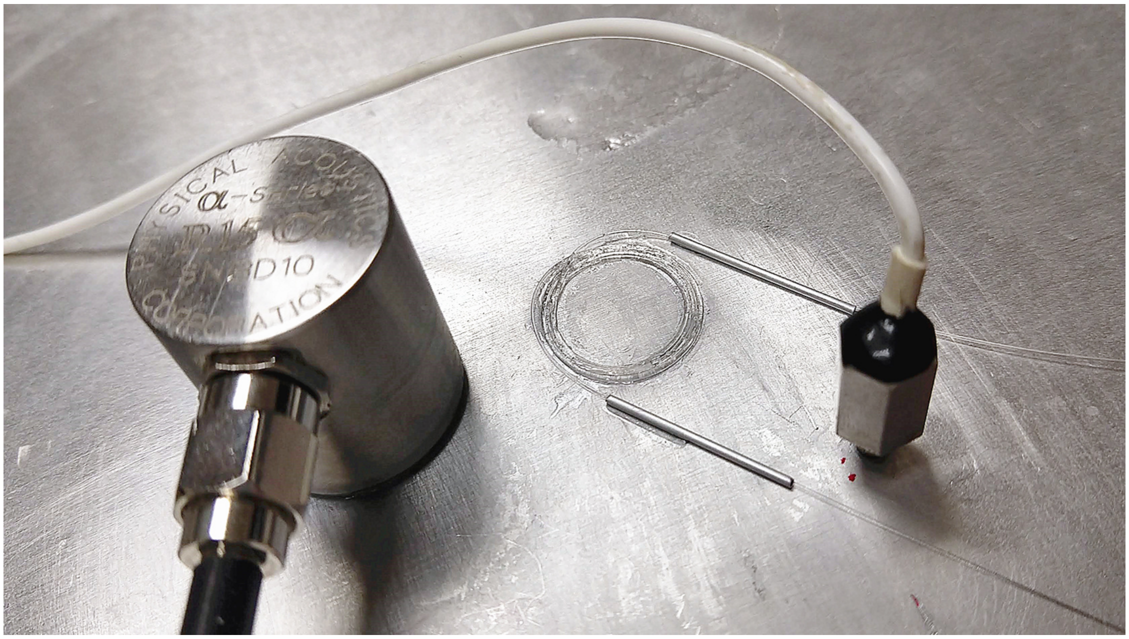

Figure 4.10: Picture of the sensor bonded on the plate with the CFBGs protected and laid freely on the plate.

perturbations and laser wavelength drift can change the operating point. We performed a quick check on the fringes by intentionally bending the plate to introduce background strain to the fiber. We observed that the two fringes experienced large spectral shift but maintained their relative phase difference.

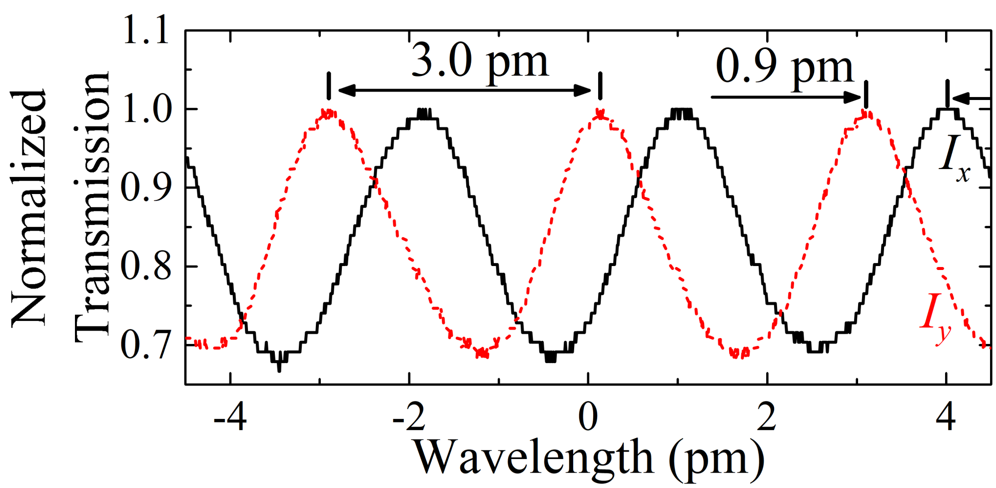

Figure 4.11: Measured spectral fringes at the two polarizations after the sensor was bonded on the plate.

4.1.3.2 Ultrasound detection

Then we demonstrated the proposed passive quadrature demodulation for ultrasound detection using the proposed system. The piezoelectric transducer was driven by a 5-cycle sinusoidal burst wave centered at 250 kHz with a peak-to-peak voltage of 20 V. The laser was free running with constant injection current and temperature. Tensile strain was applied to the fiber coil by bending the plate to change the position of the working point on the fringes, which caused the spectral shift of the fringes. Note that the CFBGs were not bonded on the plate surface and were free from the strain.

The responses of the sensor system to the ultrasound and the corresponding position of the operating point relative to the fringes are shown in Fig. 4.12. The dc components of the PD signals were used for working points analysis (Fig. 4.12(a-d)) and the corresponding ac components were amplified and filtered with bandpass filters (Fig. 4.12(e-h)). The sensor system was able to detect the ultrasonic signal with good signal-to-noise ratio (SNR) regardless of the background strain or the work point position. Specifically, Fig. 4.12(a) is the initial case where the laser wavelength was on fringe valley of the x-axis polarization but on the slope of the y-axis fringes. Figure 4.12(e) shows the corresponding responses of the two polarization channels. As expected, the channel of the x-axis exhibited little sensitivity, but the channel of the y-axis had a large response to the ultrasonic signal. Then the tensile strain was increased on the board, so that the fringes of both axes were shifted toward to the longer wavelength to change the operating point of the sensor. Figure 4.12(b) is the case where the laser wavelength reached to the point with zero-slope of the y-axis but a large slope of the x-axis. Figure 4.12(f) shows that the channel of the x-axis had a large response to the ultrasonic signal, while the channel of the y-axis barely captured the ultrasonic signal. When we continued to increase the tensile strain, the operating points were now on the spectral slope of both channels with the same slope directions (Fig. 4.12(c)), both channels captured the ultrasonic signals with consistent in-phase waveforms. As the tensile strain was further increased to the situation shown in Fig. 4.12(d), the laser wavelength was on the maximum absolute slopes of both axes but with opposite slope direction. In this case, both channels delivered maximum amplitude

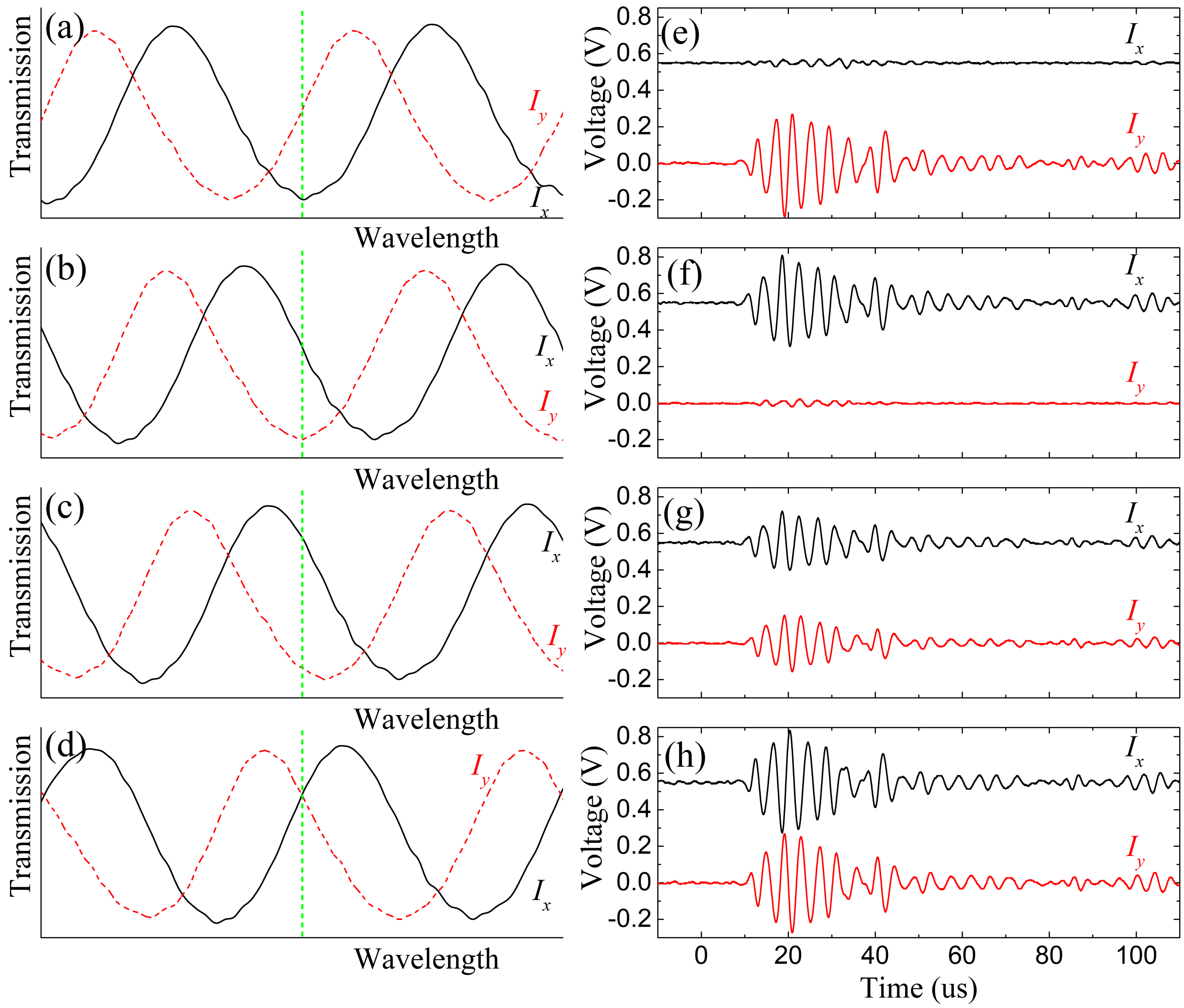

Figure 4.12: (a)-(d) Operating points (indicated by the green lines) relative to the transmission spectra of sensor at the two polarizations. (e)-(h) Corresponding detected ultrasonic signals from both polarization channels.

of the ultrasonic signal. Note that the detected ultrasonic waveforms by the two channels were out of phase, consistent with the opposite slope directions of the two fringes at the operating point.

4.1.4 Conclusions

In conclusion, we proposed and demonstrated a passive quadrature demodulation method using linearly polarized laser and a sensor with a birefringent low-finesse FP cavity. With precisely controlled birefringence in the FP cavity, the fringes probed by light polarized along the two principal axes can have a quadrature phase shift and can be separated detected. As a result, sensitive detection can be achieved by at least one of the polarization channels regardless of the laser wavelength relative to the fringes. We demonstrated the concept for fiber-optic ultrasonic sensor using a low FP cavity formed by two low-reflectivity CFBGs at the ends of a coiled PM fiber. A total phase delay of 108° between the fringes of the two polarizations of the PM fiber, optimized for the FP sensor with non-sinusoidal fringes, was obtained by controlling the length of the coiled fiber and twisting of the fiber. Quadrature spectra were extracted by a polarization beam splitter and measured by two photodetectors. The experimental results showed that the sensor is capable of detecting ultrasonic signal when the sensor spectra experience environmental drifts using a laser at fixed wavelength. Although transmission mode of the FP sensor was used in the demonstration, the demodulation method proposed here can also be used for the reflection mode of the FP sensor or sensors based on other types of interferometers.

4.2 Polarization-insensitive, omnidirectional fiber-optic ultrasonic sensor with quadrature demodulation

In this section, an ultrasonic sensor system based on a low-finesse Fabry-Perot interferometer (FPI) formed by two weak chirped fiber Bragg gratings (CFBGs) on a coiled single-mode fiber is proposed. The sensor system has several desirable features for practical applications in non-destructive evaluation and structure health monitoring. By controlling the birefringence of the fiber coil during the sensor fabrication, the sensor is made insensitive to the polarization variations of the laser source. The circular symmetric structure of the fiber coil also renders the omnidirectional response of the sensor to ultrasound. While the fiber coil is bonded directly to the structure, the CFBGs are suspended from the structure and free from large background strains with little reduction to the sensitivity of the sensor. The low-finesse FPI features sinusoidal reflection spectrum. Like the conventional phase generated carried technique, a phase modulator is utilized to implement quadrature demodulation. Therefore, the sensing system is adaptive to large background perturbations experienced by the fiber coil.

4.2.1 Introduction

Although fiber-optic ultrasonic sensors, particularly those based on fiber Bragg gratings (FBGs), have been widely envisioned as an attractive technology for non-destructive evaluation and structure health monitoring [6, 33], several challenges make few of these sensors commercially successful. Firstly, the sensor system should have a high sensitivity to ultrasound and be able to accommodate large but usually slowly varying background strain from environmental perturbations, such as structural deformation and ambient temperature variations. Secondly, the sensor operation should be independent on the laser polarization variations which are difficult to measure and control in practice. Thirdly, an omnidirectional response of the sensor is often desirable so that the ultrasonic signals from any directions can be detected with good sensitivity.

There are a few reports regarding the development of sensitive sensors and/or sensors adaptive to background strain. Detection sensitivity can be improved by optical resonators such as π-phase-shifted FBGs and FBG Fabry-Perot interferometers (FPIs) that have narrow spectral features with large spectral slopes [11, 55, 17]. A straightforward method to combat the spectral drift from environmental perturbations is to lock the laser wavelength to the linear range of the spectral slope [17, 77, 78, 44]. The method is hindered by the complicated locking system and limited availability of lasers with sufficient tuning range and speed. Remote bonding, where the FBG is free from the structure and the ultrasound is coupled to the fiber at a point away from the FBG region, is a unique technique that aims at isolating the sensor from background strain exerted by the structure [79, 80]. However, the sensor spectrum still experiences thermal drift due to ambient temperature variations. There are few studies to address the challenges in sensor birefringence and directivity. Manual polarization controllers (PCs) are often used to control the laser polarization. However, such approach is not desirable in practical applications where the laser polarization can be changed over a large range and in a random way by environmental perturbations such as fiber bending, twisting, and temperature variations. Automatic control of laser polarization through a feedback loop is challenging due to the lack of affordable and portable devices for polarization management. Most of the FBG sensors has a large directivity for detecting ultrasound on a solid surface because they are most sensitive to the strain along the fiber and show little sensitivity to strain transverse to the fiber [81].

4.2.2 Principle of operation

In this section, an adaptive ultrasonic sensor system with a polarization-insensitive and omnidirectional sensor is proposed and demonstrated. The proposed system is conceptually illustrated by Fig. 4.13. The sensor head is a low-finesse FPI with long cavity length formed by a pair of weak chirped FBGs (CFBGs) written on a bend-insensitive fiber. The fiber is made into a tight coil to reduce the footprint of the sensor and increase the ultrasonic frequency range. The long cavity length of the FPI results in fine fringes with large spectral slopes, giving rise to the high detection sensitivity. The circular symmetry of the fiber coil endows the sensor with omnidirectional response. The exact length of the coiled fiber is controlled so that the bend-induced birefringence generates a round-trip phase difference of $2N\pi$ (N=0,1,. . .) between the fast and slow axes, so that the fringes at the two principal polarization states overlap, which makes the sensor operation independent on the laser polarization. Meanwhile, the two CFBGs are suspended from the structure to isolate the background strains transferred from the structure. CFBGs have relatively wide reflection spectral windows to accommodate the spectral shift from ambient temperature variations. Similar to the conventional phase-generated carrier (PGC) demodulation scheme [69], passive quadrature demodulation for this sensor can be realized by the system shown in Fig. 4.13.

Output of the laser goes through a phase modulator and is then injected to the sensor via an optical circulator. The phase modulator is driven by a sinusoidal waveform delivered by a function generator. The returned optical signal is received by a photodetector (PD) whose output is split into two paths. One path goes through a band-pass filter which rejects all the components outside the frequency band of the ultrasound being detected, directly leading to the extracted ultrasonic signals. This path is here referred to as the DC channel. Using an electronic mixer, the other path is multiplied by a harmonic function with the same frequency applied to the phase modulator. The mixed signal passes through another bandpass filter which retains only the frequency components of

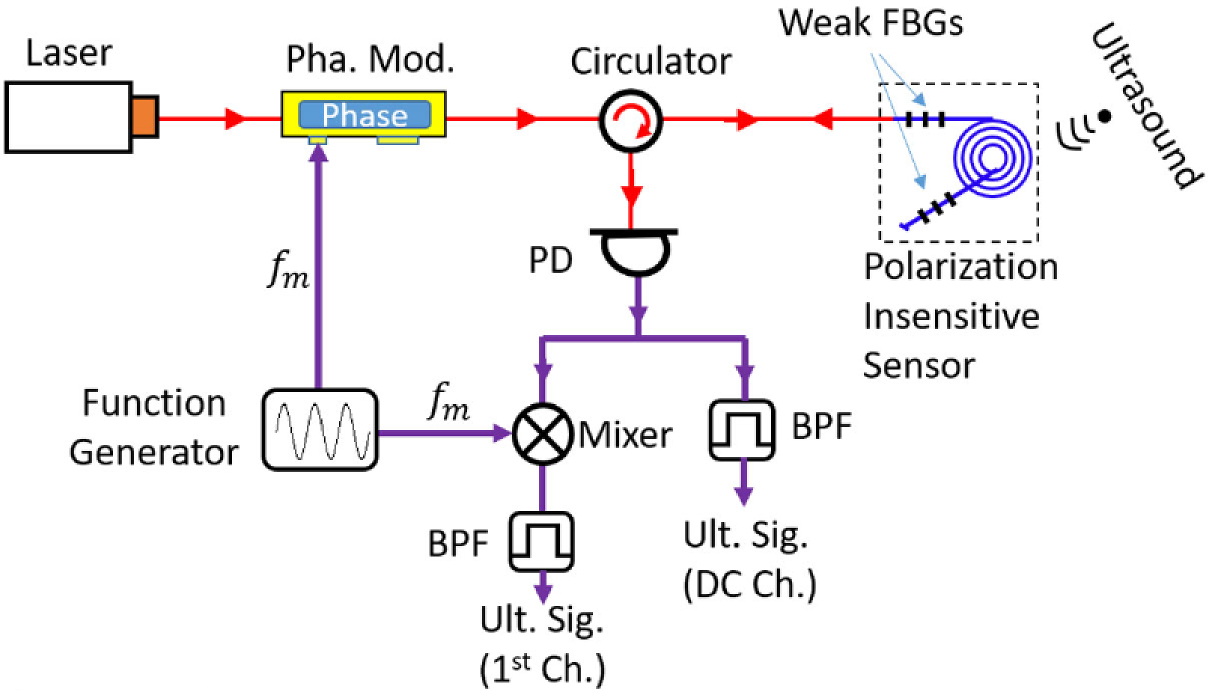

Figure 4.13: Schematic illustration of the system configuration for concept description. The FBGs are suspended from the structure to isolate large background strain. Pha. Mod., phase modulator; Ch., signal channel; Ult. Sig., ultrasonic signal; BPF, band-pass filter; FSR, free spectral range.

interest, leading to another ultrasonic signal. The second path is here referred to as the 1st harmonic channel. These two channels will be shown later, both theoretically and experimentally, to provide quadrature demodulation capability. We note that although fiber-coils with regular FBGs have been previously studied for ultrasonic detection [74, 52], they lack the key feature of polarization insensitivity possessed by the sensor here. Additionally, we studied the sensor directivity and presented a more practical method for sensor demodulation.

To better illustrate the system, a brief theoretical analysis is given. The phase modulated laser has a series of side lobes or harmonic components (Fig. 4.13(a)). Since the modulation depth is shallow in our experiments, as shown later, the electric field after phase modulation, E_i, can be expressed as [82]

$$\begin{aligned} E_i &= E_0 e^{j(\omega_0 t + \beta \sin \omega_m t)} \\ &\approx E_0[J_0(\beta)e^{j\omega_0 t} + J_1(\beta)e^{j(\omega_0+\omega_m)t} - J_1(\beta)e^{j(\omega_0-\omega_m)t}] \end{aligned} \tag{4.10}$$

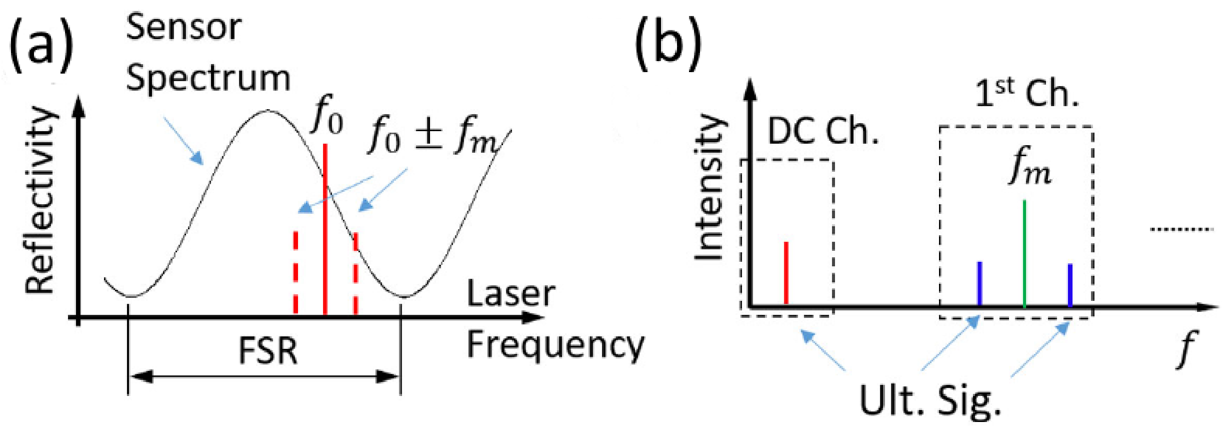

Figure 4.14: (a) sensor spectrum and phase modulated laser, and (b) signal demodulation channels.

where E_0 is amplitude of the laser field, ω_0 and ω_m are, respectively, the angular frequency of the laser and the phase modulation, J_0 and J_1 are, respectively, the 0th-order and the 1st-order Bessel functions of the first kind, β is modulation depth, and t denotes time. The reflection coefficient $r(\omega)$ of a low-finesse FPI sensor is given by [82]

$$r(\omega) = r_1 + r_2 e^{j2\omega nL/c} \tag{4.11}$$

where r_1 and r_2 are, respectively, the reflection coefficient of the front and back mirrors, n is effective refractive index of the fiber, L is the cavity length, c is speed of light in vacuum. Here, r_1 and r_2 are assumed to be the same for both the original laser line and the side lobes. Then, the total reflected electric field is given by

$$\begin{aligned} E_r = E_0[J_0(\beta)e^{j\omega_0 t}r(\omega_0) + J_1(\beta)e^{j(\omega_0+\omega_m)t}r(\omega_0+\omega_m) \\ - J_1(\beta)e^{j(\omega_0-\omega_m)t}r(\omega_0-\omega_m)] \end{aligned} \tag{4.12}$$

The optical power P received by the PD is given by

$$P \propto E_r E_r^* \tag{4.13}$$

where "*" denotes complex conjugate. In the frequency domain, the signal output from the PD consists of discrete channels with a separation of the modulation frequency, as illustrated in Fig.

4.14(b). The ultrasonic signal in the DC channel can be extracted directly by a bandpass filter, while the ultrasonic signal in the harmonic channels is obtained by the combination of a mixer and a bandpass filter. In practice, only the ultrasonic signals in the DC and the 1st harmonic channels are extracted. The other higher order harmonic channels are ignored.

Usually, r_1 and r_2 are complex numbers which include a phase shift upon reflection from an FBG [21]. However, for simplicity and without losing generality, the phase shift is ignored here. In fact, consideration of the phase shift only leads to an extra constant phase besides the ϕ_0 shown later in Eqs. 4.14 and 4.15. With such simplification, r_1 and r_2 are real and positive numbers. After some algebra, the voltage output from the DC channel reads

$$V_{DC} \propto 2P_0 r_1 r_2 [J_0^2(\beta) + 2J_1^2(\beta)\cos\phi_m]\cos\phi_0 \tag{4.14}$$

and the voltage output from the 1st harmonic channel reads

$$V_{1st} \propto -8P_0 r_1 r_2 J_0(\beta) J_1(\beta) \left|\sin\frac{\phi_m}{2}\right| \sin\phi_0 \tag{4.15}$$

where P_0 is the laser power before the phase modulator, $\phi_0 = 2\omega_0 nL/c$, and $\phi_m = 2\omega_m nL/c$. In the presence of ultrasound, both ϕ_0 and ϕ_m are modulated. However, ϕ_m is virtually a constant since the optical frequency is much higher than that of the rf modulation frequency, i.e., $\omega_0 \gg \omega_m$. Therefore, the ultrasonic signals are only included implicitly in ϕ_0. Equations 4.14 and 4.15 represent the outputs of the two channels with quadrature phase shift so that the ultrasound signal can be extracted regardless of the spectral shifts caused by environmental perturbations. Note that the signal amplitude is a function of both the phase modulation depth and frequency. It is worth mentioning that, in deriving Eq. 4.15, a phase shift is needed in the sinusoidal function sent to the mixer so that amplitude of the extracted ultrasonic signal is maximized. This phase shift is also dependent on the frequency of phase modulation.

4.2.3 Sensor structure and experiment setup

To experimentally demonstrate the system, two 5-mm long CFBGs with reflectivity of around 20% centered around 1550 nm were fabricated in-house on a bend-insensitive fiber (F-SBC, Newport). The length of the fiber between the CFBGs was about 39 cm. Assembly of the fiber coil was facilitated by a devised 3-D printed mold. Diameters of the inner most and outer most loops were 8 mm and 10 mm, respectively, resulting in an average bend-induced birefringence of 5.18×10^{-5} [75]. Therefore, a bending length of around 37.4 cm produced a round-trip phase difference of 50π between the fast and slow axes at 1550 nm. As aforementioned, a phase difference of an integer multiple of 2π would make the sensor operation independent on the laser polarization. The bending length was fine-tuned by monitoring the FPI spectrum as the laser polarization was randomly varied (see Fig. 4.15) for more details). When a polarization-insensitive FPI was reached, the fiber coil was fixed using fast-cured glue.

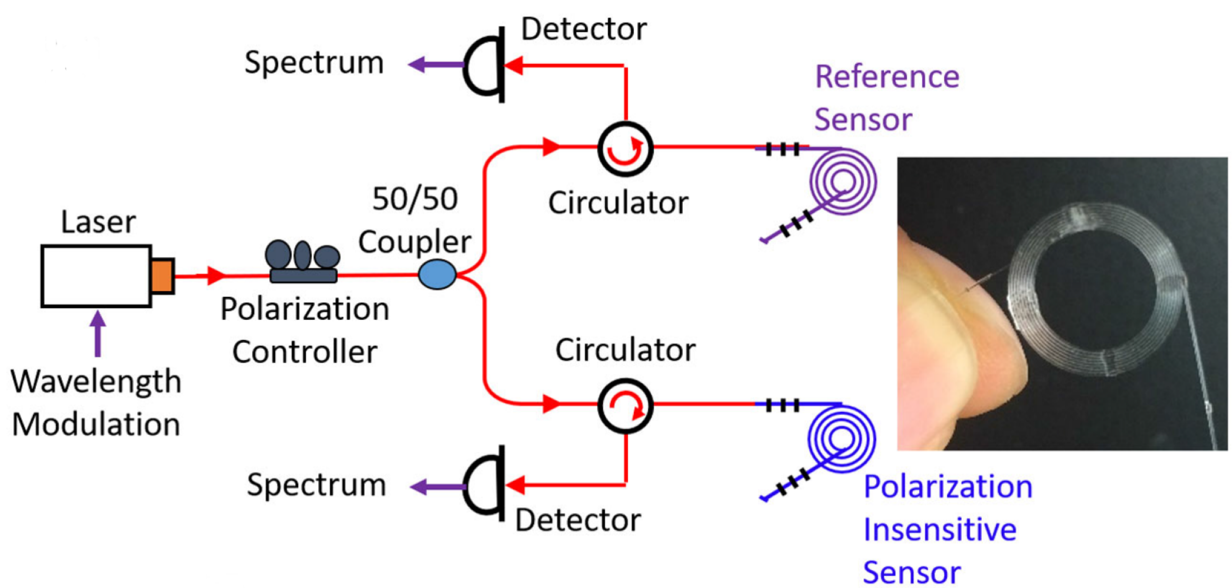

Figure 4.15: Experimental setup to study the sensitivity of the sensor to laser polarization and an image of the fiber coil.

The spectral response of the sensor to polarization variation was studied using the setup shown in Fig. 4.15. Again, polarization of the laser was manually and randomly tuned using a PC. After the PC, the laser was split into two paths using a 50/50 coupler. Using a circulator, the light in one path was sent to a reference sensor which was polarization sensitive, while the other path was connected to the polarization-insensitive sensor. Wavelength of the laser was scanned using a triangle waveform, and the returned spectrum was separately received by a PD and displayed on an oscilloscope for both sensors. This arrangement gave a direct comparison between the responses of the two sensors. The spectra in the top, middle and bottom panels of Fig. 4.16 were recorded for three different polarization states of the laser. Apparently, while the spectrum of the reference sensor showed different phases or shapes for the three polarization states, the spectrum of the maintained its sinusoidal shape with no visible changes in both its amplitude and phase.

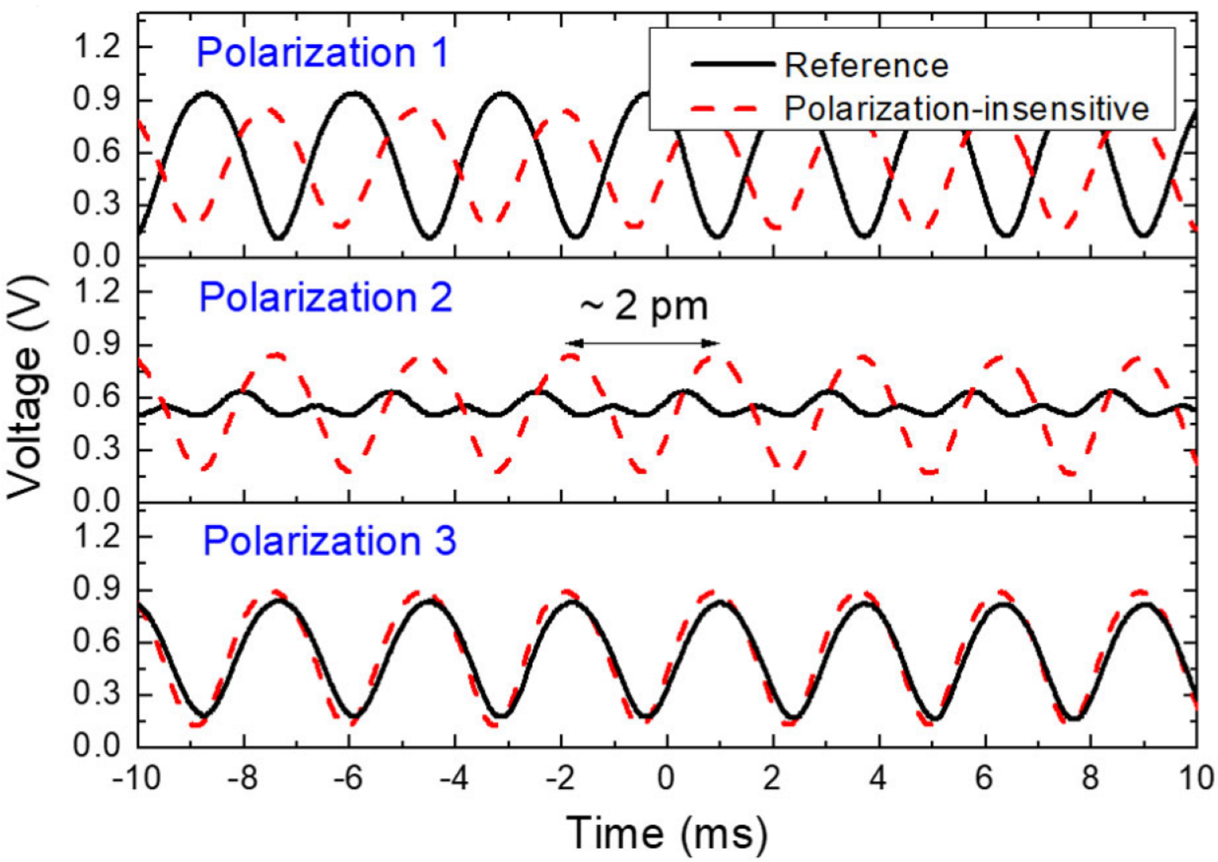

Figure 4.16: Spectra of the FPIs probed by the laser at different polarizations.

4.2.4 Directivity of the sensor

The directivity of the sensor was examined using the setup shown in Fig. 4.17. The sensor was glued to an 0.8 mm thick aluminum plate. A piezo transducer was moved to different angular positions around the sensor with a step size of 30° (see the inset of Fig. 4.17). Wavelength of the laser was tuned to a point on the fringes with maximum slope. The peak-to-peak amplitude was used as the response. Three cycles of measurements were performed to ensure better reliability. The results are summarized in Fig. 4.18. The sensor shows rather consistent responses for different angular positions. The small deviation from a perfectly omnidirectional response might arise from the slightly different ultrasound coupling efficiency from the piezo transducer to the plate.

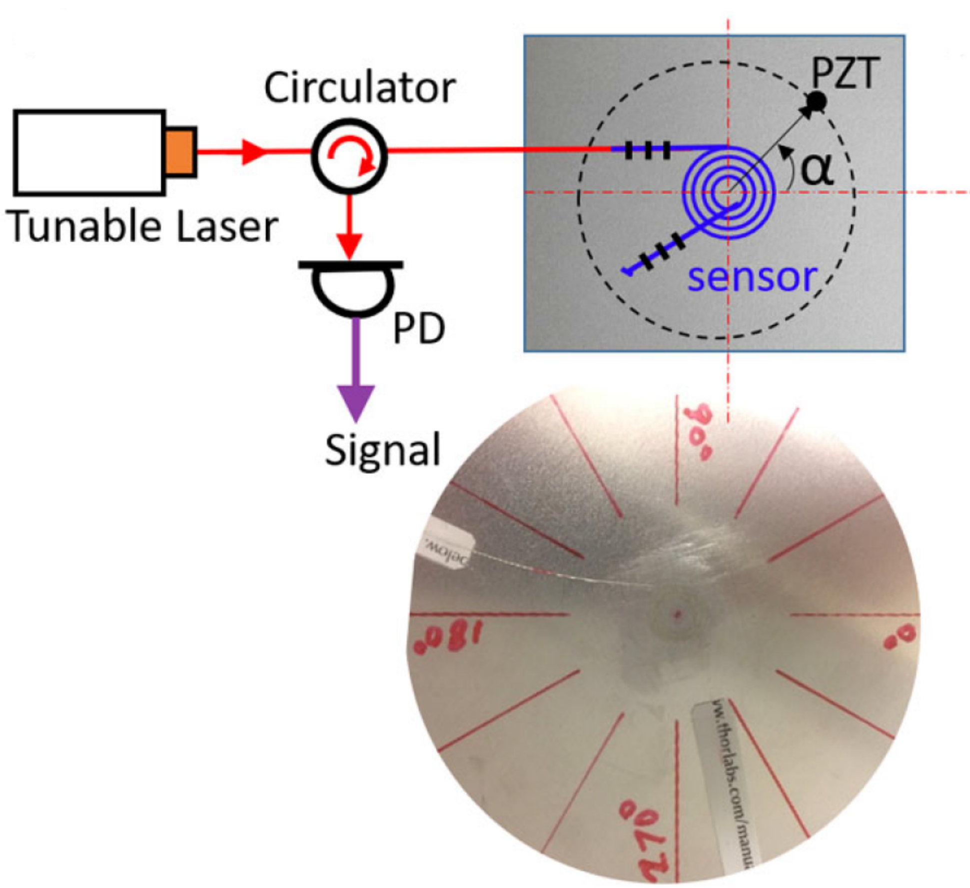

Figure 4.17: Experimental setup and an image of the sensor glued onto the aluminum plate.

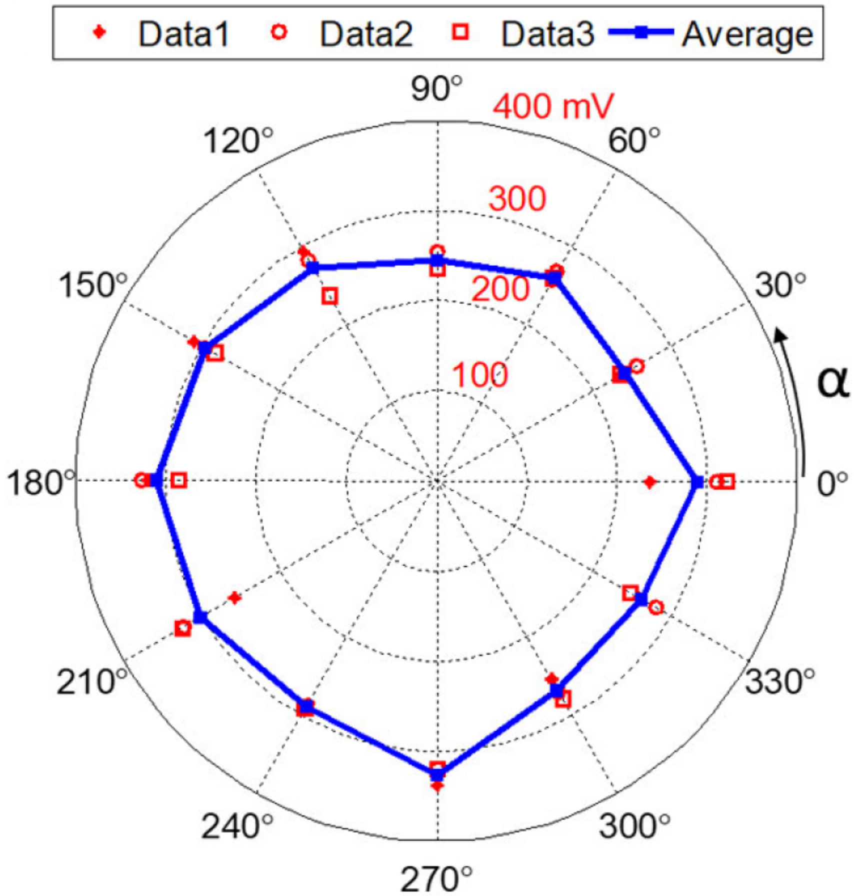

Figure 4.18: Demonstration of sensor directivity, sensor responses at different incident angles.

4.2.5 Ultrasound detection with quadrature demodulation

Finally, we demonstrated the quadrature demodulation for ultrasound detection using the setup shown in Fig. 4.19. Polarization of the laser source (6328-H, New Focus) was adjusted to match the phase modulator via a PC. A dual-channel function generator was used to drive the phase modulator. The phase modulated light was split into two arms using a 50/50 coupler. In one arm, the laser lines were monitored by a high-finesse scanning FPI with a built-in PD. Note that this arm was merely for optimizing the driving signal of the phase modulator and is not needed in practical applications. In another arm, the light propagated through a circulator and reached the sensor and the returned optical signal was divided into two channels using another 50/50 coupler. In one channel (dc Ch.), the output form the PD passed successively through a 40-dB amplifier and a 30-500 kHz bandpass filter. In the other channel (1st Ch.), the PD output was sent to a mixer to mix with a sinusoidal wave at the phase modulation frequency and with appropriate phase before passing through another set of similar amplifier and bandpass filter.

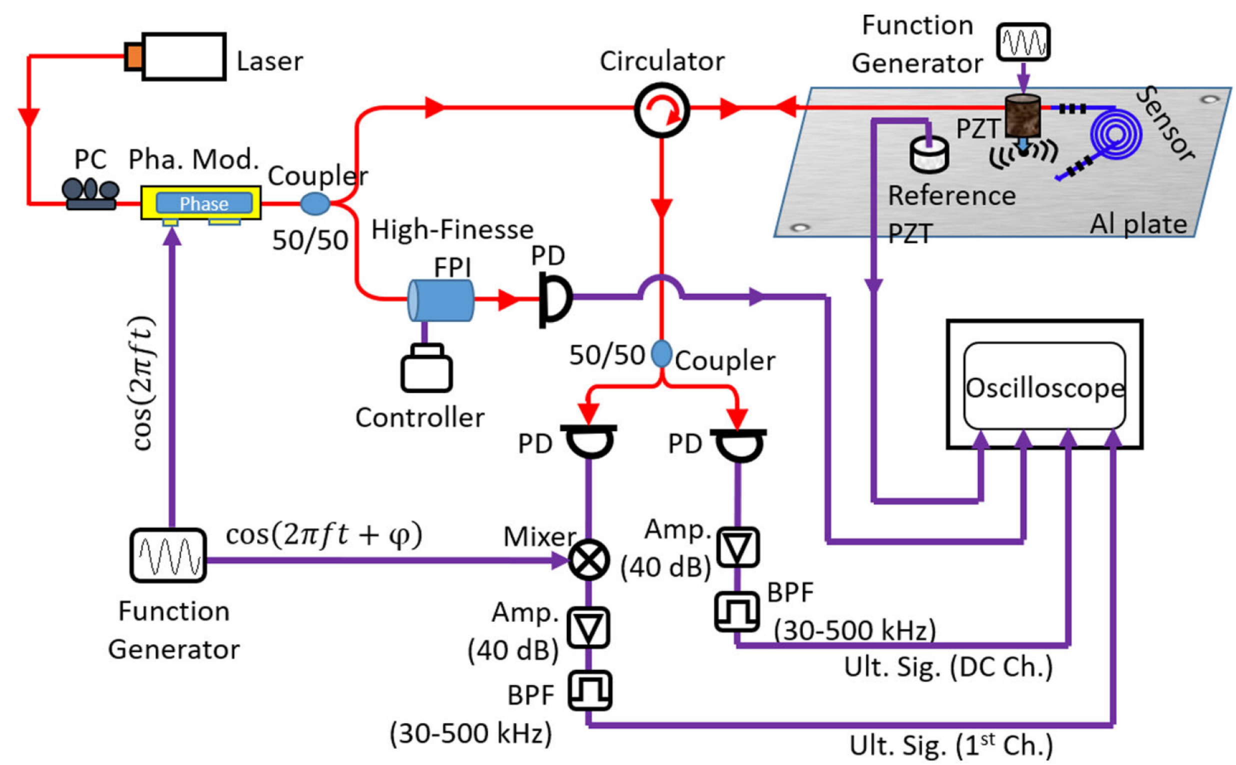

Figure 4.19: Experimental setup for the quadrature demonstration of the sensor. Amp., amplifier.

The laser lines measured by the canning-FPI are shown in Fig. 4.20. There was only one laser line without phase modulation (black curve in Fig. 4.20). When the phase modulation was turned on, two side lobes showed up (red curve in Fig. 4.20). The relative intensity between the original laser and the side lobes suggests a modulation depth (β in Eq. 4.10) of around 0.97. This small modulation depth leads to a relatively strong 1st harmonic component and negligible higher-order harmonics.

Finally, the quadrature demodulation was demonstrated, and the results are displayed in Fig. 4.21, in which all the waveforms were the average of four measurements. The top figure in Fig. 4.21 shows the five different operating points (depicted by the different relative positions of the original laser line on the spectral fringes) at which the ultrasound waveforms were captured by the two

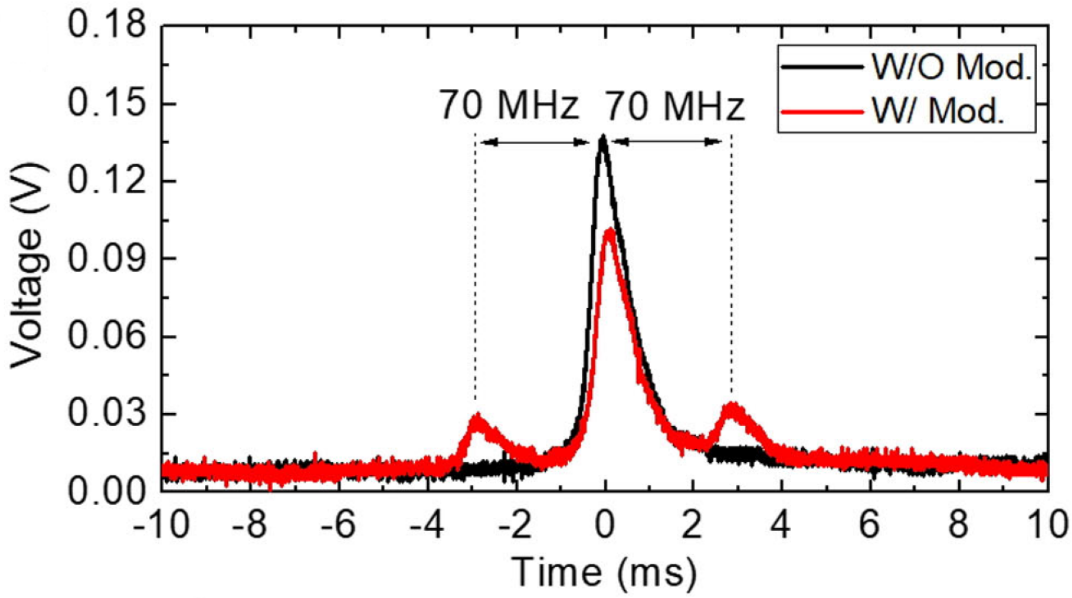

Figure 4.20: Spectrum of the phase modulated laser measured by the scanning-FPI.

channels and the corresponding channel outputs are shown in the bottom of Fig. 4.21. Positions P1 and P5 were the cases where the laser line was at the peak and valley of the fringes, respectively. As expected, the DC channel did not record any ultrasound signals (see the according black curves) and the 1st harmonic channel registered the ultrasound signal with the largest amplitude. The situation for position P3, which was around the middle point of the reflection spectrum, was opposite. In this case, the 1st harmonic channel did not record the ultrasound, while the DC channel captured the ultrasound. At the intermediate positions P2 and P4, both channels were able to detect the ultrasound, but with reduced amplitude. Also note that signals from both channels were out of phase at position P2 but in phase at position P4. As a reference, the ultrasound waveform detected by a commercial piezo sensor is also shown (blue curve at the bottom of Fig. 4.21).

4.2.6 Conclusions

In summary, we studied an ultrasonic sensor system promising for practical applications. The sensor head consists of a pair of identical weak CFBGs inscribed in a bending-insensitive fiber, forming a low-finesse FPI with fine, sinusoidal-like spectral fringes. The fiber between the two

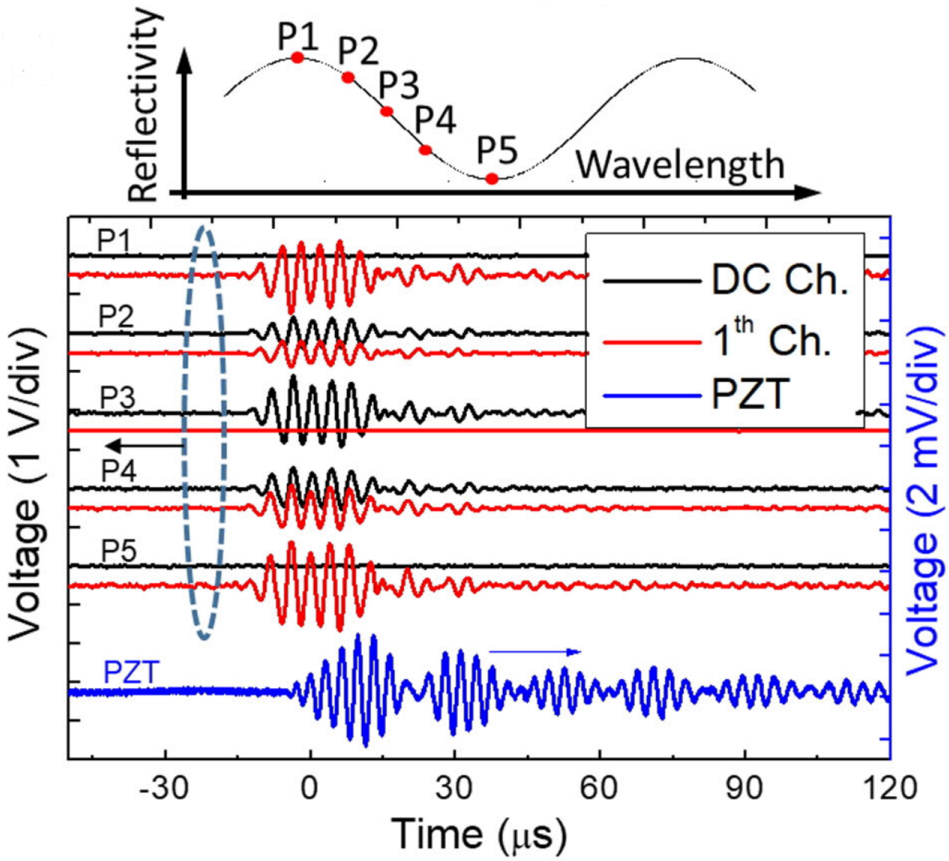

Figure 4.21: Ultrasound waveforms captured by the two channels (bottom) when the laser is at different operating points (upper).

FBGs is coiled tightly, which endows the sensor with omnidirectional response. In the meantime, length of the coiled fiber is controlled so that the phase shift of the two fringes corresponding to the two principal axes is an integer multiple of 2π. Satisfaction of this condition makes the sensor insensitive to the laser polarization, a desirable feature in practical applications. A signal demodulation system similar to PGC method is utilized to realize passive quadrature demodulation, leading to an ultrasonic sensor system adaptive to environmental perturbations.

CHAPTER 5

CONCLUSION AND FUTURE WORK

5.1 Summary

This dissertation presented a series of studies which explored the use of the fiber Bragg grating based optical fiber sensors for dynamic strain measurement. Regular fiber Bragg gratings provide a small reflection bandwidth with gentle slopes, are very difficult and inefficient to measure dynamic strain variations. Therefore, new sensor structure and demodulation techniques must be developed and optimized. Throughout this dissertation the new sensor structure is developed based on chirped fiber Bragg gratings which provides a relative large reflection bandwidth compare to regular fiber Bragg gratings. An Fabry-Perot cavity is formed with a pair of chirped fiber Bragg gratings. Then resonance peaks formed within the reflection bandwidth which greatly enhance the resolution and sensitivity. The dynamic strain measurement with proposed sensors is extensively studied. We first demonstrated a novel high resolution, large dynamic range strain sensor with Fabry-Perot cavity using cascaded chirped fiber Bragg gratings with opposite chirp directions. Then we proposed and demonstrated a high-finesse short cavity sensors for acoustic emission and ultrasonic detection in structure crack and from piezoelectric actuator. At last, we studied low-finesse long cavity sensor with coil structure to measure ultrasonic waves without laser wavelength locking and immune to the background environmental changes.

5.2 Future Work

In this dissertation, we have built an ultrasensitive ultrasound detection platform using an intra-cavity phase-shifted fiber Bragg grating in self-injection-locked diode laser. The self-injection locking technique is convenient and powerful regarding to the laser frequency noise reduction. However, it is not easy to tune the lasing wavelength after locking the laser, due to the random drifting within the locking range. Changing the injection current of the laser and the Bragg wavelength of the sensor are easy and straight forward. But we first have to gain the knowledge of the laser wavelength relative to the locking range before we make any change. One potential solution is a rapid scanning of the laser injection current under the weak self-injection locking condition. Then the center of the laser injection current can be changed to examine the "error" signal of the DC output of the photodiode. The "error" signal should have significant difference at the edges of the locking range. And the DC signal will drop to zero if the laser is unlocked. By this way, the laser wavelength can be extracted without breaking the self-injection locking status.

Regarding to the coiled fiber low-finesse long cavity sensor with phase generated carrier technique, the potential of the higher order mode can be further explored to extract the ultrasound signal that does not fade with the environmental perturbations.

BIBLIOGRAPHY

BIBLIOGRAPHY

[1] A. D. Kersey, M. A. Davis, H. J. Patrick, M. LeBlanc, K. Koo, C. Askins, M. Putnam, and E. J. Friebele, "Fiber grating sensors," *Journal of Lightwave Technology*, vol. 15, no. 8, pp. 1442–1463, 1997.

[2] Y.-J. Rao, D. J. Webb, D. A. Jackson, L. Zhang, and I. Bennion, "In-fiber bragg-grating temperature sensor system for medical applications," *Journal of Lightwave Technology*, vol. 15, no. 5, pp. 779–785, 1997.

[3] C. E. Campanella, A. Cuccovillo, C. Campanella, A. Yurt, and V. Passaro, "Fibre bragg grating based strain sensors: review of technology and applications," *Sensors*, vol. 18, no. 9, p. 3115, 2018.

[4] Y. Zhu and A. Wang, "Miniature fiber-optic pressure sensor," *IEEE Photonics Technology Letters*, vol. 17, no. 2, pp. 447–449, 2005.

[5] J. Mora, A. Diez, J. Cruz, and M. Andres, "A magnetostrictive sensor interrogated by fiber gratings for dc-current and temperature discrimination," *IEEE Photonics Technology Letters*, vol. 12, no. 12, pp. 1680–1682, 2000.

[6] Q. Wu, Y. Okabe, and F. Yu, "Ultrasonic structural health monitoring using fiber bragg grating," *Sensors*, vol. 18, no. 10, p. 3395, 2018.

[7] J. Leng and A. Asundi, "Non-destructive evaluation of smart materials by using extrinsic fabry–perot interferometric and fiber bragg grating sensors," *NDT & E International*, vol. 35, no. 4, pp. 273–276, 2002.

[8] S. Liang, C. Zhang, W. Lin, L. Li, C. Li, X. Feng, and B. Lin, "Fiber-optic intrinsic distributed acoustic emission sensor for large structure health monitoring," *Optics Letters*, vol. 34, no. 12, pp. 1858–1860, 2009.

[9] R. Kashyap, *Fiber bragg gratings*. Academic press, 2009.

[10] G. Meltz and W. W. Morey, "Bragg grating formation and germanosilicate fiber photosensitivity," in *International workshop on photoinduced self-organization effects in optical fiber*, vol. 1516. International Society for Optics and Photonics, 1991, pp. 185–199.

[11] A. Rosenthal, D. Razansky, and V. Ntziachristos, "High-sensitivity compact ultrasonic detector based on a pi-phase-shifted fiber bragg grating," *Optics Letters*, vol. 36, no. 10, pp. 1833–1835, 2011.

[12] Y. O. Barmenkov, D. Zalvidea, S. Torres-Peiró, J. L. Cruz, and M. V. Andrés, "Effective length of short fabry-perot cavity formed by uniform fiber bragg gratings," *Optics Express*, vol. 14, no. 14, pp. 6394–6399, 2006.

[13] A. Wada, S. Tanaka, and N. Takahashi, “Optical fiber vibration sensor using fbg fabry–perot interferometer with wavelength scanning and fourier analysis,” *IEEE Sensors Journal*, vol. 12, no. 1, pp. 225–229, 2011.

[14] L. Hu, G. Liu, Y. Zhu, X. Luo, and M. Han, “Laser frequency noise cancelation in a phase-shifted fiber bragg grating ultrasonic sensor system using a reference grating channel,” *IEEE Photonics Journal*, vol. 8, no. 1, pp. 1–8, 2016.

[15] G. Cranch, L. Johnson, M. Algren, S. Heerschap, G. Miller, T. Marunda, and R. Holtz, “Crack detection in riveted lap joints using fiber laser acoustic emission sensors,” *Optics Express*, vol. 25, no. 16, pp. 19 457–19 467, 2017.

[16] R. Drever, J. L. Hall, F. Kowalski, J. Hough, G. Ford, A. Munley, and H. Ward, “Laser phase and frequency stabilization using an optical resonator,” *Applied Physics B*, vol. 31, no. 2, pp. 97–105, 1983.

[17] Q. Zhang, Y. Zhu, X. Luo, G. Liu, and M. Han, “Acoustic emission sensor system using a chirped fiber-bragg-grating fabry–perot interferometer and smart feedback control,” *Optics Letters*, vol. 42, no. 3, pp. 631–634, 2017.

[18] V. Giurgiutiu, C. Roman, B. Lin, and E. Frankforter, “Omnidirectional piezo-optical ring sensor for enhanced guided wave structural health monitoring,” *Smart Materials and Structures*, vol. 24, no. 1, p. 015008, 2014.

[19] A. Yariv, “Coupled-mode theory for guided-wave optics,” *IEEE Journal of Quantum Electronics*, vol. 9, no. 9, pp. 919–933, 1973.

[20] W.-P. Huang, “Coupled-mode theory for optical waveguides: an overview,” *JOSA A*, vol. 11, no. 3, pp. 963–983, 1994.

[21] T. Erdogan, “Fiber grating spectra,” *Journal of Lightwave Technology*, vol. 15, no. 8, pp. 1277–1294, 1997.

[22] V. Mizrahi and J. E. Sipe, “Optical properties of photosensitive fiber phase gratings,” *Journal of Lightwave Technology*, vol. 11, no. 10, pp. 1513–1517, 1993.

[23] M. Yamada and K. Sakuda, “Analysis of almost-periodic distributed feedback slab waveguides via a fundamental matrix approach,” *Applied Optics*, vol. 26, no. 16, pp. 3474–3478, 1987.

[24] X. Dong, W. Liu, D. Wang, and M. Wu, “Study on fabry–perot cavity consisting of two chirped fiber bragg gratings,” *Optical Fiber Technology*, vol. 18, no. 4, pp. 209–214, 2012.

[25] S. Zheng, Y. Zhu, and S. Krishnaswamy, “Fiber humidity sensors with high sensitivity and selectivity based on interior nanofilm-coated photonic crystal fiber long-period gratings,” *Sensors and Actuators B: Chemical*, vol. 176, pp. 264–274, 2013.

[26] S. Zheng, M. Ghandehari, and J. Ou, “Photonic crystal fiber long-period grating absorption gas sensor based on a tunable erbium-doped fiber ring laser,” *Sensors and Actuators B: Chemical*, vol. 223, pp. 324–332, 2016.

[27] K. Koo, M. LeBlanc, T. Tsai, and S. Vohra, "Fiber-chirped grating fabry-perot sensor with multiple-wavelength-addressable free-spectral ranges," *IEEE Photonics Technology Letters*, vol. 10, no. 7, pp. 1006–1008, 1998.

[28] Y. Rao, Z. Ran, and C. Zhou, "Fiber-optic fabry-perot sensors based on a combination of spatial-frequency division multiplexing and wavelength division multiplexing formed by chirped fiber bragg grating pairs," *Applied Optics*, vol. 45, no. 23, pp. 5815–5818, 2006.

[29] A. Wada, K. Ikuma, M. Syoji, S. Tanaka, and N. Takahashi, "Wide-dynamic-range high-resolution fiber fabry–perot interferometric sensor with chirped fiber bragg gratings," *Journal of Lightwave Technology*, vol. 31, no. 19, pp. 3176–3180, 2013.

[30] K. Ikuma, A. Wada, S. Tanaka, K. Omichi, and N. Takahashi, "Optical fiber sensing with chirped fbg fabry-perot interferometer: vibration measurement," in *OFS2012 22nd International Conference on Optical Fiber Sensors*, vol. 8421. International Society for Optics and Photonics, 2012, p. 84213R.

[31] W. Loh, M. Cole, M. N. Zervas, S. Barcelos, and R. Laming, "Complex grating structures with uniform phase masks based on the moving fiber–scanning beam technique," *Optics Letters*, vol. 20, no. 20, pp. 2051–2053, 1995.

[32] K. Numata, J. R. Chen, and S. T. Wu, "Precision and fast wavelength tuning of a dynamically phase-locked widely-tunable laser," *Optics Express*, vol. 20, no. 13, pp. 14 234–14 243, 2012.

[33] G. Wild and S. Hinckley, "Acousto-ultrasonic optical fiber sensors: Overview and state-of-the-art," *IEEE Sensors Journal*, vol. 8, no. 7, pp. 1184–1193, 2008.

[34] D. C. Betz, G. Thursby, B. Culshaw, and W. J. Staszewski, "Acousto-ultrasonic sensing using fiber bragg gratings," *Smart Materials and Structures*, vol. 12, no. 1, p. 122, 2003.

[35] I. M. Perez, H. Cui, and E. Udd, "Acoustic emission detection using fiber bragg gratings," in *Smart Structures and Materials 2001: Sensory Phenomena and Measurement Instrumentation for Smart Structures and Materials*, vol. 4328. International Society for Optics and Photonics, 2001, pp. 209–215.

[36] M. Vidakovic, C. McCague, I. Armakolas, T. Sun, J. S. Carlton, and K. T. Grattan, "Fibre bragg grating-based cascaded acoustic sensors for potential marine structural condition monitoring," *Journal of Lightwave Technology*, vol. 34, no. 19, pp. 4473–4478, 2016.

[37] H. Tsuda, K. Kumakura, and S. Ogihara, "Ultrasonic sensitivity of strain-insensitive fiber bragg grating sensors and evaluation of ultrasound-induced strain," *Sensors*, vol. 10, no. 12, pp. 11 248–11 258, 2010.

[38] B. W. Drinkwater and P. D. Wilcox, "Ultrasonic arrays for non-destructive evaluation: A review," *NDT & E International*, vol. 39, no. 7, pp. 525–541, 2006.

[39] J. L. Rose, "Ultrasonic guided waves in structural health monitoring," in *Key Engineering Materials*, vol. 270. Trans Tech Publ, 2004, pp. 14–21.

[40] M. Parrilla, J. Anaya, and C. Fritsch, “Digital signal processing techniques for high accuracy ultrasonic range measurements,” *IEEE Transactions on Instrumentation and Measurement*, vol. 40, no. 4, pp. 759–763, 1991.

[41] M. Tanter and M. Fink, “Ultrafast imaging in biomedical ultrasound,” *IEEE Transactions on Ultrasonics, Ferroelectrics, and Frequency Control*, vol. 61, no. 1, pp. 102–119, 2014.

[42] M. Majumder, T. K. Gangopadhyay, A. K. Chakraborty, K. Dasgupta, and D. K. Bhattacharya, “Fibre bragg gratings in structural health monitoring—present status and applications,” *Sensors and Actuators A: Physical*, vol. 147, no. 1, pp. 150–164, 2008.

[43] T. Liu and M. Han, “Analysis of π-phase-shifted fiber bragg gratings for ultrasonic detection,” *IEEE Sensors Journal*, vol. 12, no. 7, pp. 2368–2373, 2012.

[44] G. Liu and M. Han, “Wavelength locking of a diode laser to the maximal slope of a π-phase-shifted fiber bragg grating for acoustic emission detection,” *IEEE Sensors Journal*, vol. 18, no. 22, pp. 9257–9262, 2018.

[45] D. Gatti, G. Galzerano, D. Janner, S. Longhi, and P. Laporta, “Fiber strain sensor based on a π-phase-shifted bragg grating and the pound-drever-hall technique,” *Optics Express*, vol. 16, no. 3, pp. 1945–1950, 2008.

[46] B. Dahmani, L. Hollberg, and R. Drullinger, “Frequency stabilization of semiconductor lasers by resonant optical feedback,” *Optics Letters*, vol. 12, no. 11, pp. 876–878, 1987.

[47] J. B. Escobedo, V. Spirin, C. López-Mercado, P. Mégret, I. Zolotovskii, and A. Fotiadi, “Self-injection locking of the dfb laser through an external ring fiber cavity: Polarization behavior,” *Results in Physics*, vol. 6, pp. 59–60, 2016.

[48] Y. Zhao and C. Shu, “Single-mode operation characteristics of a self-injection seeded fabry-perot laser diode with distributed feedback from a fiber grating,” *IEEE Photonics Technology Letters*, vol. 9, no. 11, pp. 1436–1438, 1997.

[49] W. Liang, V. Ilchenko, A. Savchenkov, A. Matsko, D. Seidel, and L. Maleki, “Whispering-gallery-mode-resonator-based ultranarrow linewidth external-cavity semiconductor laser,” *Optics Letters*, vol. 35, no. 16, pp. 2822–2824, 2010.

[50] W. Lewoczko-Adamczyk, C. Pyrlik, J. Häger, S. Schwertfeger, A. Wicht, A. Peters, G. Erbert, and G. Tränkle, “Ultra-narrow linewidth dfb-laser with optical feedback from a monolithic confocal fabry-perot cavity,” *Optics Express*, vol. 23, no. 8, pp. 9705–9709, 2015.

[51] J.-F. Cliche, Y. Painchaud, C. Latrasse, M.-J. Picard, I. Alexandre, and M. Têtu, “Ultra-narrow bragg grating for active semiconductor laser linewidth reduction through electrical feedback,” in *Bragg Gratings, Photosensitivity, and Poling in Glass Waveguides*. Optical Society of America, 2007, p. BTuE2.

[52] G. Liu, Y. Zhu, Z. Liu, and M. Han, “Passive quadrature demodulation of an ultrasonic fiber-optic interferometric sensor using a laser and an acousto-optic modulator,” *Optics Letters*, vol. 44, no. 11, pp. 2756–2759, 2019.

[53] Q. Zhang, N. Liu, T. Fink, H. Li, W. Peng, and M. Han, "Fiber-optic pressure sensor based on *pi*-phase-shifted fiber bragg grating on side-hole fiber," *IEEE Photonics Technology Letters*, vol. 24, no. 17, pp. 1519–1522, 2012.

[54] A. Othonos, "Fiber bragg gratings," *Review of Scientific Instruments*, vol. 68, no. 12, pp. 4309–4341, 1997.

[55] Q. Wu and Y. Okabe, "High-sensitivity ultrasonic phase-shifted fiber bragg grating balanced sensing system," *Optics Express*, vol. 20, no. 27, pp. 28 353–28 362, 2012.

[56] Y. Zhu, L. Hu, Z. Liu, and M. Han, "Ultrasensitive ultrasound detection using an intracavity phase-shifted fiber bragg grating in a self-injection-locked diode laser," *Optics Letters*, vol. 44, no. 22, pp. 5525–5528, 2019.

[57] F. Wei, F. Yang, X. Zhang, D. Xu, M. Ding, L. Zhang, D. Chen, H. Cai, Z. Fang, and G. Xijia, "Subkilohertz linewidth reduction of a dfb diode laser using self-injection locking with a fiber bragg grating fabry-perot cavity," *Optics Express*, vol. 24, no. 15, pp. 17 406–17 415, 2016.

[58] Y. Zhu, Q. Zhang, G. Liu, X. Luo, and M. Han, "Fabry–perot sensor using cascaded chirped fiber bragg gratings with opposite chirp directions," *IEEE Photonics Technology Letters*, vol. 30, no. 16, pp. 1431–1434, 2018.

[59] T. Erdogan and V. Mizrahi, "Characterization of uv-induced birefringence in photosensitive ge-doped silica optical fibers," *JOSA B*, vol. 11, no. 10, pp. 2100–2105, 1994.

[60] P. Lu, D. Grobnic, and S. J. Mihailov, "Characterization of the birefringence in fiber bragg gratings fabricated with an ultrafast-infrared laser," *Journal of Lightwave Technology*, vol. 25, no. 3, pp. 779–786, 2007.

[61] S. Rashleigh, "Origins and control of polarization effects in single-mode fibers," *Journal of Lightwave Technology*, vol. 1, no. 2, pp. 312–331, 1983.

[62] M. Hanawa, T.-Y. Kim, T. Yamada, S.-J. Kim, C.-S. Park, and K. Nakamura, "Birefringence reduction on cascaded fiber bragg gratings," *Proceedings of the 2006 IEICE General Conference, C-3-107*, 2006.

[63] M. Hanawa, T. Yamada, T.-Y. Kim, C.-S. Park, and K. Nakamura, "Polarization dependency measurements on birefringence-reduced cascaded fbgs," *Proceedings of the 2006 IEICE Electronics Society, C-3-44*, 2006.

[64] L. L. Sánchez-Soto, J. J. Monzón, and G. Leuchs, "The many facets of the fabry–perot," *European Journal of Physics*, vol. 37, no. 6, p. 064001, 2016.

[65] J.-R. Lee and H. Tsuda, "Acousto-ultrasonic sensing using capsular fibre bragg gratings for temperature compensation," *Measurement Science and Technology*, vol. 17, no. 11, p. 2920, 2006.

[66] J. Wee, B. Wells, D. Hackney, P. Bradford, and K. Peters, "Increasing signal amplitude in fiber bragg grating detection of lamb waves using remote bonding," *Applied Optics*, vol. 55, no. 21, pp. 5564–5569, 2016.

[67] M. Islam, M. M. Ali, M.-H. Lai, K.-S. Lim, H. Ahmad *et al.*, "Chronology of fabry-perot interferometer fiber-optic sensors and their applications: a review," *Sensors*, vol. 14, no. 4, pp. 7451–7488, 2014.

[68] J. F. Dorighi, S. Krishnaswamy, and J. D. Achenbach, "Stabilization of an embedded fiber optic fabry-perot sensor for ultrasound detection," *IEEE Transactions on Ultrasonics, Ferroelectrics, and Frequency Control*, vol. 42, no. 5, pp. 820–824, 1995.

[69] A. Dandridge, A. B. Tveten, and T. G. Giallorenzi, "Homodyne demodulation scheme for fiber optic sensors using phase generated carrier," *IEEE Transactions on Microwave Theory and Techniques*, vol. 30, no. 10, pp. 1635–1641, 1982.

[70] K. A. Murphy, M. F. Gunther, A. M. Vengsarkar, and R. O. Claus, "Quadrature phase-shifted, extrinsic fabry–perot optical fiber sensors," *Optics Letters*, vol. 16, no. 4, pp. 273–275, 1991.

[71] I. Read, P. Foote, and S. Murray, "Optical fibre acoustic emission sensor for damage detection in carbon fibre composite structures," *Measurement Science and Technology*, vol. 13, no. 1, p. N5, 2001.

[72] B. Dong, M. Han, and A. Wang, "Two-wavelength quadrature multipoint detection of partial discharge in power transformers using fiber fabry-perot acoustic sensors," in *Fiber Optic Sensors and Applications IX*, vol. 8370. International Society for Optics and Photonics, 2012, p. 83700K.

[73] H. Liao, P. Lu, L. Liu, S. Wang, W. Ni, X. Fu, D. Liu, and J. Zhang, "Phase demodulation of short-cavity fabry–perot interferometric acoustic sensors with two wavelengths," *IEEE Photonics Journal*, vol. 9, no. 2, pp. 1–9, 2017.

[74] R. Pappu, "Acoustic emission detection using optical fibre sensors for aerospace applications," Ph.D. dissertation, Aston University, 2012.

[75] R. Ulrich, S. Rashleigh, and W. Eickhoff, "Bending-induced birefringence in single-mode fibers," *Optics Letters*, vol. 5, no. 6, pp. 273–275, 1980.

[76] R. Ulrich and A. Simon, "Polarization optics of twisted single-mode fibers," *Applied Optics*, vol. 18, no. 13, pp. 2241–2251, 1979.

[77] N. Stan, D. Bailey, S. Chadderdon, S. Webb, M. Zikry, K. Peters, R. Selfridge, and S. Schultz, "Increasing dynamic range of a fibre bragg grating edge-filtering interrogator with a proportional control loop," *Measurement Science and Technology*, vol. 25, no. 6, p. 065206, 2014.

[78] H. Wei, C. Tao, Y. Zhu, and S. Krishnaswamy, "Fiber bragg grating dynamic strain sensor using an adaptive reflective semiconductor optical amplifier source," *Applied Optics*, vol. 55, no. 10, pp. 2752–2759, 2016.

[79] H. Tsuda, E. Sato, T. Nakajima, H. Nakamura, T. Arakawa, H. Shiono, M. Minato, H. Kurabayashi, and A. Sato, "Acoustic emission measurement using a strain-insensitive fiber bragg grating sensor under varying load conditions," *Optics Letters*, vol. 34, no. 19, pp. 2942–2944, 2009.

[80] J. Wee, D. Hackney, P. Bradford, and K. Peters, "Experimental study on directionality of ultrasonic wave coupling using surface-bonded fiber bragg grating sensors," *Journal of Lightwave Technology*, vol. 36, no. 4, pp. 932–938, 2018.

[81] Q. Wu, Y. Okabe, K. Saito, and F. Yu, "Sensitivity distribution properties of a phase-shifted fiber bragg grating sensor to ultrasonic waves," *Sensors*, vol. 14, no. 1, pp. 1094–1105, 2014.

[82] E. D. Black, "An introduction to pound–drever–hall laser frequency stabilization," *American Journal of Physics*, vol. 69, no. 1, pp. 79–87, 2001.